WIMRC FORUM 2006

Proceedings of Lectures on

Cavitation in Turbo-machinery
&
In Medical Applications

International Manufacturing Centre
The University of Warwick
Coventry, CV4 7AL, UK

3rd July 2006

Editor
Professor S.C. Li

Assistant Editor
Miss N.A. Wensley

ISBN 0 902683 79 9

WARWICK IMRC Innovative Manufacturing Research Centre

THE UNIVERSITY OF WARWICK

PREFACE

Professor S.C. Li, Chair of WIMRC FORUM 2006
University of Warwick, Coventry, UK
S.Li@warwick.ac.uk

WIMRC FORUM 2006 was organized in response to the rapid development of cavitation research in hydraulic machinery and medical applications and to promote information exchange and international collaboration. Six invited lectures are presented in this document and I hope you will find them interesting and informative.

I would like to thank the speakers and members of the organizing committee for their valuable contributions to the Forum. Thanks are due to Dr Nick Mallinson, Research Manager of WIMRC, for his overall management and to the Forum Secretary, Miss Valerie Saker and my Editing Assistant, Miss Nikki-Ann Wensley, for their professional work.

The financial support from EPSRC via WIMRC (projects RESCM9001 and SCAP16) and overall support from the WIMRC Management Committee is greatly appreciated.

CONTENTS

1. WIMRC INTRODUCTION

Dr Nick Mallinson
WIMRC, University of Warwick, Coventry, UK
nick.mallinson@warwick.ac.uk

1.1 HISTORY

WIMRC was established at the University of Warwick in October 2001 drawing on research capabilities within Warwick Manufacturing Group (WMG), the wider School of Engineering (SoE) and the Warwick Business School (WBS) and supported by funding from the Engineering and Physical Sciences Research Council (EPSRC). Its remit was to integrate engineering and management research to deliver high quality outputs addressing the competitiveness of UK manufacturing industry in the specific focus sectors of premium automotive, aerospace, construction and medical. WIMRC has recently been awarded EPSRC Phase 2 funding to support it until September 2011.

The benefits of WIMRC to the University include:

- Multidisciplinary research encouraging cross-departmental working (including

collaboration with Warwick Medical School which was formed during Phase 1)
- Encouraging more adventurous research
- Regular self-analysis and critical review of activities
- Transparent management processes nurturing a more cooperative innovative climate

1.2 WIMRC MANAGEMENT

Dr Ken Young is WIMRC Director and Dr Nick Mallinson is WIMRC Research Manager.

Dr Ken Young is a Reader in WMG with special interest in Automation and Robotics. He has been a member of staff at Warwick for 15 years during which time he has won research grants worth over £7M and published 25 journal papers. He is a member of the EPSRC College and Chairman of the British Automation & Robot Association.

Dr Nick Mallinson was appointed WIMRC Research Manager in May 2005, having previously been Sales & Marketing Director for Dynex Semiconductor Limited. He gained his PhD at Imperial College and then worked in semiconductor product development and marketing for 20 years, during which time he became a Chartered Engineer and gained an MBA from the Open University. During 2005, the WIMRC Management Committee, made up of academics from WMG, the wider SoE and WBS, was formed to replace the original membership structure. A representative from WMS joined the committee in February 2006. The Management Committee meets as required to support the Director and Research Manager in the definition of strategy, selection of new projects, preparation of the Annual report and the like.

The WIMRC Steering Group, chaired by Dr Alistair Keddie and made up of external industrialists and academics, meets on a six monthly basis to monitor the activities of the centre on behalf of EPSRC and provide strategic guidance and critical comment to the management team.

1.3 WIMRC'S RESEARCH PRIORITIES

WIMRC's research priorities for Phase 2 have been determined by reference to the themes followed during Phase 1, an analysis of research conducted during Phase 1, a review of our core competencies and a requirement to identify the following:

- Significant challenges within a medium to long term time frame
- Problems or obstacles where solutions will make a "real difference"
- Areas where manufacturing knowledge transfer is relevant
- Challenges and themes that complement other IMRCs' activities

During Phase 1, WIMRC projects fell into one of three distinct manufacturing "themes":

- Technology – Novel Application of Materials, Processes and Tool Design / Manufacture
- Design – Tools & Techniques
- Management - Business Processes and Systems, People and Organisational Culture

This model will also be followed during Phase 2 but priority will be given to projects that aim to be multidisciplinary, combining design, technology and management research to produce relevant and sustainable solutions to real-world problems.

1.4 VISION STATEMENT (2006 – 2011)

"To be a centre of research excellence, demonstrating an ability to innovate, influence and perform in manufacturing research Internationally at the highest academic level by applying competencies in cross-disciplinary research in manufacturing technology and operations, materials, business processes and related management activities to enhance the competitiveness and effectiveness of organisations within the specific sectors of intelligent and eco-friendly vehicles (IEV) and lean healthcare (LH)"

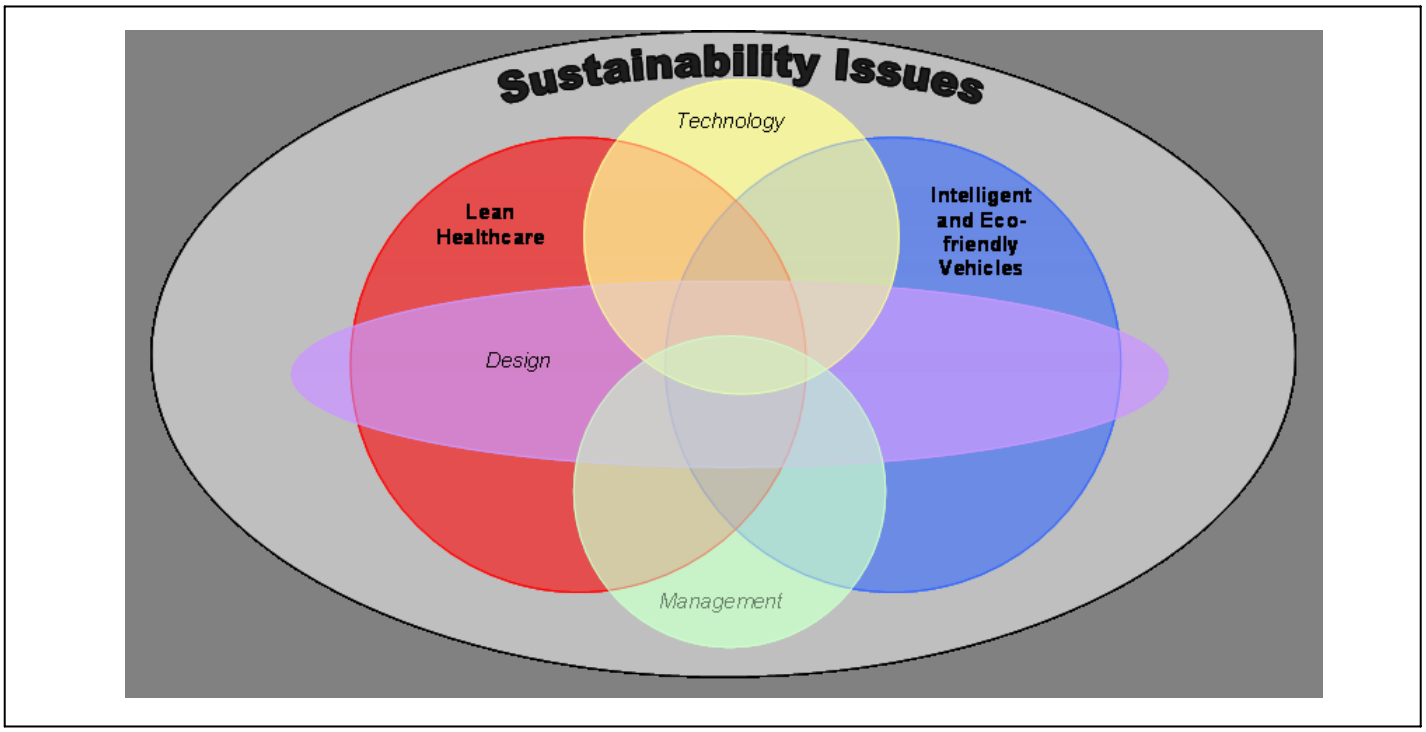

1.5 THE EVOLUTION OF WIMRC – PHASE 2 OBJECTIVES

Through appropriate calls for research proposals, communication of strategy and progress, performance monitoring and transparent decision making, the WIMRC Management Committee has set itself several goals including:

- ***Adventure*** - Encouraging high-risk research;
- ***Fostering Team Building*** - Building and maintaining strong partnerships with vehicle and healthcare partners to ensure research addresses key sector challenges and is exploited;
- ***Cross Sectoral*** - Performing leading edge medium to long term research at the interface of design, technology and management to generate internationally competitive knowledge and a fund of novel processes and techniques;
- ***Sustainability*** - Ensuring that projects incorporate work to investigate and improve the economic, environmental, infrastructure, social or political sustainability of solutions in the focus sectors;
- ***Innovative Vehicles*** - Supporting research specifically relevant to the "next but one" generation of vehicles (automotive and aerospace);
- ***Healthcare*** - Establishing WIMRC as a leading centre of excellence for lean healthcare and a centre of innovation for the NHS;
- ***Nurturing*** – Exploring adventurous new opportunities in manufacturing through short term feasibility studies;
- ***Researcher Development*** - Developing the next generation of researchers for UK industry through an increased emphasis on recruiting top quality research students and academics;
- ***Creatively Exchange Technology*** – Building links and, where appropriate, performing mutually beneficial projects with other IMRCs and research centres;
- ***Developing Research Clusters*** – sponsoring multi-disciplinary projects within Warwick University.

1.6 WIMRC'S CORE COMPETENCIES AND RESEARCH THEMES

1.6.1 COMPETENCIES

Physical Engineering/Science
Plastic and composite materials
Automation
High reliability (robust) electronics
Joining processes
Experimental engineering
Optical and thermal instrumentation

Soft Engineering/Science
Knowledge and innovation management
Lean manufacturing & services
Change management
Producing introduction processes
Quality management
Supply chain management

1.6.2 DESIGN THEME

Manufacturing and design are inextricably linked. Work in this area falls into the following:

- Innovative design methods and knowledge based engineering
- Design analysis
- Design and new product introduction processes
- Experiential engineering

1.6.3 MANAGEMENT THEME

Management of manufacturing including services is critical to the success of modern organisations. Work in this area falls into the following:

- Knowledge management
- Innovation management
- Lean manufacturing
- Management of complexity
- Supply chain management
- New product introduction

1.6.4 TECHNOLOGY THEME

WIMRC has always had a strong technology focus. Research areas in this area include:

- Materials processing technology
- Control systems
- Analysis of sound
- Direct manufacture and tooling
- Joining processes

1.7 CO-OPERATIVE COMPLEMENTARY RESEARCH

WIMRC is committed to working both with other IMRC's and Universities without IMRC's. WIMRC is determined to apply its knowledge base, core competencies and research staff where it can maximise added value in terms of knowledge generation and impact on industrial processes. WIMRC recognises that its capabilities will have greatest impact for UK industry if they are combined with complementary outputs from other IMRC's to create more comprehensive solutions.

Discussions have already been held with Cardiff, Loughborough, Nottingham, Salford and UCL IMRC's.

1.8 RESEARCH PROJECTS' SELECTION CRITERIA

Proposals are considered against a number of criteria intended to ensure that high quality research will be performed over the medium to long term. Criteria include 'qualifiers' (conditions that all submissions must meet in order to go forward to a detailed 'peer' review), and 'differentiators' (distinguishing features that enable choices to be made between competitive high quality proposals). Projects selected for funding continue to be reviewed against the selection criteria as they progress.

1.9 WIMRC'S PHASE 2 RESEARCH PROJECTS

WIMRC has recently approved funding for 15 scoping projects and 5 feasibility studies to investigate and identify suitable multidisciplinary research challenges to be addressed by Phase 2 projects. These projects will run up to September 2006 and from their outputs it is intended to define a small number of IEV and LH projects which will run over the five years of Phase 2 funding.

Regular showcase events will be arranged to disseminate the work as widely as possible.

For more information please view the WIMRC website at http://go.warwick.ac.uk/wimrc.

Invited Lecture

2. A REVIEW OF CAVITATION USES & PROBLEMS IN MEDICINE

Professor Christopher E. Brennen
California Institute of Technology, Pasadena, California, USA
brennen@caltech.edu

ABSTRACT

There are an increasing number of biological and bioengineering contexts in which cavitation is either utilized to create some desired effect or occurs as a by-product of some other process. In this review an attempt will be made to describe a cross-section of these cavitation phenomena. In the by-product category we describe some of the cavitation generated by head injuries and in artificial heart valves. In the utilization category we review the cavitation produced during lithotripsy and phaco-emulsification. As an additional example we describe the nucleation suppression phenomena encountered in supersaturated oxygen solution injection.

Virtually all of these cavitation and nucleation phenomena are critically dependent on the existence of nucleation sites. In most conventional engineering contexts, the prediction and control of nucleation sites is very uncertain even when dealing with a simple liquid like water. In complex biological fluids, there is a much greater dearth of information.

Moreover, all these biological contexts seem to involve transient, unsteady cavitation. Consequently they involve the difficult issue of the statistical coincidence of nucleation sites and transient low pressures. The unsteady, transient nature of the phenomena means that one must be aware of the role of system dynamics in vivo and in vitro. For example, the artificial heart valve problem clearly demonstrates the importance of structural flexibility in determining cavitation occurrence and cavitation damage. Other system issues are very important in the design of in vitro systems for the study of cavitation consequences.

Another common feature of these phenomena is that often the cavitation occurs in the form of a cloud of bubbles and thus involves bubble interactions and bubble cloud phenomena.

In this review we summarize these issues and some of the other characteristics of biological cavitation phenomena.

NOMENCLATURE

A : Typical dimension of the cloud of bubbles.
R : Typical equilibrium radius of the bubbles.
α : Equilibrium void fraction in the cloud.
β : Interaction parameter, $\alpha A^2/R^2$

2.1 INTRODUCTION

One of the first people to recognize the occurrence of cavitation in living organisms was E.N. Harvey whose work eventually encompassed many aspects of bubble formation in plants and in animals. His considerations of the state of tension in the sap of trees led him to important deliberations on the ability of a liquid to sustain tension and, consequently, on a model ("the Harvey nucleus") that he used to explain the existence of stable cavitation nuclei in a liquid [2.1-2.5]. This model was an important precursor to our current understanding of the existence of stabilized nuclei in the cracks and interstices of solid surfaces in contact with a liquid. Harvey went on to an erudite and broad ranging research career, that included investigations of the existence of cavitation nuclei in blood and in animal tissue [2.1,2.2], studies of the "bends" or bubble formation during

decompression [2.6], and investigations of cavitation during wounding by high velocity missiles [2.7] as well as a host of studies of bioluminescence. He has been called the "Dean of Bioluminescence" but could also be identified as the father of cavitation studies in the biological environment.

Today, we recognize that the processes that involve cavitation in a biological or bioengineering context are so wide-ranging that it would be impossible (and excessively tedious) to attempt a comprehensive review. Rather we will focus on the different types of cavitation that occur or are generated, attempt to find common themes and thereby suggest avenues of basic research that might help advance these applications.

The cavitation that occurs in biological, bioengineering and biomedical contexts can be divided into that which is deliberately induced in order to generate some beneficial effect and that which occurs as an undesirable by-product of some other procedure or device. We begin by reviewing the former.

2.2 ULTRASOUND

By far the commonest deliberate generation of cavitation in medicine is through the use of ultrasound. For a comprehensive recent review of the therapeutic effects of ultrasound the reader is referred to the excellent review by Bailey et al. [2.8]. Though the normal use of ultrasound is to emulsify unwanted tissue or to pulverize unwanted solid material, it is also beginning to be used for hemostasis (to stop bleeding in internal organs [2.9] such as the liver [2.10] and spleen [2.11]), for tumour necrosis [2.8] and for immunotherapy [2.8].

Two different tissue destruction techniques are used and are described in the following paragraphs. In some applications an ultrasonically vibrating probe is placed in close proximity to the tissue or solid material. The cavitation induced at the tip of this probe creates the desired effect when it is placed close to the tissue or solid material. One of the earliest uses of such an ultrasonic probe was in dentistry, where ultrasonic probes are now commonly used to clean teeth by dislodging plaque [2.12] with product names such as Cavijet and Cavitron [2.13].

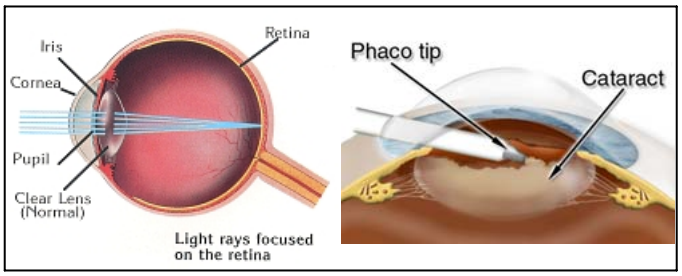

Figure 2.1: Schematics of the eye and of the phaco-emulsification procedure.

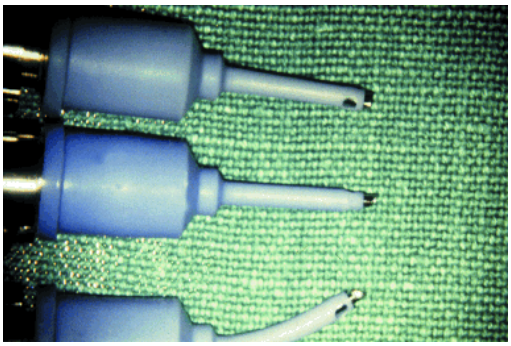

Figure 2.2: Phaco-emulsification probes (from Sabbagh [2.15]).

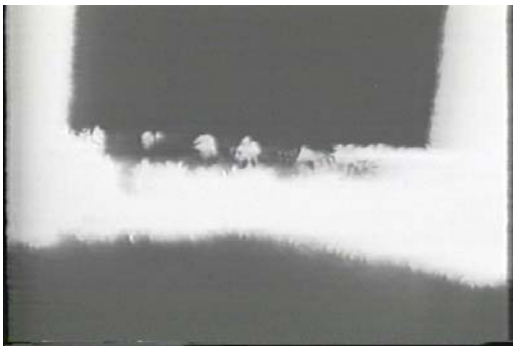

Figure 2.3: Outline of cavitation bubble cloud (the black images below the black rectangle) on the face of a phacoemulsifier (Anis [2.18]).

Another common application is in phaco-emulsification, the procedure most commonly used to emulsify and remove the natural optical lens during cataract surgery. A perfusion and vacuum system is built into the probe in order to remove the emulsified tissue. The invention of the phaco-emulsification probe by Charles Kelman in 1967 was, in fact, motivated by the dental plaque-removing tool [2.14]. The advantage of the phaco-emulsification tool is that it can be inserted through a very small incision in the

side of the eye and the old lens removed with minimal invasion (see Figures 2.1 and 2.2). The new artificial lens is then inserted in folded form through the same incision and unfolded in place. More than a million such procedures take place each year. However, the WHO estimates that 17 million more people in the world presently suffer from cataracts. While problems with the procedure are rare, the main concerns are collateral damage to surrounding tissue and the possibility of damage to the material of the tool itself, which might result in metal debris being left behind in the eye [2.16].

Figure 2.3 is a frame from a high-speed video of a phaco-emulsification probe in use. It shows the cavitation on the 0.9mm diameter end face of the probe (or needle) as it approaches a cadaver lens (Anis [2.17]). Variations in the design of the probe have been deployed in attempts to increase its effectiveness and to minimize collateral damage by confining the cavitation to a well-controlled volume on the face of the device.

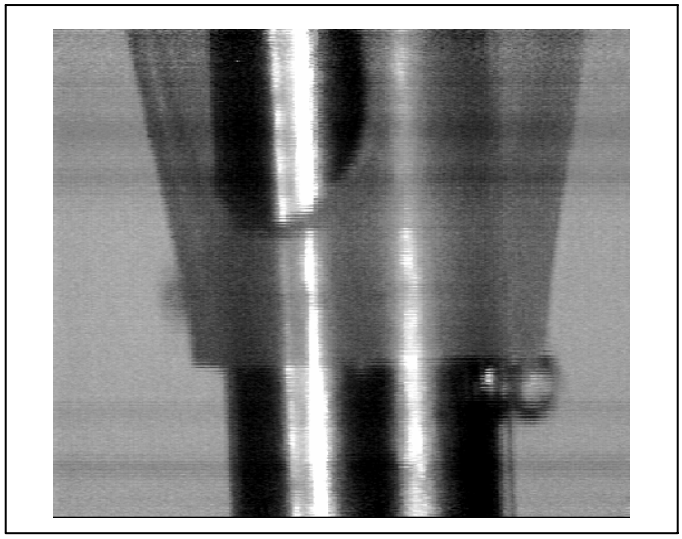

Figure 2.4: Cavitation bubbles near irrigation sleeve of a phaco-emulsifier (from [2.20]).

One particular variation is particularly interesting from a fluid mechanical perspective. Anis [2.17,2.18] has developed a probe, which not only vibrates at ultrasonic frequency (40kHz in this case) but also rotates (Figure 2.3 is a view of this probe in action). Control over the extent of cavitation is important in minimizing collateral damage. In the absence of such control, cavitation can occur in unexpected locations; for example, Figure 2.4 shows cavitation bubbles formed at the irrigation sleeve around the outside of the tool.

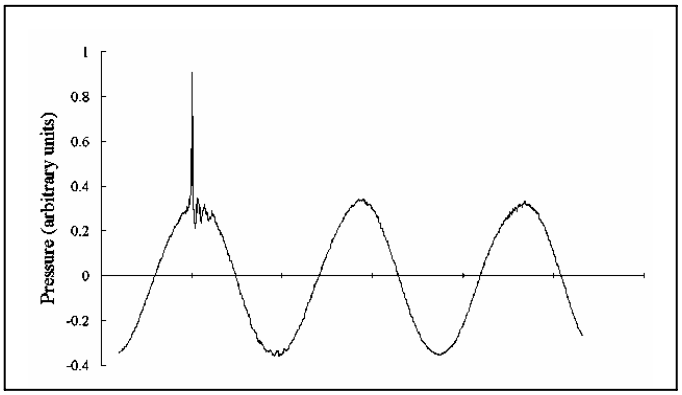

Figure 2.5: Typical phaco-emulsification pressure signal showing a cavitation event during the first high pressure cycle (from [2.19]).

The typical noise generated by a cavitation event on the face of a phaco-emulsifier is shown in Figure 2.5 [2.19]. The pulses shown superimposed on the first high pressure cycle of the ultrasound are very similar to the cavitation event noise measured in other hydrodynamic experiments; for example, Figure 2.6 shows the prototypical signal produced by the collapse of a single cavitation bubble [2.24,2.25] and includes the large positive spike produced by the first collapse as well as a second spike produced by the second collapse following the first rebound.

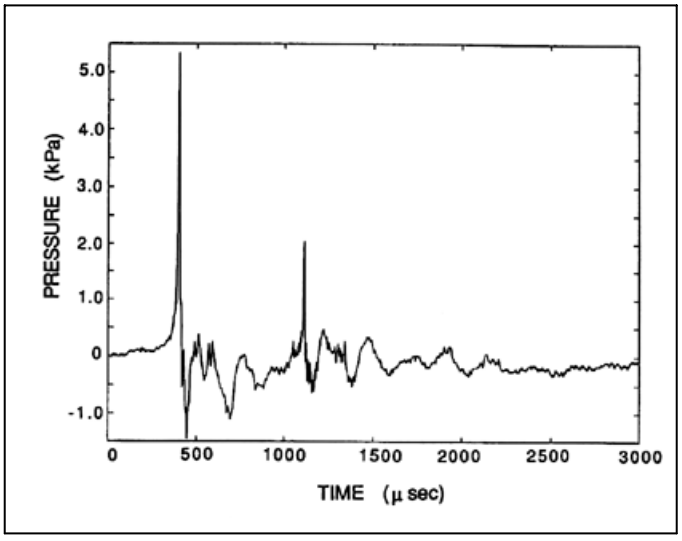

Figure 2.6: Typical acoustic signal produced by the collapse of a single cavitation bubble [2.24, 2.25].

2.3 FOCUSSED SHOCKWAVES AND ULTRASOUND

Cavitation is also generated remotely by focusing shockwaves or ultrasound at a target site within the body. For example, focusing is now commonly used in lithotripsy [2.22, 2.8, 2.25, 2.26], the process that remotely disintegrates kidney and gall stones so that they can be rejected by normal routes. With the patient submerged in a water bath (so that the surroundings closely match the acoustic impedance of the body), shockwaves or strong ultrasonic waves are focused at the site of the stone. Multiple shocks or wavetrains are then used to break the stone into pieces small enough to be ejected by the body. Cavitation may or may not play a role in the disintegration of the stone; it can also cause substantial collateral tissue damage. For an excellent recent review of lithotripsy research the reader is referred to Bailey et al. [2.27].

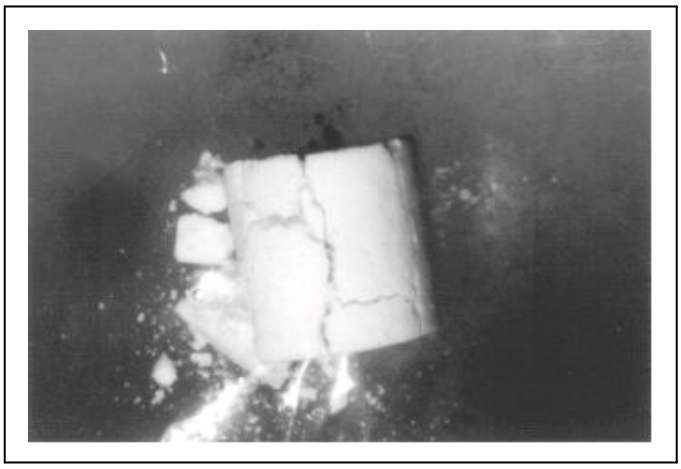

Figure 2.7: Artificial stone fractured by shockwave lithotripsy [2.23].

Figure 2.8: New and damaged artificial renal stone (courtesy of Erin Hatt, Dept. of Anatomy and Cell Biology, Indiana University).

Lithotripsy using shock waves has a long history [2.26, 2.27]. Figure 2.7 exemplifies the fracture of an artificial stone by lithotripsy using strong shock waves. It seems likely that this form of communition results from shock-induced stresses rather than cavitation. On the other hand, the damage shown in Figure 2.8 seems to be quite characteristic of cavitation. Strong shocks do cause widespread cavitation. Frequency dispersion prevents the shock waves from being more narrowly focused and consequently the focal volume is often significantly larger than the target stone. Figure 2.9 shows the formation of cavitation bubbles on an artificial stone in a shock wave lithotripter. Another illustration, Figure 2.10, exemplifies how widespread the cavitation can be in a focal volume significantly larger than the target stone (the larger black object on the right). Consequently the cavitation generated by the shockwaves causes substantial collateral tissue damage in conventional lithotripsy. Double pulse shock wave lithotripsy can help reduce this focal volume [2.29].

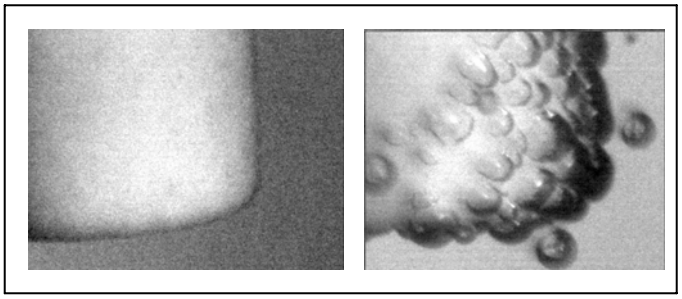

Figure 2.9: Cavitation bubbles (right) near surface of an artificial stone (left) (courtesy of D. Sokolov, M.R. Bailey, Centre for Industrial and Medical Ultrasound, U. Washington)

The use of focused ultrasound (rather than shock waves) is more recent and has some significant advantages (see the review by Bailey et al [2.8]). With a significantly narrower spectrum ultrasound can be focused much more precisely and therefore has the potential for significantly reduced collateral damage.

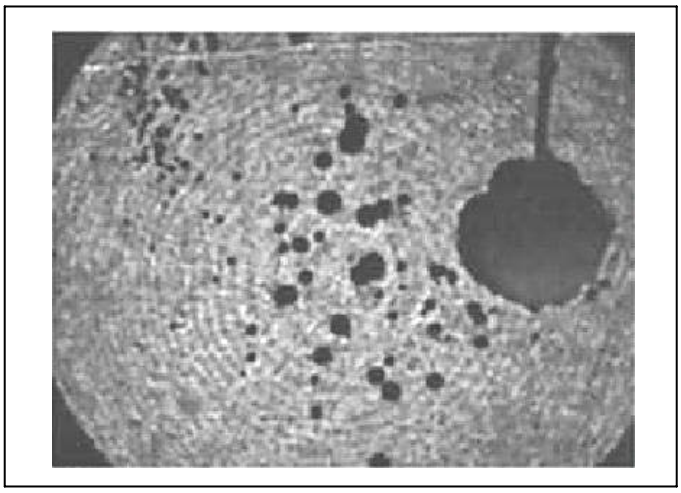

Figure 2.10: Typical shockwave lithotripsy bubble cloud near stone (larger black object) (from Zhu et al. [2.24]).

2.3.1 FOCUSSED ULTRASOUND

The use in lithotripsy of focused ultrasound (rather than shock waves) is more recent [2.8, 2.25] and has some significant advantages. With a significantly narrower spectrum ultrasound can be focused much more precisely and therefore has the potential for significantly reduced collateral damage. It is possible to focus the cavitation on the surface of the stone (Figure 2.11), enhancing the damage potential while reducing the collateral damage. The cavitation generated at the focal point pulverizes the material of the stone, ultimately reducing it to a powder [2.28].

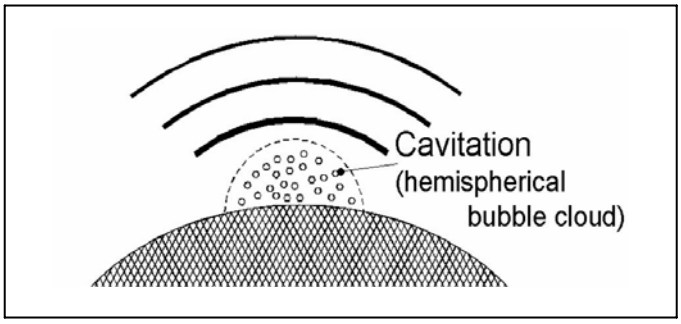

Figure 2.11: Schematic of the cavitation formed on a target at the focal point of an ultrasonic lithotripter (from [2.28]).

Figure 2.12 (from [2.28]) shows a typical cloud of cavitation bubbles formed at the focal point. During the lecture several videos of the damage process will be presented.

Various techniques have been investigated in order to try to refine lithotripter design. These usually have the competing objectives of limiting the collateral damage by confining the cavitation to a well-defined region while at the same time generating the most damage potential. These are partially competing objectives and the strength of the shockwaves or the ultrasound is usually limited by the need to minimize collateral damage. However, knowledge of the intricacies of bubble dynamics suggests some superior strategies. Thus, for example, in shockwave lithotripsy multiple pulses [2.28] may be better than single pulses.

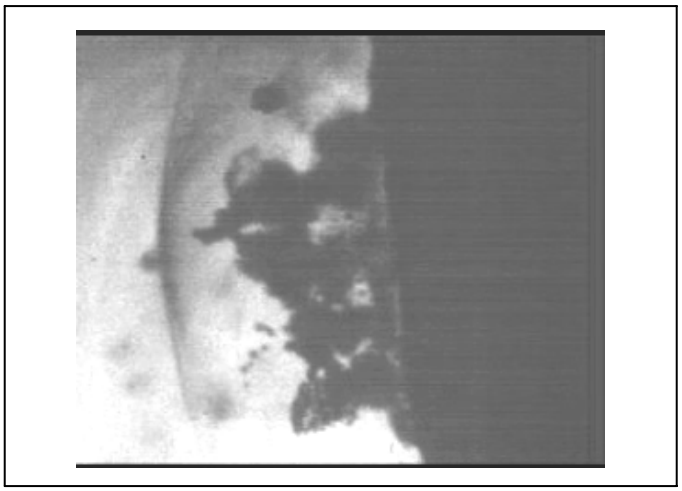

Figure 2.12: Bubble cloud (centre) on face of a target stone (right) (from Matsumoto et al. [2.28]).

As another example, we would note the strategy devised by Matsumoto et al. [2.28] who found that a period of high frequency ultrasound followed by a few low frequency cycles can be very effective. The high frequency period generates a cloud of small bubbles in the focal region by the process of rectified diffusion [2.21]. The subsequent low frequency pulses then cause the collapse of this cloud in the manner described by Wang and Brennen (see [2.30, 2.31]).

2.4 CLOUD CAVITATION

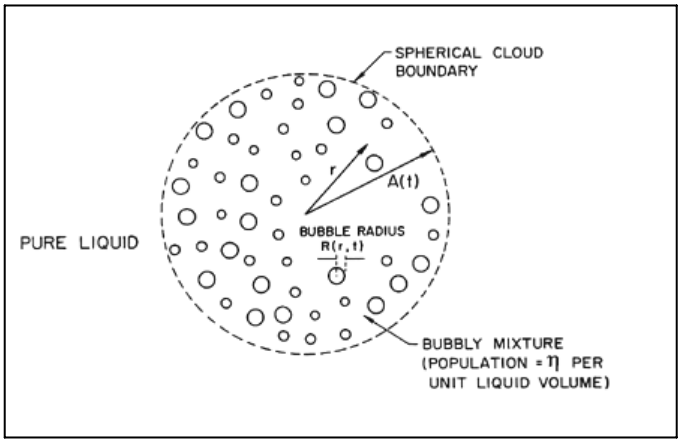

Figure 2.13: Schematic of a spherical cloud of cavitation bubbles [2.30, 2.31].

At this point it is worth digressing to note that many of the applications described herein involve the dynamics of clouds of cavitation bubbles and that there is a continuing need to proceed beyond single cavitation bubbles to understand the dynamics of such clouds. The interactions between the bubbles in these clouds generate new phenomena that may be the key to understanding the effectiveness of the cavitation tool. For example, Wang and Brennen [2.30, 2.31] examined the geometrically simple case of the growth and collapse of a spherical cloud of bubbles (such as depicted in Figure 2.13) surrounded by pure liquid. It transpires that the response of this cloud to an episode of reduced pressure in the surrounding liquid is quite different depending on the magnitude of the parameter $\alpha A^2/R^2$ where α is the initial volume fraction of bubbles in the cloud and A and R are the typical linear dimensions of the cloud and the individual bubbles. When α is much greater than unity the typical cloud response to an episode of reduced pressure is shown in Figure 2.14. Note that the bubbles on the surface of the cloud grow more rapidly than those in the interior, which are effectively shielded from the reduced pressure in the surrounding liquid. More importantly the bubbles on the surface collapse first and a collapse front propagates inward from the cloud surface developing into a substantial shock wave.

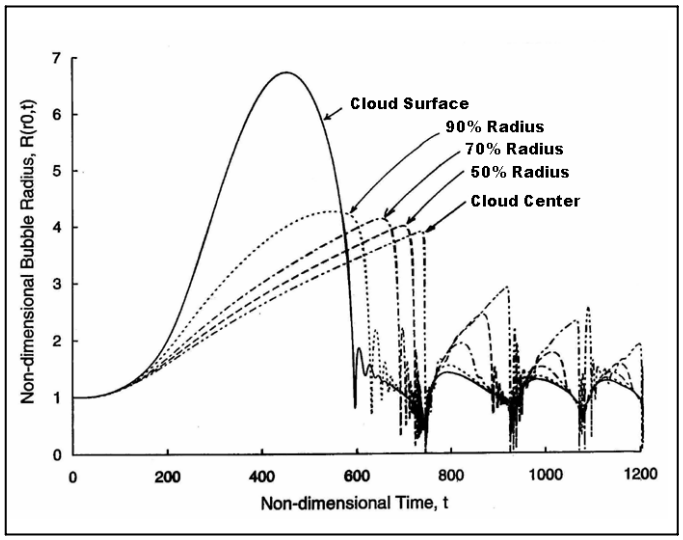

Figure 2.14: A typical time history of the bubble size at six different Lagrangian positions in a spherical cloud in response to a period of reduced pressure in the surrounding liquid (between t=0 and t=250) when the parameter α is much greater than unity [2.30, 2.31].

Figure 2.15 is a snapshot in time of the form of the collapse front and the large pressure pulse or shock wave that is associated with it. Due to geometric focusing this shock wave strengthens as the shock proceeds inwards and creates a very large pressure pulse when it reached the centre of the cloud.

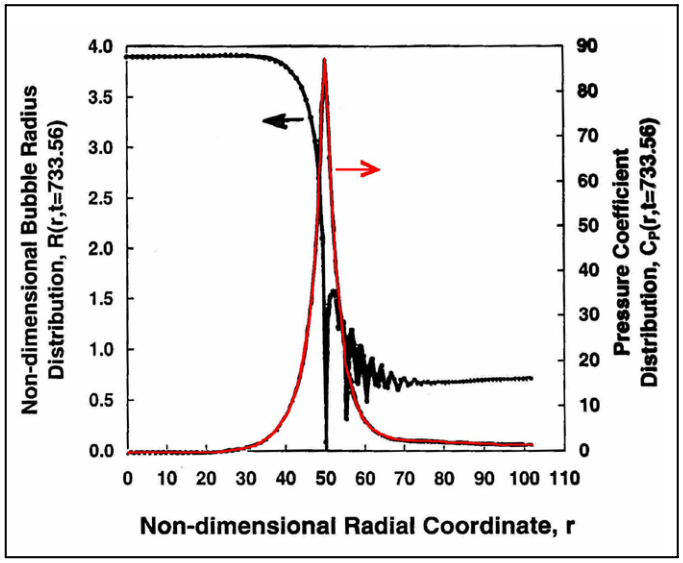

Figure 2.15: A snapshot in time of the radial distribution of bubble size (black) and pressure (red) from the same calculation as Figure 2.14 at a moment when the collapse shock is roughly half way into the cloud [2.30, 2.31].

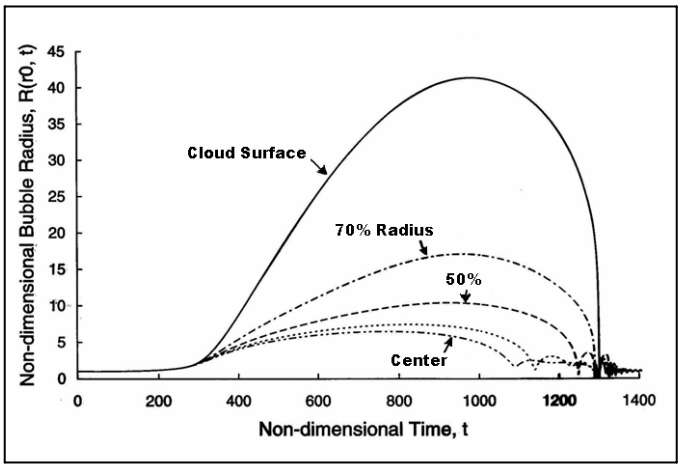

Figure 2.16: A typical time history similar to that of Figure 2.14 except that the parameter is of order unity or less [2.30, 2.31].

On the other hand when the initial void fraction is small or A/R is small such that α is less than unity, the response of the cloud as shown in Figure 2.16 is quite different. Then the shielding causes the bubbles at the centre of the cloud to collapse first, resulting in an outgoing collapse front that weakens geometrically resulting in a quite different dynamic.

While real bubble clouds are often far from spherical the potential for similar shielding effects still clearly exists and there are a number of experimental observations that suggest that geometric collapse front focusing causes the enhanced noise and damage potential associated with cavitation clouds.

It should also be noted that this simple spherical cloud example demonstrates a clear need for enhanced computational tools that would be capable of predicting these effects in more complex geometries and systems so that the kinds of complex strategies like that explored by Matsumoto could be examined analytically. Hence there is a need for CFD methodologies capable of predicting these complex bubbly flows. Tanguay and Colonius [2.32] have addressed this need and their work is exemplified by Figure 2.17 which shows a comparison between the photographs of the bubbly clouds caused in the focal region by a double shockwave lithotripter pulse (photographs by Sokolov, see [2.29]) and the calculations of the void fraction distribution from the computations of Tanguay and Colonius.

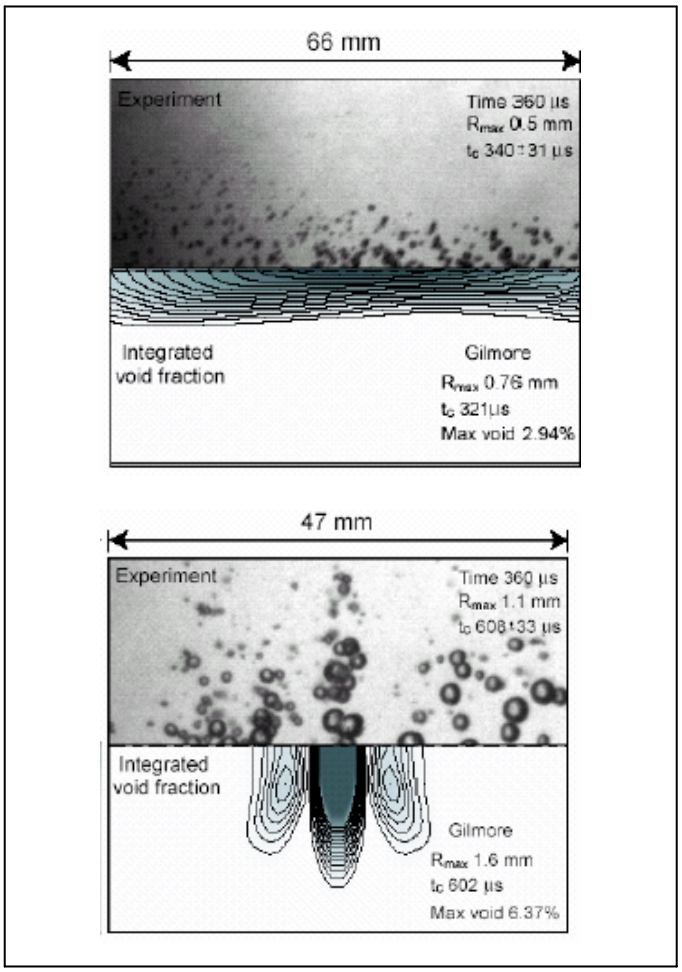

Figure 2.17: Comparisons between the experimental bubble clouds (upper half of figures, photographs by Sokolov (see [2.29]) and void fraction distributions from the calculations of Tanguay and Colonius [2.32]. Single pulse on left, double pulse on the right.

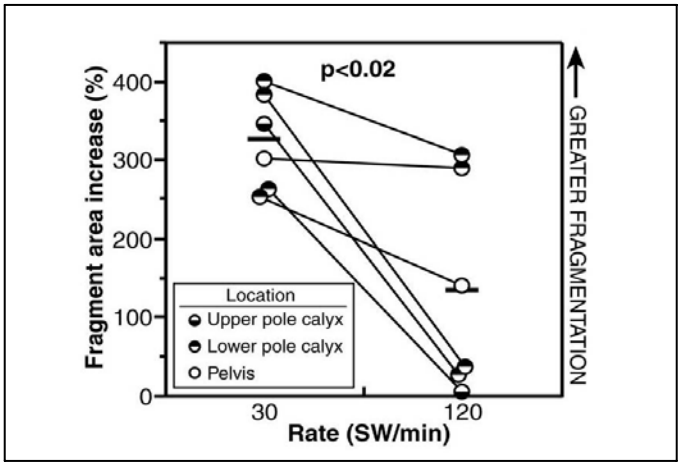

Figure 2.18: Measured fragmentation as a function of the rate or number of shock waves per minute from Paterson et al. [2.33].

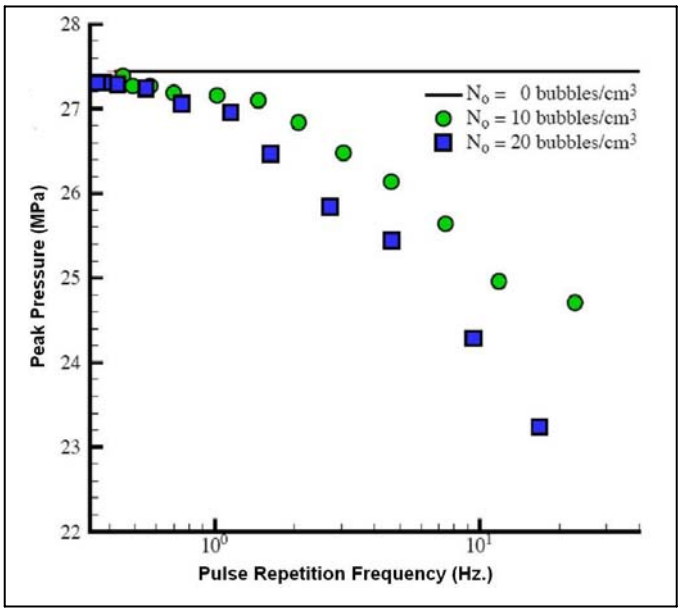

Figure 2.19: Calculated peak pressure as a function of the pulse repetition rate from Tanguay and Colonius [2.32].

These computational tools are also approaching the point where they can be used to generate useful information on parametric trends. Figures 2.18 and 2.19 provide one example. Figure 2.18 presents measured data, which shows the initially surprising result that the fragmentation due to shockwave lithotripsy decreases as the number of shockwaves per minute is increased. However, calculations by Tanguay and Colonius [2.32] show that the same trend emerges from the calculations as a result of rectified diffusion effects [2.21].

2.5 LASER-INDUCED CAVITATION

Another method of generating cavitation in a selected region is by means of a focused laser beam. Known as photo disruption, the focused laser light creates cavitation bubbles that cut through tissue and thus generate precise microscopic incisions that are of great potential value in many surgical procedures. Known as "light scalpels", Nd:YAG laser pulses have, for example, become a well-established tool in "non-invasive" intraocular surgery [2.34-2.36].

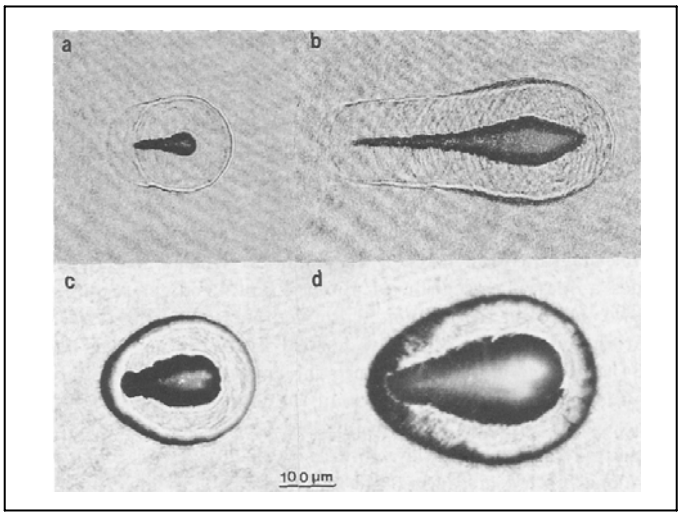

Figure 2.20: Shockwaves and bubbles formed at the focal point by picosecond laser pulses (a and b) and by nanosecond pulses (c and d). Beam coming from right. From Vogel and Busch [2.38].

The key to these tools is to produce repetitive, low energy pulses that have a very small damage range and thus limit undesirable collateral damage. As Vogel and his co-workers have demonstrated (see, for example, [2.37, 2.38]), the extent of the damage is proportional to the cube root of the pulse energy, and therefore the objective is to use the lowest energy laser pulse that still causes cavitation. Vogel and Busch [2.38] have shown that this can be achieved by reducing the duration of the laser pulses and that picosecond pulses are therefore superior to nanosecond pulses. Some of their photographs are reproduced in Figure 2.20; each frame shows the extent of both the shock wave associated with the initiation of cavitation and, inside that, the cavitation bubble itself. The laser pulse is arriving from the right and the shape is of the images is, in part, determined by the shape of the focal volume.

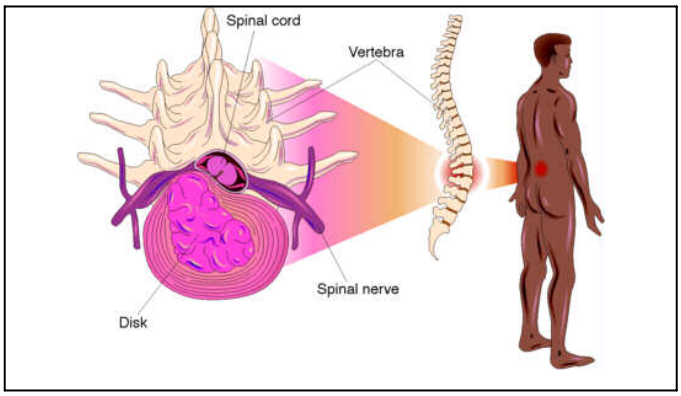

Figure 2.21: Schematic of the spinal structure (illustration by Electronic Illustrators Group).

Focused laser light is also used in other surgical procedures, for example, laser-induced lithotripsy [2.39] and in neurosurgery. In the latter, the primary issue is a concern for the limited control of the real-time laser interactions with the neural tissue (see, for example, [2.40]). Another example of the laser-induced cavitation is the procedure known as percutaneous laser disc decompression [2.41]. Laser energy is introduced into the nucleus pulposus (the gelatinous core of a spinal disk - see Figure 2.21) through a needle in order to vaporize a small volume of the nucleus and, by removing that volume, reducing the pressure of the disk and thus relieve the pressure on the neural tissue.

2.6 ARTIFICIAL HEART VALVE CAVITATION

One subject area that has received considerable publicity and therefore some careful attention (see [2.42-2.49]) is the issue of artificial heart valve cavitation, a problem whose seriousness did not become apparent until a large number of these valves had been installed. Though cavitation damage to the valve itself is an issue, the rupture of red bloods cells (hemolysis) by the cavitation is the primary concern. Parenthetically we note that attached cavitation appears to be more hemolytic than bubble cavitation [2.50].

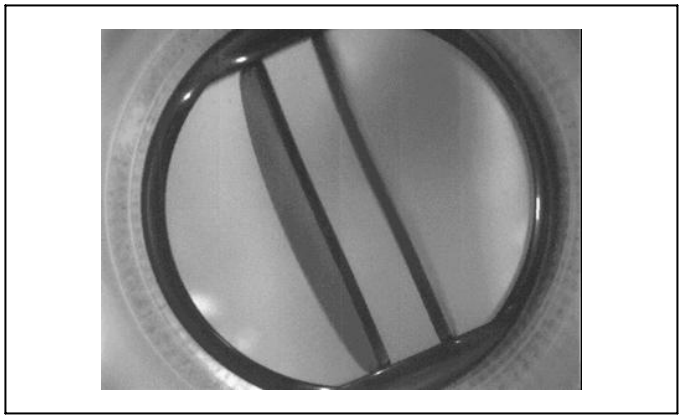

Figure 2.22: Bi-leaflet artificial heart valve in the open position viewed from downstream (from Rambod et al. [2.48]).

Though there are a number of different designs of prosthetic heart valves we choose to illustrate the phenomenon using the bi-leaflet type shown in Figure 2.22. The flows associated with this valve prior to and during closure are sketched in Figure 2.23.

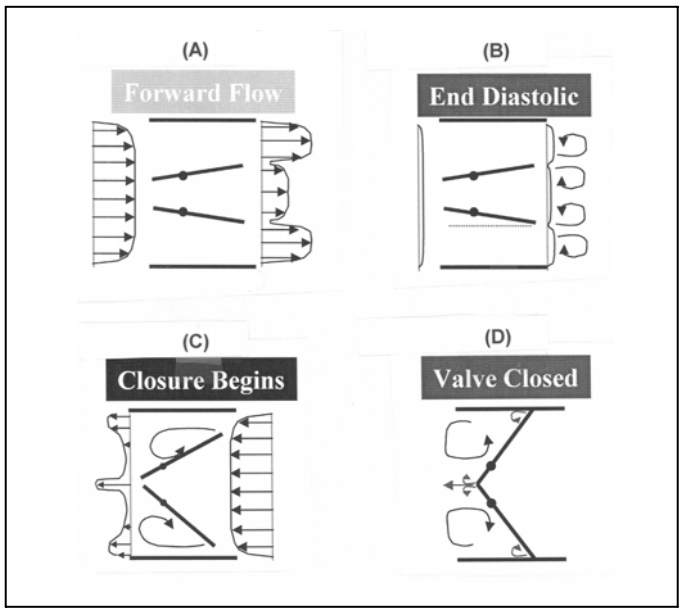

Figure 2.23. Schematic of the flows associated with the closing of a bileaflet prosthetic heart valve (from [2.49]).

The two leaflets hinge at roughly the end-on locations shown in Figure 2.23. When first subjected to backflow (stage B, Figure 2.23) these leaflets move in such a way that, just prior to closure (stage C, Figure 2.23), there are narrow passages both along the central diameter and at the circular tips of the leaflets. For a time interval just before and after closure the deceleration of the flow downstream of the valve

generates low pressures within the jets and vortices emanating from these temporary narrow passages, thus causing cavitation [2.49].

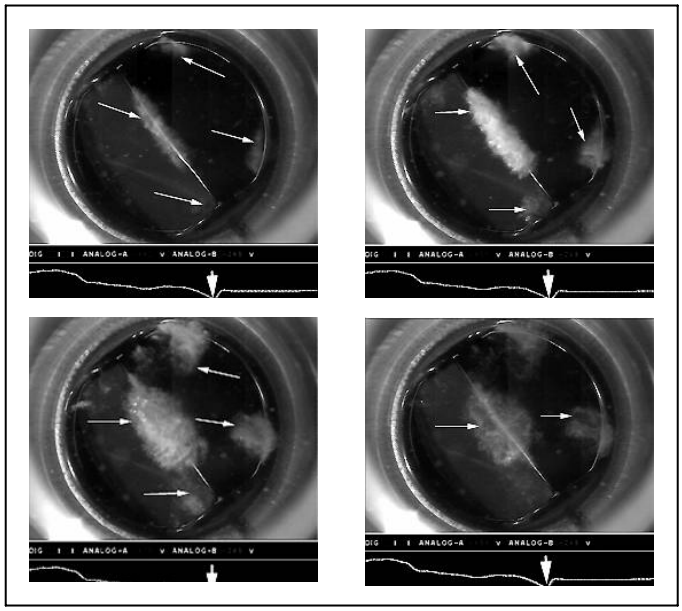

Figure 2.24: Photographs of cavitation downstream of a closing and closed artificial heart valve (from Rambod et al. [2.48]).

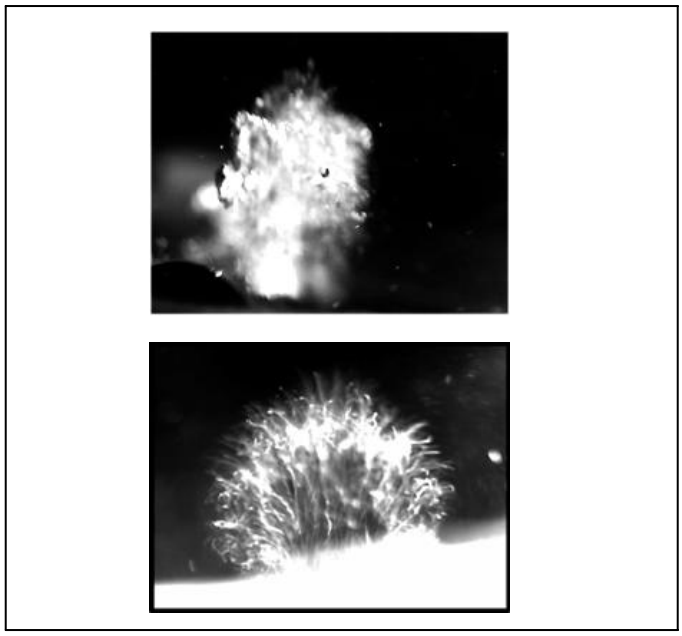

Figure 2.25: Close-up views of cloud-like cavitation in an artificial heart valve (from Rambod et al. [2.48]).

The extensive and careful research of the Penn State group [2.42-2.47] has done much to elucidate our understanding of this problem. Their observations have shown that both bubble and/or vortex cavitation may occur and that blood is similar to the transparent saline surrogates in so far as its cavitation susceptibility is concerned (Stinebring et al. [2.42], Garrison et al. [2.44]). Clearly future improvements in these prostheses will depend on improvements in our understanding of the features that promote or inhibit cavitation as well as an understanding of why they are currently inferior to natural valves. Zapanta et al. [2.47] provide some useful insights in this regard. They found that both the valve geometry and material have significant effects on the cavitation though the leakage clearance did not. It appears that softer materials provide compliance that reduces the magnitude of the low pressures and reduces the cavitation. This may be the reason that natural valves are superior. Clearly there is a need for better understanding of cavitation in the presence of flexible surfaces.

Prosthetic heart valve cavitation is illustrated herein by the photographs of Rambod et al. [2.48] reproduced in Figures 2.24 and 2.25. The growth and collapse of the cavitation both along the central diameter and at the tips can be clearly seen in the sequence in Figure 2.24. Close-ups of these clouds are shown in figure 25. It may be that the fluid used by Rambod et al. [2.48] contained more cavitation nuclei than some other experiments and hence the prevalence of clouds of cavitation bubbles. The photographs of Stinebring et al. [2.42] show smaller clouds as well as individual bubbles. However, in experiments conducted at Carbomedics, cavitation events did not occur during every closure and took the form of occasional single bubbles. This is illustrated in Figure 2.26 where just a few individual cavitation bubbles can be observed near the leaflet tip.

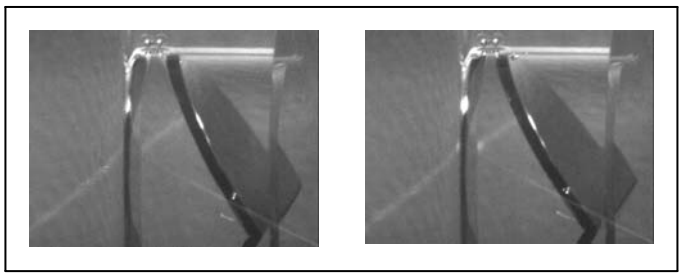

Figure 2.26: Photographs of a heart valve leaflet (the inclined black plate) just before and at closure showing cavitation bubbles just before closure (left) just downstream of leaflet tip (upper left) (courtesy of Carbomedics). The forward flow is from right to left.

Thus it appears that this transient form of cavitation and its consequences may depend not only on the design of the valve and the flow conditions but also on the number of cavitation nuclei present in the fluid and the statistical coincidence of a nucleus with the transient low pressure region. Thus it is clear that more needs to be known about the population of nuclei in the blood.

2.6.1 ARTIFICIAL HEARTS

The present artificial hearts or ventricular assist devices (VADs) have a wide range of fluid flow designs which will only be touched upon here by example. Some, such as the MicroMed deBakey VAD (Figure 2.27), the Jarvik VADs (Figure 2.28) or the Thoratec HeartMate (Figure 2.29) are essentially axial flow pumps; others such as the WorldHeart HeartQuest (Figure 2.30) are centrifugal pumps; still others are more complex pulsatile devices such the Cleveland Clinic Foster-Miller Magscrew or the Abiocor artificial hearts. Since the typical design specific speeds are of the order of 0.5 (non-dimensional units [2.48A] and based on the typical rotational speed of 1000s of revolutions per minute) for this pumping device, the pump designer might ask why all the designs are not of the centrifugal type. The answer is that an artificial heart has a complicated and wide-ranging set of design constraints including size, shape, material compatibility, reliability, minimal shear rates, etc. Different emphases on this wide variety of constraints have led to the wide range of geometries.

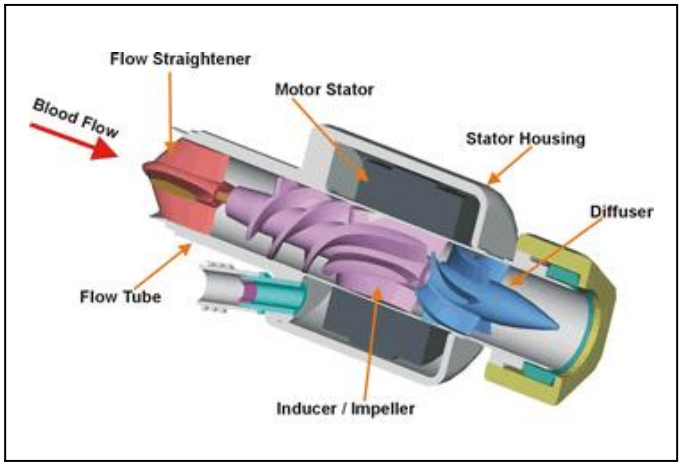

Figure 2.27: The MicroMed deBakey VAD.

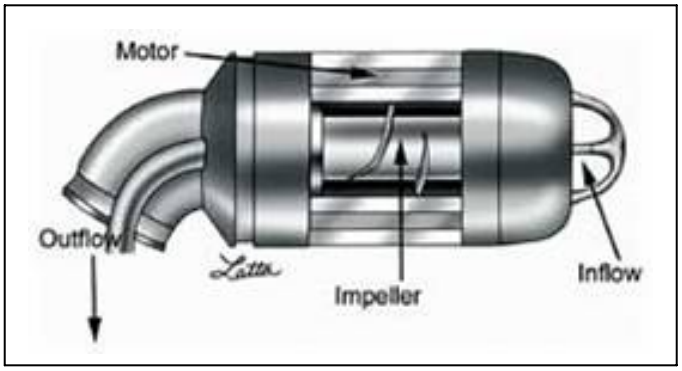

Figure 2.28: The Jarvik 2000 VAD.

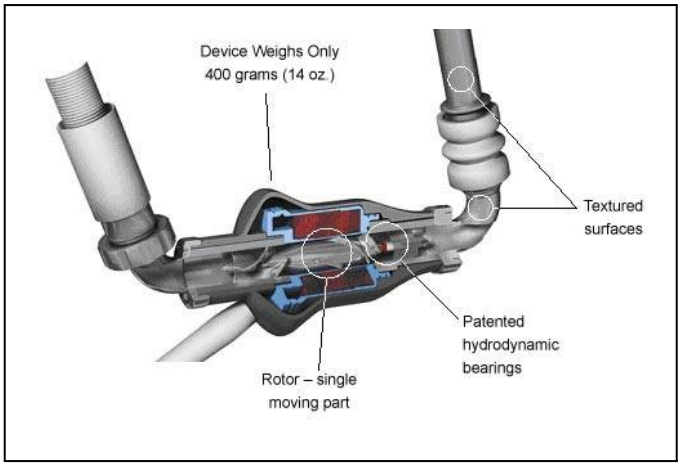

Figure 2.29: The Thoratec Heartmate 11.

A review of all these devices is beyond the scope of this review but some common basic issues are worth mentioning. One key concern is extent to which the device causes hemolysis or the rupture of red blood cells. High shear rates in the flow through the pumps (caused by the high rotation rates of the order of 1000s of rotations per minute) and cavitation can both lead to unacceptable hemolysis. As in the case of the heart valves, more flexible structures might help but most of the current devices use conventional rigid components. Some of the more complex designs generate pulsatile flow but, as with the heart valves, this is likely to increase the cavitation potential. As a result of these complexities, much development remains to be done before these artificial heart designs converge toward an optimal form.

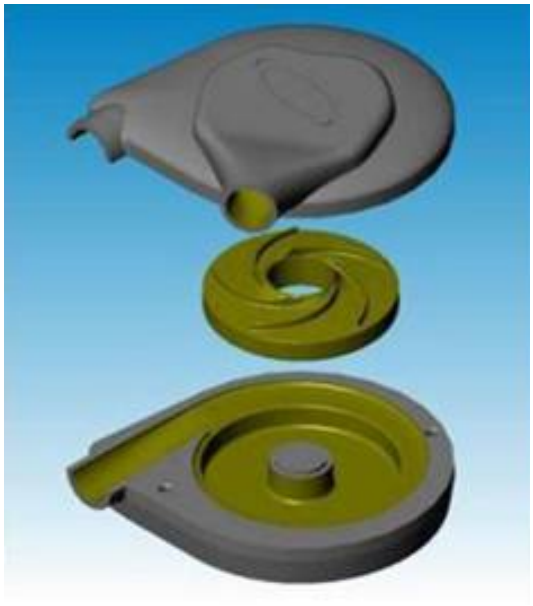

Figure 2.30: The WorldHeart HeartQuest.

2.7 HEAD INJURIES AND WOUNDS

Other subject areas in which the dynamics of cavitation are believed to be important are in head injuries and in wounds caused by high velocity bullets. These are lumped together only because they involve massive trauma and not because the pertinent mechanics are similar.

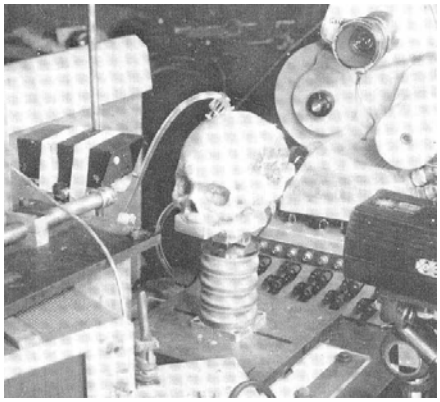

Figure 2.31: Cadaver skull replica used by Lubock and Goldsmith [2.54].

It has long been known that liquid-filled containers can experience cavitation when the container is subject to impact and/or high accelerations. The resulting pressure waves within the liquid cause momentary regions of low pressure within which the liquid may cavitate. In so far as such dynamics are concerned, the skull is effectively a liquid-filled container and, moreover, one which contains delicate structures. Thus, when subject to an external impact, head injuries are often compounded by cavitation of the cerebral fluid. Goldsmith and his coworkers conducted extensive experiments and analyses of the dynamics of head injuries [2.52, 2.53]. The collapse of such cavitation bubbles could cause significant secondary damage during a head injury.

When an approximately spherical liquid-filled container is impacted on one side, thus creating a high pressure in the liquid on that impact side, the subsequent transmission and reflection of the pressure waves can generate low, even negative, pressures at other locations within the container (see, for example, [2.55]). Typically the lowest pressures occur at the contrecoup position on the side opposite the impact. Lubock and Goldsmith [2.54] studied the occurrence of cavitation in these low-pressure zones using both simple spherical shells and cadaver skull replicas (see Figure 2.31). They observed a number of interesting forms of cavitation. An example is shown in Figure 2.32, which illustrates the ring patterns of cavitation bubbles that were observed to occur in water-filled spherical shells. Though cavitation was observed to occur with water, it was not observed when gelatin was used. Consequently, the extent to which cavitation magnifies the damage in head injuries remains uncertain.

The origin of the cavitation damage caused by high velocity bullets is different. When such an object passes through fluid-like tissue it creates a vapor-filled wake, a transient attached cavity. This tends to grow as the bullet progresses; in much the same way as occurs with water-entry cavities [2.56]. Consequently the exit wound is usually much larger than the entrance wound. Harvey [2.7] may have been among the first to investigate such phenomena. Detailed knowledge of these dynamics may help doctors anticipate the forms and areas of serious damage due to bullets and other missiles.

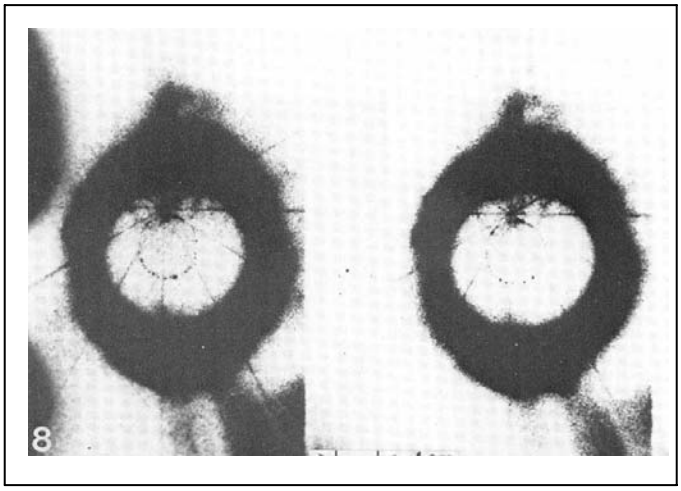

Figure 2.32: Ring patterns of cavitation bubbles in water-filled acrylic spherical head-neck model subjected to impact (from Lubock and Goldsmith [2.54]).

2.8 NUCLEATION SUPPRESSION

Many of the preceding examples have demonstrated the importance of cavitation nucleation sites in biological systems. Though far-fetched, it may therefore be of value to consider ways in which one might be able to control that site population and thereby modify the cavitation characteristics of a device. The author was recently involved with a project in which bubble nucleation suppression was remarkably successful [2.57, 2.58]. The context is a system designed to inject a highly supersaturated aqueous solution of oxygen into the bloodstream in order to minimize tissue damage caused by oxygen deprivation in the aftermath of a heart attack or stroke. The aqueous solution of oxygen is prepared at very high pressure (100s of atmospheres) and then is injected through very small capillaries (100s of micrometers) at high speed (m/s). The trick is to accomplish mixing with the receiving fluid without the formation of gaseous oxygen bubbles; this is achieved as follows.

Because of the high speed and high-pressure gradient within the capillary, only a short length close to the exit has a pressure below the saturation level. Consequently only nucleation sites within this short length have the potential to produce bubbles. Observations [2.57, 2.58] showed that there were typically only of the order of 10 such sites in drawn silica capillaries. Moreover these sites could be deactivated by the simple expedient of flushing ethanol through the capillary while it was underwater. Apparently, the ethanol preferentially wets the interior surface of the site and removes the buried nucleation bubble/site. The ethanol may also help dissolve the gas in the nuclei since the solubility in ethanol is about an order of magnitude larger than the solubility in water.

This process of "ethanolization" of the surface was remarkably successful in suppressing nucleation. Moreover, it was made compatible with medical injection by preparing the capillary with an interior coating of benzalkonium heparin laid down in ethanol.

This remarkably successful example of nucleation suppression suggests that similar strategies might be successfully employed in other contexts though the precise mechanism requires more investigation before it can be thoroughly understood.

2.9 CONCLUSIONS

While this survey has been both episodic and superficial it nevertheless seems to reveal several common themes that, in turn, suggest areas of cavitation research that would prove valuable in the biological and bioengineering contexts:

2.9.1 CONTROL OF CAVITATION

The first (and perhaps most challenging) feature involves the need to control or manage cavitation. It seems clear that the desirability of such control is almost universal. The dual motivations are an increase in the effectiveness of the procedure and a reduction in the collateral damage. However, the methods devised for this control vary greatly. In phaco-emulsification spatial control is sought through the design of the ultrasonic probe and the deployment of additional features such as rotation. In other circumstances, temporal rather than spatial control is attempted. Thus in lithotripsy, multiple pulses are used and more sophisticated strategies such as the Matsumoto et al. sequencing are being investigated. A different temporal control approach is embodied in the picosecond laser pulses of Vogel and his co-workers. It seems clear that much could be gained by exploration of more of these temporal and spatial control strategies especially when the full range of possible bubble and cloud dynamics are taken into account.

2.9.2 STOCHASTIC NATURE OF CAVITATION

Most of the cavitation phenomena described above involve bubble cavitation in transient low-pressure regions. Consequently the cavitation is governed by the coincidence of a nucleation site with the occurrence of that low pressure in space and time. In my opinion we need to know more about these stochastic aspects of cavitation and we need to devise experiments and experimental devices that would allow measurement of these statistical processes.

Of course, a key input to these processes is the distribution of nucleation sites. While much is now known about the nuclei distributions in water, very little is known of their existence in biological fluids or structures [2.48]. It may also be possible to alter or control the nucleation process [2.58] by surface coatings such as described above.

2.9.3 CLOUD CAVITATION

Many of the cavitation phenomena described also involve multiple bubbles or clouds of bubbles in which the interactions between the bubbles are critical to the cavitation dynamics. More needs to be learnt about the collapse of such bubble assemblages especially in the presence of solid structures. An important component of this research will be the ability to accurately simulate these multiphase flows computationally.

2.9.4 FINAL COMMENT

As a final comment, this author was surprised to learn of the wide range of biomedical and bioengineering contexts in which cavitation is utilized for beneficial effect. However, this wide range is very splintered and there is little cross talk that could initiate new strategies and devices. Perhaps the fluids engineering community could play a role in providing some such unifying forum.

ACKNNOWLEDGMENTS

Many individuals provided me with valuable assistance in the preparation of this review, including Tim Colonius, Allan Acosta, Yoichiro Matsumoto, Aziz Anis, Michel Tanguay, Brant Maines, Morteza Gharib, Larry Crum, Tim Baldwin, James Antaki, and Eric Johnsen.

REFERENCES

[2.1] E.N. Harvey, D.K. Barnes, W.D. McElroy, A H. Whiteley, D.C. Pease and K.W. Cooper. (1944). Bubble formation in animals. I. Physical factors. J. Cellular and Comp. Physiol. 24, No.1, 1-22.

[2.2] E.N. Harvey, A.H. Whiteley, W.D. McElroy, D.C. Pease and D.K. Barnes. (1944). Bubble formation in animals. II, Gas nuclei and their distribution in blood and tissues. J. Cellular and Comp. Physiol. 24, No.1, 23-24.

[2.3] E.N. Harvey, D.K. Barnes, W.D. McElroy, A.H. Whiteley and D.C. Pease. (1945). Removal of gas nuclei from liquids and surfaces. J. Amer. Chem. Soc., 67, No.1, 156-157.

[2.4] E.N. Harvey, K.W. Cooper, A.H. Whiteley, D.C. Pease and W.D. McElroy. (1946). Bubble formation within single cells. Biol. Bull. 91, No.2, 236-237.

[2.5] E.N. Harvey, W.D. McElroy and A.H. Whiteley. (1947). On cavity formation in water. J. Appl. Phys. 18, No.2, 162-172.

[2.6] E.N. Harvey. (1945). Decompression sickness and bubble formation in blood and tissues - Harvey lecture. New York Acad. Med. 21, No.10, 505-536.

[2.7] E.N. Harvey. (1948). The mechanism of wounding by high velocity missiles. Proc. Am. Phil. Soc. 92, 294--304.

[2.8] M.R. Bailey, V.A. Khokhlova, O.A. Sapozhnikov, S.G. Kargl and L.A. Crum. (2003). Physical mechanisms of the therapeutic effect of ultrasound (a review). Acoust. Phys. 49, No.4, 437-464.

[2.9] S. Vaezy, R. Martin, P. Mourad and L.A. Crum. (1999). Hemostasis using high intensity focused ultrasound. European J. Ultrasound, 9, 79-87.

[2.10] S. Vaezy, R. Martin, U. Schmiedl, M. Caps, S. Taylor, K. Beach, S. Carter, G. Kaczkowski, G. Keilman, S. Helton, W. Chandler, P. Mourad, M. Rice, R. Roy and L.A. Crum. (1997). Liver hemostasis using high intensity focused ultrasound. Ultrasound in Med. and Biol., 23, 1413-1420.

[2.11] S. Vaezy, R. Martin, G. Keilman, G. Kaczkowski, E. Chi, E. Yaziji, M. Caps, S. Poliachik, S. Carter, S. Sharar, C. Cornejo L.A. Crum. (1999). Control of splenic bleeding using high intensity ultrasound. J. Trauma, 47, 521-525.

[2.12] A.R. Williams. (1983). Ultrasound: biological effects and potential hazards. Academic Press.

[2.13] http://www.dentsply.co.uk/products/products/cavitronselect.htm

[2.14] C.D. Kelman. (1967). Phaco-emulsification and aspiration; a new technique of cataract removal; a preliminary report. Amer. J. Ophthalmol., 64, 23-35.

[2.15] L.B. Sabbagh. (1999). Lasers in phaco: challenging the standard. http://www.revophth.com/1999/November_articles/1199%20phaco.htm

[2.16] FDA CDRH (1996). FDA Center for Devices and Radiological Health, Office of Science and Technology Annual Report, Section 18. http://www.fda.gov/cdrh/ost/index.html

[2.17] A.Y. Anis. (2003) Personal communication.

[2.18] A.Y. Anis. (1999) PhacoTmesis. Chapter 12 in Atlas of Cataract Surgery (eds: S. Masket and A.S. Crandall), 89-96, Martin Dunitz.

[2.19] FDA CDRH (1997). FDA Centre for Devices and Radiological Health, Office of Science and Technology Annual Report, http://www.fda.gov/cdrh/ost/rpt97/OST1997AR75.html

[2.20] S.L. Ceccio and C.E. Brennen, (1991). Observations of the dynamics and acoustics of travelling bubble cavitation. J. Fluid Mech., 233, 633-660.
[2.21] C.E. Brennen, (1995). Cavitation and bubble dynamics. Oxford Univ. Press.
[2.22] C. Chaussy, W. Brendel and E. Schmiedt, (1980). Extracorporeally induced destruction of kidney stones by shock waves. Lancet , 1265-1268.
[2.23] W. Eisenmenger. (2001). The mechanisms of stone fragmentation in ESWL. Ultrasound in Med. & Biol., 27. No. 5, 683-693.
[2.24] S. Zhu, F.H. Cocks, G.M. Preminger and P. Zhong. (2002). The role of stress waves and cavitation in stone comminution in shock wave lithotripsy. Ultrasound in Med. & Biol., 28, No. 5, 661-671.
[2.25] A.J. Coleman, J.E. Saunders, L.A. Crum and M. Dyson. (1987). Acoustic cavitation generated by an extra corporeal shockwave lithotripter. Ultrasound Med. & Biol., 13, 69-76.
[2.26] B. Sturtevant. 1996. Shock wave physics of lithotripters. In Smith's Textbook of Endourology, Quality Medical , St. Louis, 529-552.
[2.27] Bailey, M.R., McAteer, J.A., Pishchalnikov, Y.A., Hamilton. M.F. and Colonius, T. (2006). Progress in lithotripsy research. Acoustics Today, April 2006, 18-29.
[2.28] Y. Matsumoto, J. Allen, S. Yoshizawa, T. Ikeda and Y. Kaneko. (2003). Renal stone communition utilizing cavitation erosion. Manuscript in preparation.
[2.29] D.L. Sokolov, M.R. Bailey and L.A. Crum. (2001). Use of a dual-pulse lithotripter to generate a localized and intensified cavitation field. J. Acoust. Soc. Amer., 110, No.3, 1685-1695.
[2.30] Y.C. Wang and C.E. Brennen. (1994). Shock wave development in the collapse of a cloud of bubbles. ASME Cavitation and Multiphase Flow Forum, 1994, FED-194, 15-20.
[2.31] Y.C. Wang and C.E. Brennen. (1999). Numerical computation of shock waves in a spherical cloud of cavitation bubbles. ASME J. Fluids Eng . 121, 872-880.
[2.32] M. Tanguay and T. Colonius. (2002). Numerical investigation of bubble cloud dynamics in shock wave lithotripsy. Proc. ASME Fluids Eng. Div. Summer Meeting, FEDSM2002-31010.
[2.33] R.F. Paterson, D.A. Lifshitz, A.P. Lingeman, B.A. Evan, J.C. Connors, J.C.jnr. Williams and J.A. McAteer. (2002). Stone fragmentation during shock wave lithotripsy is improved by slowing the shock wave rate: Studies with a new animal model. J. Urol., 168, 2211-2215.
[2.34] F. Fankhauser, P. Rousel, J. Steffen, E. Van der Zypen, and A. Chrenkova. (1981). Clinical studies on the efficiency of high power laser radiation upon some structures of the anterior segment of the eye. Int. Opthalmol., 3, 129-139.
[2.35] D. Aron-Rosa, J.J. Aron, M. Griesemann and R. Thyzel. (1980). Use of the Nd:YAG laser to open the posterior capsule after lens implant surgery: a preliminary report. Am. Intraocul. Implant Soc. J., 6, 352-354.
[2.36] R.F. Steinert and C.A. Puliafito. (1985). The Nd:YAG laser in Ophthalmology, Saunders.
[2.37] A. Vogel, W. Lauterborn, and R. Timm. (1989). Optical and acoustical investigations of the dynamics of laser-produced cavitation bubbles near a solid boundary. J. Fluid Mech., 206, 299-338.
[2.38] A. Vogel and S. Busch. (1994). Time-resolved measurements of shock wave emission and cavitation-bubble generation in intraocular laser surgery with ps- and ns-pulses. In Bubble Dynamics and Interface Phenomena (eds: J.R.Blake et al.), Kluwer Acad. Publ., 105-117.
[2.39] R. Steiner. (ed.) (1988). Laser lithotripsy. Proc. 1st Int. Symp. on Laser Lithotripsy, Springer.
[2.40] S. Krishnamurthy and S.K. Powers. (1994). Lasers in neurosurgery. Lasers in Surg. and Med., 15, No.2, 126-167.
[2.41] D.S.J. Choy. (1998). Percutaneous laser disc decompression (PLDD): Twelve years' experience with 752 procedures in 518 patients. J. Clin. Laser Med. & Surg., 16, No.6, 325-331.
[2.42] D.R. Stinebring, T.C. Lamson and S. Deutsch. (1991). Techniques for in vitro observation of cavitation in prosthetic heart valves. ASME Cavitation and Multiphase Flow, FED-109, 119-124.
[2.43] T.C. Lamson, G. Rosenberg, D.B. Geselowitz, S. Deutsch, D.R. Stinebring, J.A. Frangos and J.M. Tarbell. (1993). Relative blood damage in the three phases of a prosthetic heart valve flow cycle. ASAIO J., 39, No.3, M626-M633.
[2.44] L.A. Garrison, T.C. Lamson, S. Deutsch, D.B. Geselowitz, R.P. Gaumond and J.M. Tarbell. (1994). An in vitro investigation of prosthetic heart valve cavitation in blood. J. Heart Valve Dis., 3, Suppl.1, S8-S24.
[2.45] D.R. Stinebring, S. Deutsch, D.S. Sneckenberger, C. Zapanta and J.M. Tarbell, (1995). Investigations of cavitation in prosthetic heart valves. ASME Cavitation and Multiphase Flow, FED-210, 95-103.
[2.46] C.M. Zapanta, D.R. Stinebring, D.S. Sneckenberger, S. Deutsch, D.B. Geselowitz, J.M. Tarbell, A.J. Snyder, G. Rosenberg, W.J. Weiss, W.E. Pae and W.S. Pierce, W.S. (1996). In vivo observation of cavitation in prosthetic heart valves. ASIAO J., 42 (5), M550-M554.
[2.47] C.M. Zapanta, D.R. Stinebring, S. Deutsch, D.B. Geselowitz and J.M. Tarbell. (1998). A comparison of the cavitation potential of prosthetic heart valves based on valve closing dynamics. J. Heart Valve Dis., 7, No.6, 655-667.
[2.48] E. Rambod, M. Beizaie, M. Shusser, S. Milo and M. Gharib. (1999). A physical model describing the mechanism for formation of gas microbubbles in patients with mitral mechanical heart valves. Ann. Biomed. Eng., 27, 774--792.
[2.49] B.H. Maines and C.E. Brennen. (2002). Applicability of fluid transient test methods for mechanical heart valve cavitation scaling. Sixth Annual Hilton Head Workshop sponsored by the Parker Institute for Bioengineering and Bioscience. Prosthetic Heart Valves: Past, Present and Future.
[2.50] S.D. Chambers, R.H. Bartlett and S.L. Ceccio. (2000). Hemolytic potential of hydrodynamic cavitation. ASME J. Biomech. Eng., 122, No.4, 321-326.
[2.51] C.E. Brennen. (1994). Hydrodynamics of pumps. Concepts ETI and Oxford University Press.
[2.52] W. Goldsmith. (2001). The state of head injury biomechanics: past, present and future: part 1. Crit. Rev. Biomed. Eng., 29 (5 & 6), 441-600.
[2.53] W. Goldsmith. (1972). Biomechanics of head injury. Chap.23, 585-634, in Biomechanics, Its Foundations and Objectives, eds: Y.C.Fung, N.Perrone and M.Anliker, Prentice-Hall.

[2.54] P. Lubock and W. Goldsmith. (1980). Experimental cavitation studies in a model head-neck system. J. Biomech., 13, 1041-1052.
[2.55] J.V. Benedict, E.H. Harris and D.U. Von Rosenberg. (1970). An analytical investigation of the cavitation hypothesis of brain damage. ASME J. Basic Eng., Sept.1970, 597-603.
[2.56] R.T. Knapp, J.W. Daily and F.G. Hammitt. (1970). Cavitation. McGraw-Hill.
[2.57] C.E. Brennen. (2002). Micro-nucleation in supersaturated oxygen solution injection. Proc. JSME Mech. Eng. Congr., 18-19.
[2.58] I. Creech, V. Divino, W. Patterson, P.J. Zalesky. and C.E. Brennen. (2002). Injection of highly supersaturated oxygen solutions without nucleation. ASME J. Biomed. Eng., 124, No.6, 676-683.

Invited Lecture

3.6 THERAPEUTIC APPLICATION OF ACOUSTIC CAVITATION

Professor Y. Matsumoto
Department of Mechanical Engineering, The University of Tokyo
ymats@mech.t.u-tokyo.ac.jp

ABSTRACT

Medical applications of ultrasound such as High Intensity Focused Ultrasound (HIFU), Extracorporeal Shock Wave Lithotripsy (ESWL) and ultrasound contrast agent imaging have recently been the subject of much interest. In these applications, acoustic cavitation facilitates the medical treatment by improving the image quality or enhancing the therapeutic effects through localized heating, erosion or acoustic emission. In ultrasound imaging, the harmonic and subharmonic responses from the cavitating bubbles assist in distinguishing the acoustic scattering of blood from that of the surrounding tissue. In HIFU treatment, the heat generated by the bubble motion contributes an enhanced localized heating effect from the ultrasound. In Extracorporeal Ultrasound Lithotripsy, acoustic cloud cavitation contributes to the comminution of renal stones. In all these applications, it is essential to understand the cavitation phenomena, including bubble and bubble cloud dynamics. The bubble motion and bubble cloud behavior are strongly influenced by the internal phenomena of thermal diffusion, mist formation, mass diffusion and heat and mass transfer through the bubble wall. In this paper, medical applications of microbubbles and acoustic cavitation in the above areas are highlighted.

3.1 INTRODUCTION

Ultrasound and pressure waves are widely applied in the clinical setting, for example diagnostic ultrasound, High Intensity Focused Ultrasound (HIFU), Extracorporeal Shock Wave Lithotripsy (ESWL) and sonodynamic therapy. Some of these applications depend strongly on cavitation, the dynamic behavior of microbubbles and that of bubble clouds. In ultrasound imaging, microbubbles are used as contrast agents, while in HIFU treatment they are used to enhance the heating of the tissues. However acoustic cavitation generated by high amplitude ultrasound may cause tissue trauma, and the optimal acoustic parameters need to be determined. Acoustic cloud cavitation also has a close relationship with the efficiency of Extracorporeal Lithotripsy. There is a need to better understand the amplitude and the power spectrum of acoustic emission from microbubbles to visualize tissues and organs, to determine the heat deposition rate for the treatment of tumors and to find the emitted shock pressure from the collapsing bubble cloud.

Many researchers have investigated single spherical bubble motion in an infinite liquid and there has been also research considering additional effects, such as compressibility of the liquid, bubble deformation from the spherical shape near a solid wall and thermal phenomena. It is well understood that the thermal phenomena inside the bubble significantly influence the bubble motion. The effects of non-equilibrium phase change [3.1] and thermal diffusion [3.2,3.3] on the bubble motion have been discussed. Bubble motions [3.4,3.5] have been calculated numerically by using the full equations for mass, momentum and energy in the gas and liquid phases taking into account the internal phenomena such as thermal and mass diffusion and mist formation due to homogeneous condensation. Not only single bubble dynamics but

also bubble cloud dynamics have been investigated [3.6–3.11]. Reisman et al. [3.9] suggested that the formation and focusing of bubbly shock waves, which are formed during the collapse of a cloud, are responsible for the severe noise and damage associated with cloud cavitation. The behavior of cavitation clouds has been investigated in connection with severe cavitation damage [3.10,3.11] using the set of governing equations for spherical bubble cloud, where the internal phenomena of each bubble and compressibility of the liquid are taken into account. An inwardly-propagating shock wave is formed during the collapse of the bubble cloud and focused at the cloud center [3.11]. These phenomena are utilized in medical applications [3.12, 3.13].

In this paper, new methods for medical ultrasound with microbubbles based on previous research in other contexts are discussed. One is the localized enhancement of heating for HIFU therapy using contrast agent microbubbles, and another is Cavitation Control Lithotripsy (CCL) of renal calculi using a method of acoustic cavitation control.

3.2 MICROBUBBLE ENHANCED HIGH INTENSITY FOCUSED ULTRASOUND

High Intensity Focused Ultrasound (HIFU) is used in the treatment of tumors [3.14,3.15], whereas the use of microbubbles in medical ultrasound applications like ultrasound imaging and sonodynamic therapy [3.16] have been investigated and applied. Recently, microbubbles have attracted much attention as heat transducers in medical ultrasound applications [3.17,3.18]. There are reports of the *in vivo* enhancement of tissue heating by the acoustic cavitation produced by HIFU [3.14] and contrast agents [3.19]. In the field of bubble dynamics, it is known that the microbubble is a converter of mechanical energy to heat when subjected to an acoustic field. If the heat deposited from microbubbles can be effectively utilized, the treatment for a tumor can be achieved with less intense ultrasound, and accordingly a less invasive and more effective therapy might be developed.

In order to achieve a more effective use of microbubbles, we need to better comprehend the behavior of the microbubbles and cavitation bubbles in the ultrasound field.

3.2.1 HEATING EFFECT OF MICROBUBBLES

In this section, some results of experiments are shown and the heating effect of microbubbles is discussed. Figure 3.1 shows the experimental set-up [3.20]. The concave PZT ceramic diaphragm with a natural frequency of 2.2 MHz is used as the ultrasound transducer. The diameter of the transducer is 40 mm, and the focal length is also 40 mm. Polyacrylamide gel is placed in the ultrasound field. In the gel a cylindrical space whose depth is 10 mm and diameter is 10 mm is created, into which pure water or water with Levovist^{TM} is injected. Levovist^{TM} is a contrast agent with mean bubble diameter of 1.3 αm and whose internal gas is air. It is made by dissolving galactose, so the density of microbubbles is controlled by changing the amount of the galactose. The temperature at the focus is measured by a thermocouple; the initial temperature of the test section is fixed at 37 °C.

Figure 3.2 shows the time history of the temperature at the focus. In this figure, α represents the void fraction at the ultrasound focal region. The intensity of ultrasound (I_{SPTA}) is 1200 W/cm^2 and the irradiation time is 60s. The graph shows that increasing the void fraction increase the temperature rise. Figure 3.3 shows the relation between the number density of bubbles and the temperature rise. In this graph, the temperature rises linearly in the region of low density. As the density becomes larger, the rise in temperature becomes saturated. It is hypothesized that other phenomena occur in this region above a certain density. One possibility is a shielding effect of microbubbles acting as a bubble cloud as has been hypothesized previously [3.17].

3.2.2 TEMPERATURE DISTRIBUTION IN THE MEDIUM CONTAINING MICROBUBBLES

In this section, the temperature distribution in the medium containing the microbubble contrast agents is analyzed. The position, shape and volume of the high temperature region are observed. Figure 3.4 shows the experimental setup [3.21]. The diameter of the piezoelectric transducer is 40 mm and the focal length is 40 mm. The frequency is 2.2

MHz, the intensity (I_{SPTA}) is 340 W/cm^2 and the irradiation time is 60 s. A polyacrylamide gel, containing the microbubble contrast agent is placed in the ultrasound field. The water containing Levovist^{TM} is mixed into a polyacrylamide solution. It is solidified before the microbubbles float creating a gel with microbubbles. A thermal liquid crystal (TLC) sheet is put in the middle of the gel in order to visualize the temperature distribution inside it. The color of the liquid crystal changes to red, green and blue as the temperature rises. The TLC sheet has a temperature sensitivity of from 50°C to 60°C. The temperature of the surrounding water is kept to 37 °C. A video camera (30 fps, 720 x 480 pixels) is set above the test section to recode the temperature distribution.

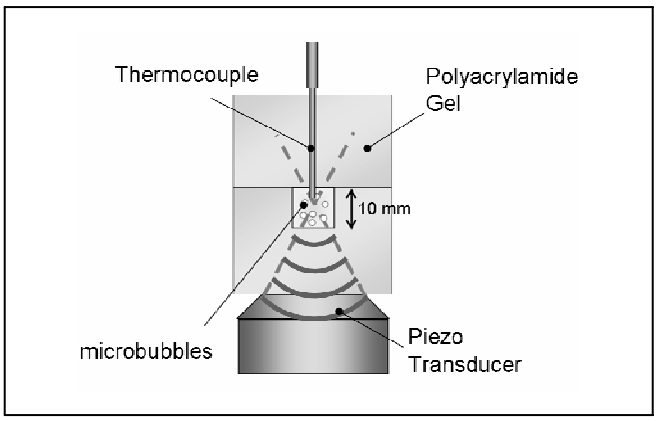

Figure 3.1: Setup of the microbubble heating experiment.

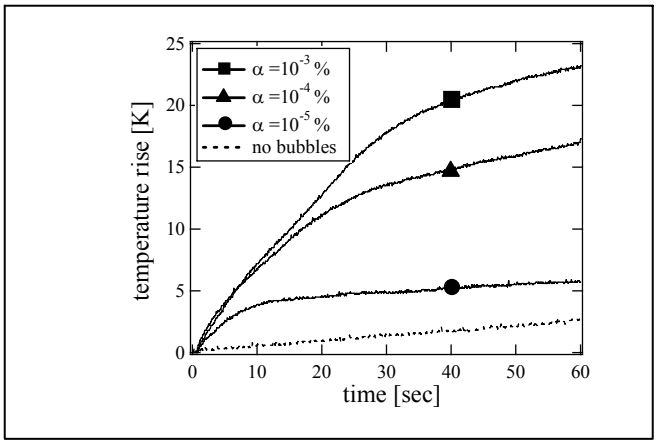

Figure 3.2: Time history of the temperature at the focus.

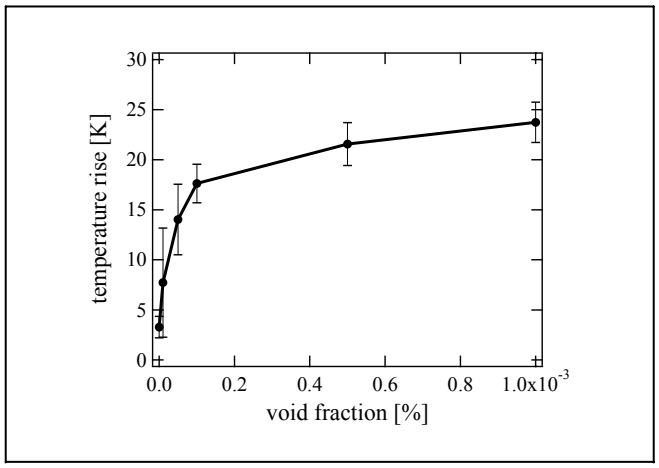

Figure 3.3. Relationship between the void fraction and the temperature rise.

Figure 3.5 shows the time history of the temperature distribution in the gel and we now analyze the relationship between the number density of microbubbles, which is represented by the void fraction α, and the temperature distribution in the medium. The ratio α of total gas volume to that of the gel (void fraction) and the experiments were conducted under the following conditions: (i) α =0 %, (ii) α =10^{-5} %, (iii) □ =10^{-4} % and (iv) α =10^{-3} %.

In the case of no bubbles (case (i)), the shape of the high temperature region is almost elliptical at the focal point. In cases (ii) and (iii), the shape is more complicated, resembling a circular cone. The position of the high temperature region shifts to the front of the geometric focal point. This is because the microbubbles oscillate and radiate heat energy around them, and the attenuation effect of the ultrasound becomes larger. In the case of too many bubbles (case (iv)), the temperature at the geometric focal region does not become so high. The attenuation effect of the ultrasound is too large, and most of the ultrasound is absorbed near the surface of the transducer.

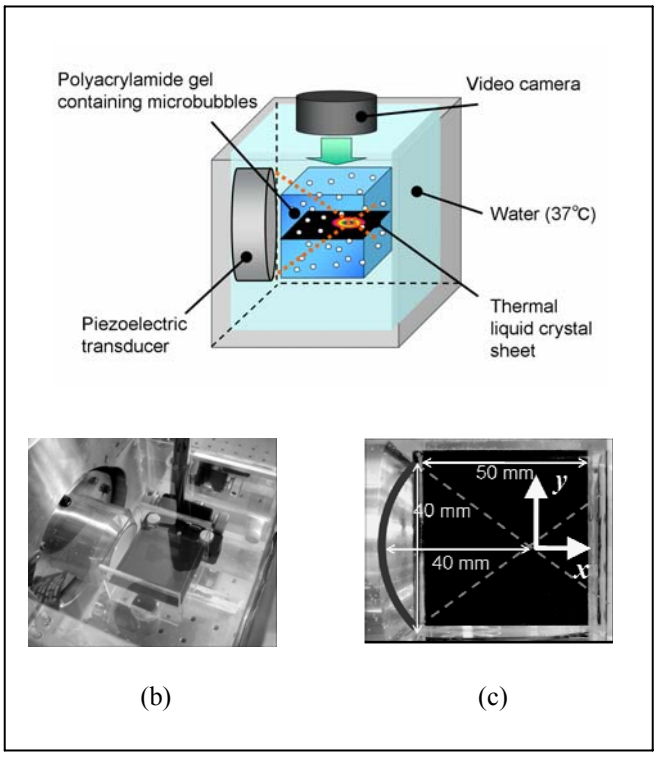

Figure 3.4: Experimental setup. (a) Schematic of the experimental system. (b) A photograph of the test section. (c) Thermal liquid crystal sheet in the water tank.

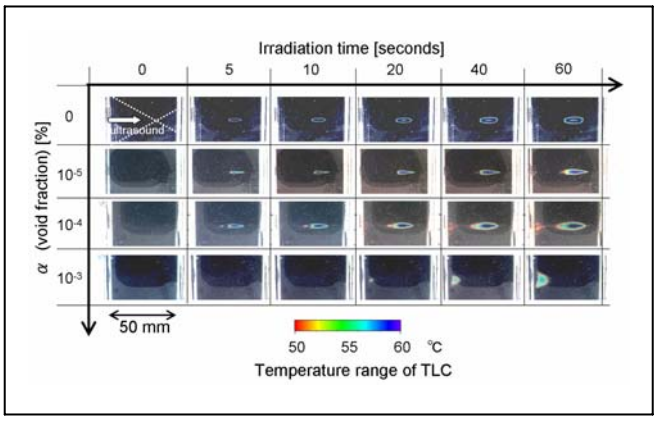

Figure 3.5: Temperature distribution in the gel containing microbubbles after 60 seconds HIFU irradiation

3.3 EXTRACORPOREAL FOCUSED ULTRASOUND LITHOTRIPSY (CAVITATION CONTROL LITHOTRIPSY: CCL)

In the HIFU application, high intensity ultrasound causes acoustic cavitation near the focal area. The violent collapse of the cavitation bubbles has the potential of inducing tissue trauma [3.22], especially in the case in which the bubbles form a cloud, although the collapsing process is not well understood. A maximum pressure in the cloud of the order of GPa has been reported both in numerical [3.13] and experimental [3.23] studies in other fields. On the other hand, the complex effects of cavitation have been known since the early stage of ESWL research history [3.24] and many researchers have investigated the role of the cavitation in ESWL. These studies were conducted on the tissue damage [3.22], and on the acceleration of the stone comminution [3.25]. Recently, cavitation control techniques using novel shock wave combinations have been proposed, and effective results have been achieved [3.26,3.27]. However, the main force that breaks the stone is still considered to be the incident plane shock wave, which has a 10-60 mm focal region. Moreover, the cavitation collapse is thought to only complement the stone comminution process. If the cavitation phenomena are well controlled in time and space to occur only at the stone surface, the extremely high-energy and high-pressure concentration can be utilized as the main mechanism of renal stone disintegration.

By utilizing two-frequency ultrasound, Extracorporeal Focused Ultrasound Lithotripsy (Cavitation Control Lithotripsy: CCL) is being developed. This method can erode and chip away the renal stone by the violent collapse that is induced by the HIFU. The cavitation phenomena are well controlled in time and space to occur only at the stone surface. Thus, the sole contribution to the stone disintegration is cavitation erosion. In this section, the concept of the method and the phenomena in the CCL protocol are explained and the results of the stone crushing are also discussed.

3.3.1 SCHEMATICS OF ACOUSTIC CAVITATION CONTROL

Figure 3.6 shows a schematic of Cavitation Control Lithotripsy (CCL) [3.13, 3.28, 3.29]. The CCL method is comprised of two different frequencies of ultrasound. First, higher frequency ultrasound is focused at the stone surface (Figure 3.6-3.1), with a range of about 1–15 MHz so as to have a shorter wavelength than the characteristic length of the renal stone. This creates a hemispherical bubble cloud consisting of very tiny bubbles existing only at the stone surface (Figure

3.6-3.2). Immediately after the higher frequency ultrasound is stopped, a short pulse of lower frequency ultrasound (100 kHz–1 MHz) is focused at the hemispherical bubble cloud (Figure 3.6-3.3). The lower pulse forces the bubble cloud to oscillate at near resonance frequency (Figure 3.6-3.4). Accompanying the forced oscillation of the bubble cloud, a shock wave propagates inwards in the hemispherical bubble cloud [3.11, 3.30] (Figure 3.6-3.5). The bubbles near the center of the cloud collapse violently and emit an extremely high-pressure wave that reaches the order of GPa [3.11]. Therefore, stone erosion is restricted to the stone surface and the stone is crushed with a high-energy concentration and with the minimum amount of cavitation resulting in scoop-like indentations (Figure 3.6).

Figure 3.7 is the typical CCL ultrasound waveform. As indicated previously, the high frequency ultrasound (bubble cloud creator) is immediately followed by the low frequency ultrasound (cloud collapse inducer). The interval time should be long enough to dissolve all of the cavitation bubbles into the liquid. If this scheme can be finely controlled within the cavitation area in space and the occurrence time of the bubble cloud collapse, a lithotripsy method utilizing only cavitation erosion might be developed that produces less tissue damage and smaller stone fragments than conventional ESWL.

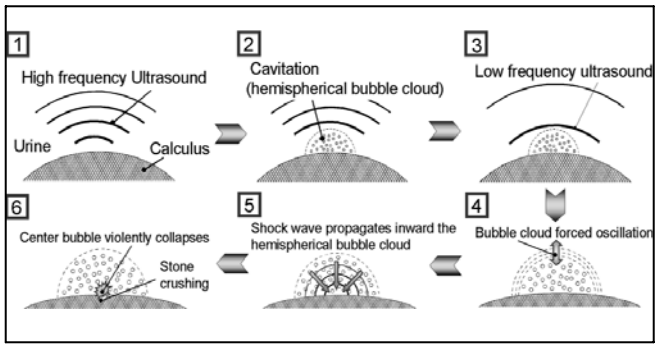

Figure 3.6. Schematic of cloud cavitation control.

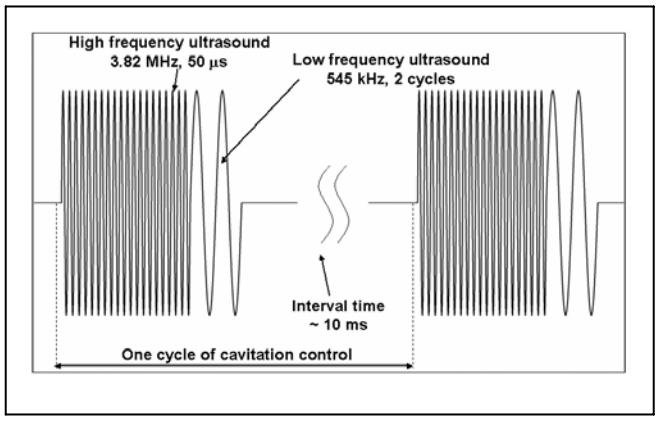

Figure 3.7. Typical cavitation control waveform using two-frequency ultrasound.

3.3.2 BEHAVIOR OF THE BUBBLE CLOUD IN CCL

In this section, the observed bubble cloud phenomena in the CCL cycle are discussed. Figure 8 shows the experimental set-up. A concave PZT ceramic diaphragm with a natural frequency of 545 kHz is used for the ultrasound transducer. It transmits a higher amplitude of ultrasound at the frequencies of (2n+l) times the fundamental frequencies. Appropriate higher-order harmonics coupled with the fundamental frequency is used to realize the CCL waveform (Figure 3.7). The maximum output voltage of CCL waveform is 1.6 kV in its peak-to-peak amplitude. An aluminum ball or artificial stone is used as the crushing test material of the ESWL machine, and is fixed at the focus point. The cavitation phenomena at the focal point of the ultrasound are photographed by an ultra high-speed camera (IMACON200, DRS Hadland), with the ability to take 16 frames with 5 ns exposure time and 5 ns minimum frame interval. An IMOTEC needle hydrophone is placed near the focal region to detect the synchronized signal of the shock wave emitted by the cavitation collapse.

<u>High frequency focusing phase: a stable bubble cloud</u>

Figure 3.9 shows photographs of the bubble cloud in forced oscillation. Immediately after 100 μs irradiation of 2.74 MHz ultrasound, a 545 kHz pulsed ultrasound is focused upon the cloud. As shown in the first frame of Figure 3.9, after 100-200 μs irradiation of the 2.74 MHz ultrasound, a stable bubble cloud appears. As the bubble cloud grows in

size, almost the entire pressure wave is scattered at its surface, so this does not proceed into the cavitation cloud. At some point, the bubble cloud stops growing and so reaches a stable size. The stable bubble cloud is observed for various ultrasound frequencies, and there is a strong relationship between the size of the bubble cloud and the ultrasound wavelength [3.29]. Because the standing wave field at the focal point is created by the incident and reflected ultrasound wave, the size of stable bubble cloud is considered to be dependent on the wavelength of ultrasound. This indicates that the size of the area of the bubble cloud can be controlled by the ultrasound frequency, that is, in the focused ultrasound field; acoustic cavitation at the solid surface can be spatially well controlled.

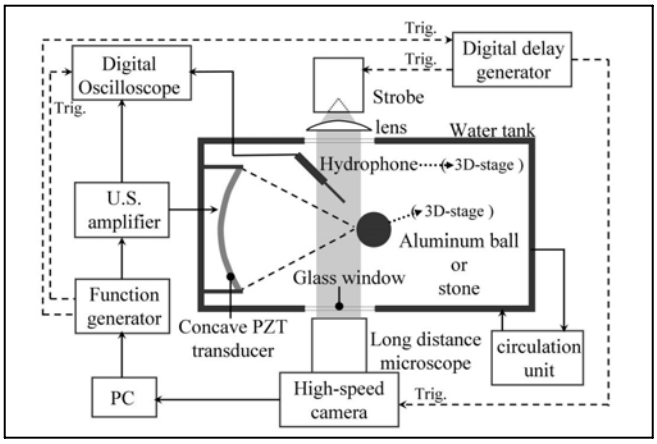

Figure 3.8. Setup of the acoustic cavitation experiment.

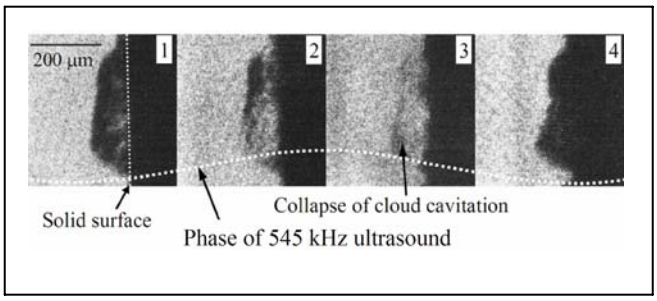

Figure 3.9. Forced collapse of cloud cavitation.

Low frequency focusing phase: Collapse of the bubble cloud

Figure 3.10 also shows the stable bubble cloud forced to collapse by the 545 kHz ultrasound. The bubble cloud shrinks at the positive phase of the 545 kHz ultrasound by decreasing each bubble radius, and as seen in the 3rd frame of Figure 3.9, the bubble cloud collapses. Shadowgraph photography of the cloud collapse is shown in Figure 3.10, in which the shock wave propagation from the bubble cloud is observed. Figure 3.10 corresponds to the phenomena that occurred immediately after the third frame of Figure 3.9, for a different frequency; a strong shock wave propagating outward from the bubble cloud is seen. Figure 3.11 shows the acoustic signal taken 1.6 mm away from the focal point. The shock wave signal of the cloud cavitation collapse is captured at about 3.3 μs. The maximum pressure at this distance is about 3 MPa. The standard deviation of the occurrence time of the peak amplitude is 65 ns; the reproducibility of the cloud collapsing phenomena is very high.

It is concluded that cloud cavitation collapsing phenomena can be well controlled in time and space with a high pressure and energy concentration at the solid surface.

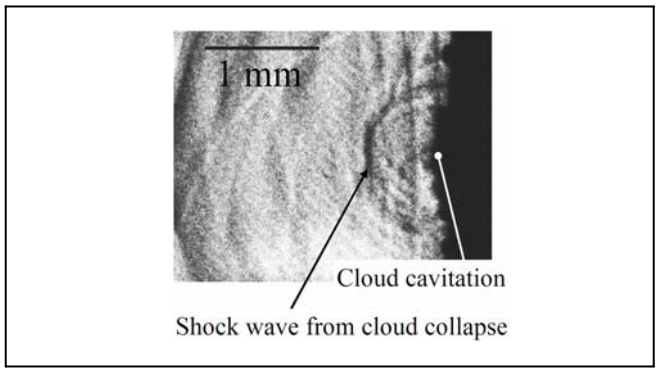

Figure 3.10. Shadowgraph photography of the shock wave emitted from the cloud cavitation.

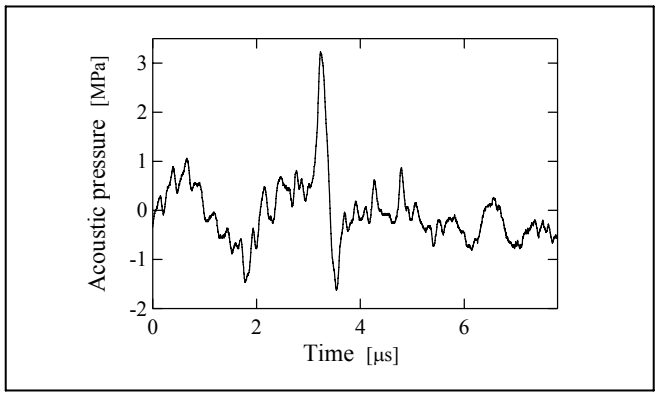

Figure 3.11. Shockwave signal of the cloud cavitation.

3.3.3 IN VITRO STONE CRUSHING TESTS

In this section, crushing tests of model stones used as the test materials of ESWL machines are discussed. The repetition frequency of the ultrasound pulse and the amplifier voltage are fixed at 20 Hz and 1.6 kV (peak-to-peak).

To investigate the advantages of the CCL method, three types of waveform are applied to the cylindrical model stones. The waveforms used are (a) high frequency, (b) low frequency and (c) high and low frequency combination (CCL waveform; Figure 3.7), and Figure 3.12 shows the results. For case (a), little erosion is visible reaching a depth of 1 mm. In case (b), more erosion is visible than in (a), at a depth of 2 mm. Two cycles of low frequency follow the high frequency 50 μs irradiation in (c), and the depth of the scoop indentation reaches 6 mm. In this case, a very acute hole is created by the cloud cavitation collapse. These results show that by controlling acoustic cavitation, high-pressure and high-energy concentration is realized within fine spatial and timing resolutions. The estimated total break up time by CCL is comparable to the conventional ESWL methods. Also the resulting fragments are small enough (~ 1 mm) to pass through the urethra.

Figure 3.13 shows natural kidney stones after the irradiation of ultrasound: they are a Cystine stone and a Staghorn stone. The waveform is the same as in the case of Figure 3.12 and the PRF of the cycle is 25 Hz. The upper photographs in Figure 3.13 are the eroded stones and their fragments: (a) Cystine stone, (b) Staghorn stone. Erosion holes can be seen both in Fig. 12 (a) and (b). The fragment size is of the order of 1 mm for both stones. The lower figures are the size-frequency of a number-size distribution of fragments diameter, D_p, for (a) the Cystine stone and (b) the Staghorn stone. The D_p is calculated from the binary processed image of photographed stone fragments. From the area and the peripheral length of the particles, the area-equivalent diameter, D_p, is calculated for each particle. For the Cystine stone the mean diameter is 0.13 ± 0.070 mm for 756 particles while for the Staghorn stone it is 0.187 ± 0.120 mm for 1393 particles. Every Cystine stone particle is less than 0.8 mm while in the case of the Staghorn stone, almost all are less than 1.0 mm, although three particles of D_p =1.2 mm and one particle of D_p =1.5 mm are observed.

The size distributions for each stone have slightly different characteristics. The Staghorn stone fragments have typical size-frequency distribution of particles with a long tail in the direction of increasing particle size. The Cystine stone's distribution also has a long tail for large particle sizes, whereas the small size fragments do not have one local maximum. This is possibly because very small particles could not be completely collected since the convection of the water in the tank could mean that they did not all fall into the beaker placed just beneath the stone.

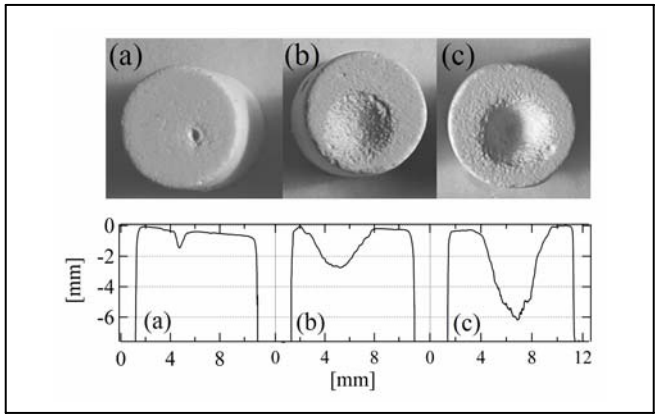

Figure 3.12. Model stone crushing test (a) high frequency only (b) low frequency only (c) CCL waveform.

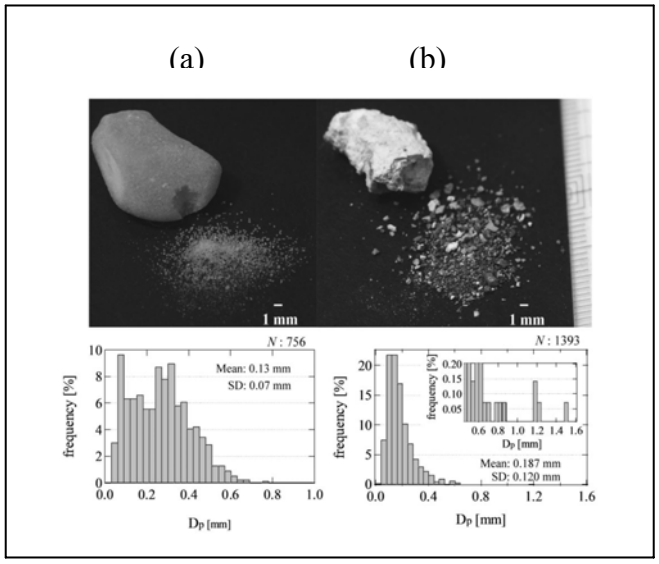

Figure 3.13. Natural kidney stones and fragments after the irradiation of CCL waveform.

3.4 CONCLUSIONS

Both in diagnostic and therapeutic ultrasound, applications of microbubble and acoustic cavitation have recently been the subjects of much interest. New methods for medical ultrasound therapies with microbubbles based on their nonlinear dynamics were outlined. One was the localized enhancement of heating for HIFU therapy using a microbubble contrast agent, and the other was Cavitation Control Lithotripsy (CCL) for renal stone disintegration using a method of acoustic cavitation control.

The heat deposited near a bubble in the ultrasound field can be utilized for the localized enhancement of heating in HIFU treatment. Injecting microbubbles at the ultrasound focal region and enhancing the acoustic cavitation leads to more effective heating of the region compared with ultrasound alone. The temperature rise is saturated above a certain density of bubbles.

An extracorporeal lithotripsy method, Cavitation Control Lithotripsy (CCL) is being developed by utilizing two-frequency focused ultrasound. By controlling cloud cavitation phenomena, high-energy and high-pressure concentrations at the stone surface were obtained. The cavitation phenomena were well controlled both in time and space. The occurrence time of the bubble cloud collapse can be controlled with high reproducibility, and the cavitation area that is generated by high frequency ultrasound can be controlled to be in a restricted area at the stone surface. The model stone is efficiently eroded and the stone comminution mechanism is attributed solely to the cavitation erosion. Compared with conventional ESWL, the spatial range of cavitation is narrower and the input energy is also smaller. The CCL method has the potential to provide a less invasive and more controllable lithotripsy system.

REFERENCES

[3.1] S. Fujikawa, T. Akamatsu, E□ect of the non-equilibrium condensation of vapour on the pressure wave produced by the collapse of a bubble in a liquid, J. Fluid Mech. 97 (3) (1980) 481–512.

[3.2] R.I. Nigumatulin, N.S. Khabeev, F.B. Nagiev, Dynamics, heat and mass transfer of vapor gas bubbles in liquid, Int. J. Heat Mass Transfer 24 (6) (1981) 1033–1044.

[3.3] V. Kamath, A. Prosperetti, Numerical integration methods in gas bubble dynamics, J. Acoust. Soc. Am. 85 (1989) 1538–1548.

[3.4] Y. Matsumoto, F. Takemura, Influence of internal phenomena on gas bubble motion (e□ects of thermal di□usion phase change on the gas–liquid interface and mass di□usion between vapor and noncondensable gas in the collapsing phase), JSME Int. J. B-37 (2) (1994) 288–296.

[3.5] F. Takemura, Y. Matsumoto, Influence of internal phenomena on gas bubble motion (e□ects of transport phenomena and mist
formation inside bubble in the expanding phase), JSME Int. J. B-37 (4) (1994) 736–745.

3.[6] K.A. Mørch, Cavitation and inhomogeneities, in: On the Collapse of Cavity Cluster in Flow Cavitation, Springer-Verlag, 1980, pp. 95–100.

[3.7] R. Omta, Oscillation of a cloud of bubbles of small and not so small amplitude, J. Acoust. Soc. Am. 82 (1987) 1018–1033.

[3.8] G.L. Chahine, R. Duraiswami, Bubble nuclei measurement via an inverse acoustic scattering technique, ASME J. Fluids Eng. 114 (1992) 680–686.

[3.9] G.E. Reisman, Y.C. Wang, C.E. Brennen, Observations of shock waves in cloud cavitation, J. Fluids Mech. 335 (1998) 255–283.

[3.10] Y. Matsumoto, M. Shimada, Dynamics of cavitation bubble
cloud, ASME FEDSM97-3267, 1997.

[3.11] M. Shimada, T. Kobayashi, Y. Matsumoto, Dynamics of cloud: cavitation and cavitation erosion, ASME FEDSM99-6775, 1999.

[3.12] Y. Matsumoto, J. S. Allen, S. Yoshizawa, T. Ikeda, Y. Kaneko, Medical ultrasound with microbubbles, Experimental Thermal and Fluid Science, 29, pp.255-265, 2005.

[3.13] T. Ikeda, S. Yoshizawa, M. Tosaki, J. S. Allen, S. Takagi, N. Ohta, T. Kitamura, Y. Matsumoto, Cloud cavitation control for lithotripsy using high intensity focused ultrasound, Ultrasound in Medicine and Biology, in press.

[3.14] G.R. ter Haar, Acoustic surgery, Phys. Today 54 (16) (2002) 29–34.

[3.15] L.A. Crum, Acoustic hemostasis, in: Proc. 15th ISNA, 1999, pp. 13–22.

[3.16] S. Umemura, K. Kawabata, K. Sasaki, In vitro and in vivo
enhancement of sonodynamically active cavitation by secondharmonic superimposition, J. Acoust. Soc. Am. 101 (1997) 569–577.

[3.17] R.G. Holt, R.A. Roy, et al., Bubbles and HIFU: the Good, the bad, and the ugly, in; Proc. 2nd ISTU, 2002, pp. 120–131.

[3.18] S. Umemura, K. Kawabata, K. Hashiba, Enhancement of ultrasound absorption by microbubbles for therapeutic application, in:Ultrasonic Symposium, 2001.

[3.19] N.T. Sanghvi, F.J. Fry, et al., High intensity focused ultrasound treatment of prostate Tissue in the presence of us contrast agent, J. Ultrason. Med 14 (1995) S17.

[3.20] Y. Kaneko, T. Higaki, T. Maruyama, Y. Matsumoto, The e□ect of microbubbles as a heat transducer, in: Proc. 3rd ISTU, Lyon, France, 2003, pp. 55–60.

[3.21] Y. Kaneko, S. Watanabe, S. Takagi, Y. Matsumoto, Temperature distribution in the medium containing contrast

agent microbubbles in HIFU field, in: Proc. 5th ISTU, Boston, USA, 2005, pp. 353-357.
[3.22] P.A. Evan et al., Kidney damage and renal functional changes are minimized by waveform control that suppresses cavitation in shock wave lithotripsy, J. Urol. 168 (2002) 1556–1562.
[3.23] H. Kato, A. Konno, M. Maeda, H. Yamaguchi, Possibility of quantitative prediction of cavitation erosion without model test, Trans. ASME J. Fluids Eng. 118 (1996) 582–588.
[3.24] L.A. Crum, Cavitation microjets as a contributory mechanism for renal calculi disintegration in ESWL, J. Urol. 140 (1988) 1587–1590.
[3.25] S. Zhu, P. Zhong, et al., The role of stress waves and cavitation in stone comminution in shock wave lithotripsy, Ultrasound Med. Biol. 28 (5) (2002) 661–671.
[3.26] X. Xi, P. Zhong, Improvement of stone fragmentation during shock-wave lithotripsy using a combined EH/PEAA shock-wave generator—in vivo experiments, Ultrasound Med. Biol. 26 (3) (2000) 457–467.
[3.27] D.L. Sokolov, M.R. Bailey, L.A. Crum, Use of a dual-pulse lithotripter to generate a localized and intensified cavitation field, J. Acoust. Soc. Am. 110 (2001) 1685–1695.
[3.28] Y. Matsumoto, S. Yoshizawa, T. Ikeda, Dynamics of bubble cloud in focused ultrasound, in: Proc. 2nd ISTU, ISBN 0-7354-0125-X, Seattle, America, 2002, pp. 290–299.
[3.29] T. Ikeda, M. Tosaki, Y. Matsumoto, M. Ohta, T. Kitamura, Renal stone comminution utilizing cloud cavitation erosion, in:
Proc. 3rd ISTU, Lyon, France, 2003, pp. 49–54.
[3.30] Y. Matsumoto, S. Yoshizawa, Behavior of bubble cluster in ultrasound field, Int. J. Numer. Methods Fluids, 47, pp.591-601, 2005.

Invited Lecture

4. GUIDE VANE SURFACE DAMAGE TO THREE GORGE TURBINES A CHALLENGE TO MODERN TURBINE TECHNOLOGIES

A more detailed version presented at the 1st Int. Conf. on Hydropower Technology & Key Equipment 2006 (Beijing) is attached in the end.

Professor S.C. Li
University of Warwick, Coventry, UK
S.Li@warwick.ac.uk

ABSTRACT

The Francis turbines (710 MW) of Three Gorge Project are the world largest and even larger ones (1000MW) are to be developed for schemes on the upstream of the Yangtze river. The 14 units installed in the left-powerhouse have been all commissioned successfully during the period from June 2003 to September 2005, functioning as expected. Despite the success of commissioning and the normality of functioning, all these turbines supplied by world leading manufacturers have developed a pattern of damage mainly on the guide-vanes. This type of damage has never been reported before. Is it an isolated issue or a fundamental phenomenon/challenge present to huge turbines? A brief description of the damage together with suggestions of research is presented, in order to facilitate further investigations in response to this challenge.

4.1 INTRODUCTION

The turbines developed for Three Gorge Project are the world largest Francis turbines in terms of their power (710 MW) and geometric dimensions (9800 mm of runner diameter). The 14 units installed in the left-powerhouse have been all commissioned successfully during the period from June 2003 to September 2005, generating electricity normally.

The damage was firstly found on the Number 11 turbine ('11F' will be used in the article, following the abbreviation employed at the Three Gorge Power Station) incidentally on 14th October 2005 (operated for 10,245.78 hours) when examining/repairing the damaged guide plate [1]. Later on similar damages were found on 10F on 27th December 2005 (11924.55 hours), on 9F on 11th December 2005 (2328.41 hours) and other units (e.g. 5F and 6F etc). The 14 machines in the left-powerhouse are supplied by two consortiums (Alstom + HEC, GE + Voith Siemens + DFEM) [4.1]

The significance of the Three Gorge Project itself is obvious in terms of technology development, economic-social-environmental effects. Further 12 similar turbines, in the right-powerhouse are being installed, and 6 additional similar machines in the underground- powerhouse will be purchased soon. Other hydro projects employing similar scale turbines are being developed by the China Yangtze Three Gorge Project Development Cooperation (CTGPC). For example, 18 turbines of 770 MW each for Xiluodu Project and 8 turbines of 750 MW each for Xiangjiaba are to be purchased late this year; 18 turbines of 825 MW each for Baihetan project and 10 units of 700 MW each for Wudongde project are at the feasibility study stage, total about 90 turbines. It is also under consideration to develop 1,000 MW turbine-generator units for hydro schemes. Under such a strategy for hydropower development, these damages, although their impact on the machine

[1] A device developed and employed on turbines for the first time. It will be discussed later.

operation is insignificant[2], does catch the great attention from the top management team of CTGPC, and needs to be thoroughly investigated.

Questions immediately arise: is this a new phenomenon happened in extremely large turbines? Are there any new technologies need to be developed for even larger turbines? A special meeting was thus held at the Three Gorge site from 12 to 14 March 2006, attended by research engineers, university academics and manufacturer representatives. A few days later (19th March 2006), the author inspected the damages on 11F unit, in particular the damage on No 4 guide vane. It is realized that in order to find the nature of the damage, remedy approach and guidelines for future design & manufacture, a multidisciplinary research is essential. The outcome would benefit not only the power industry but also scientific knowledge in general. The purpose of presenting this article to the FORUM 2006 is for promoting research in this direction.

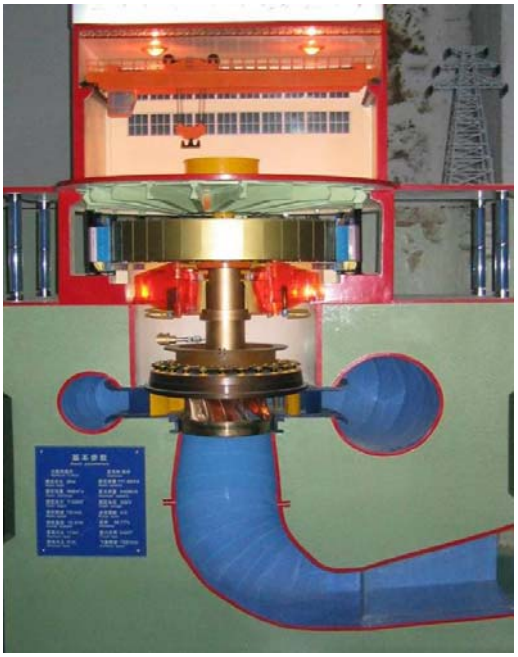

Figure 4.1: Cross-section of Three Gorge Plant model
(Courtesy of Harbin Electric Works)

4.2 BASIC INFORMATION

The power plant is shown by the model in Figure 4.1 and the specifications of the 11F turbine are as follows:

- Rated power 710 MW
- Max efficiency guaranteed, 96.26%
- Rated head 80.6 m
- Min head 61.0 m
- Max head 113.0 m
- Rated speed 75 rpm
- Run away speed <150 rpm

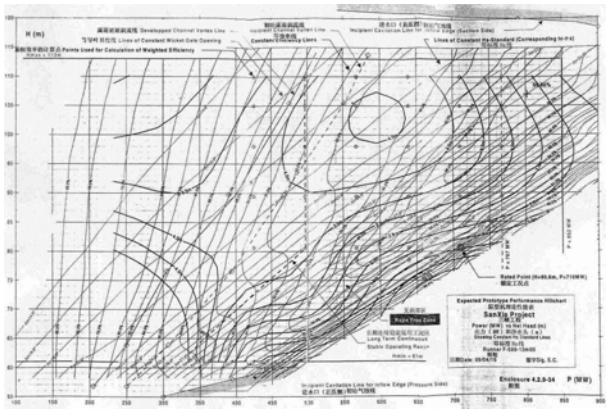

Figure 4.2: Expected prototype performance hill-chart for 11F by the supplier

The performance curve is shown by Figure 4.2. The 11F unit has been operating under low head conditions around and below 70 m.

[2] They do not require an immediate rectification/repairing at this stage because the damage does not affect the safety and effectiveness of operation.

4.3 DAMAGE OBSERVED

4.3.1 NO. 4 GUIDE VANE (11F)

The damage observed on the Number 4 guide vane of 11F turbine is representative for this particular pattern of damage. The guide vane is a positively curved hydrofoil as shown in Figure 4.3. The turbine has total 24 guide vanes and 24 stay vanes, referring to Figure 4.3.

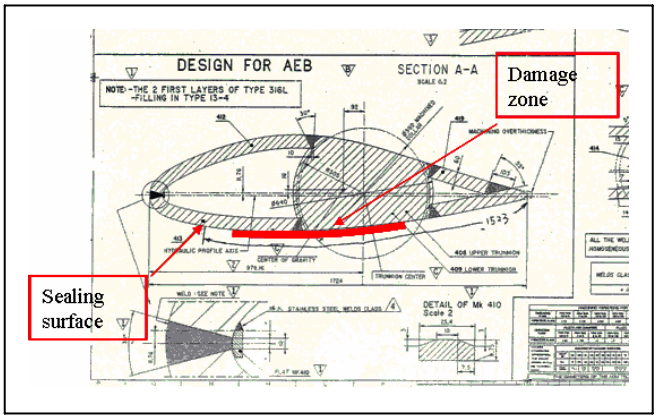

Figure 4.3: No 4 guide vane

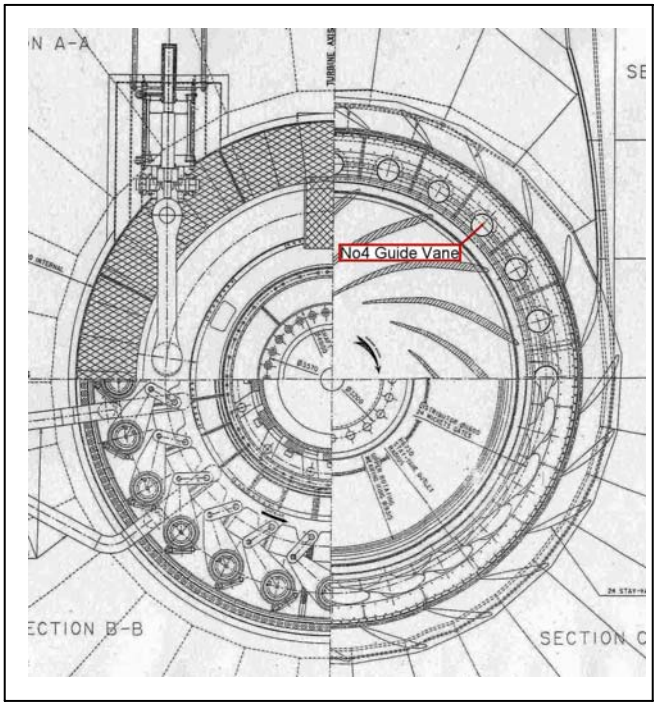

Figure 4.4: Plan view of 11F turbine

4.3.2 FEATURES

The damages occur only on the foil's lower surface [3] as horizontal strips, starting in the favorable pressure gradient (FPG) zone extending into adverse pressure gradient (APG) zone as shown by Figure 4.5 and Figure 4.6.

Figure 4.5: Damages on the lower surface on all guide vanes showing nearly the same pattern

[3] Here, the lower surface refers to the pressure side of a foil if the angle of attack is positive as conventionally defined in aerofoil aerodynamics.

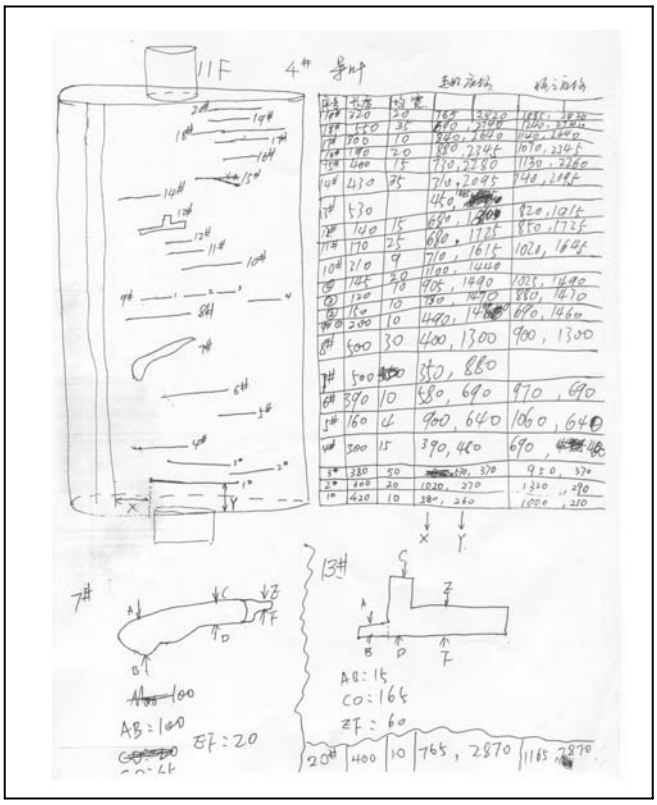

Figure 4.6: Sketch of damage on No4 guide vans (11F)

The depth of most damaged area is much less than 1 mm fully covered by corroded rough surface as shown by Figure 4.7.

Figure 4.7: Damaged surface

Heated tail on damaged surface is observed (red-circled in Figure 4.7), which is another common feature. Figure 4.8 shows heated area at joints. However, it puzzles that the circled one (in Figure 4.8) is not similar to others that appear approximately at the main flow direction.

Figure 4.8: Heated sign on the top surface between guide vanes

This heated feature is also observed on other machines, e.g. photos from 9F are shown by Figure 4.9 and Figure 4.10. These are approximately in the direction of flow there.

Figure 4.9: Heated tails observed on the top ring (9F)

Figure 4.10: Heated tail on the guide vane (9F)

Another feature is the wedged head, which almost always presents[4]. Typical one is shown in Figure 4.11.

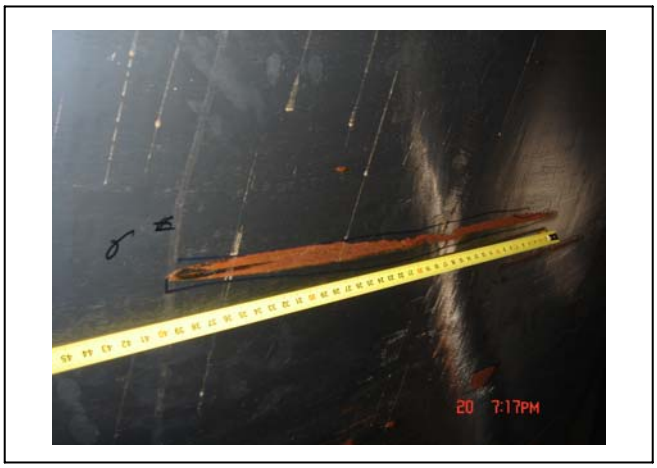

Figure 4.11: A damaged strip showing wedged head

These damaged strips are distributed in span-wise, showing regularities, referring to Figure 4.5.

4.4 INVESTIGATIONS REQUIRED AND RELEVENT KNOWLEDGE

Such damages on the guide vane have not been reported before. It shows clear sign of multi-disciplinary nature. Based on our current knowledge, the following aspects are considered as the main research directions.

4.4.1 CAUSE OF DAMAGE

It is suggested that, among all possible factors, cavitation damage needs to be considered firstly although the observed does not comply with conventional cavitation damages often observed on Francis turbines. The following facts strongly suggest the possible cause of cavitation.

Heated tail of damaged area

The observed heated (blue and other) colour zone at the tails of damages suggests that this zone has encountered a temperature around $250^0 C - 600^0 C$ (called as 'bluing' in heat-treatment[5]). As far as we know, the hydrodynamic mechanism involved in Francis turbines that would provide/generate temperature above this range is cavitation. The experimentally proven temperature that a collapsing single bubble could generate is about $6000^0 C - 7000^0 C$ [6]. One may argue that the damage compared with those we often observed in Francis turbines, in particular those made of low-alloy steels before 1980's, are different. They all show typical sponge-like deep erosion, such as shown by Figure 4.12.

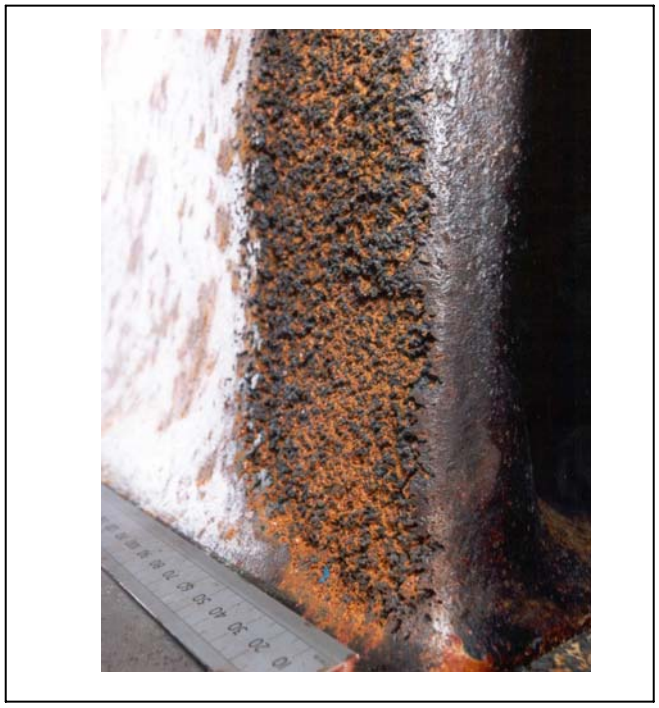

Figure 4.12: Typical sponge-like erosion pattern caused by a leading-edge cavitation attack (4000 hour operation) [4.2]

Firstly, materials with better cavitation resistance are used such as the martensitic stainless steel (containing 13% Cr and 4% Ni or 17% Cr and 7% Ni) to replace the low-Mn steel for fabricating machines. The material used for 11F is X3CrNiMo13-4 (EN-1088), close/equivalent to *CA6MN* (12.9% Cr, 4% Ni and 0.04% C), a commonly used martensitic stainless for turbine fabrications [4.4]. Secondly, the striking force, i.e.

[4] The heads of No 1 & 18 has been sanded off by the representative of manufacturer.

[5] A simple heat-treatment method that coats steels with a thin, even film of coloured oxide from bluish-black to purple brown shade, obtained by exposure to an atmosphere of dry steam or air, at certain temperature subject to the material as well as the colour. A typical case of coating sheets with a thin, even film of bluish-black oxide is obtained by exposure to an atmosphere of dry steam or air, at a temperature of about $1000^0 F$ ($538^0 C$) done during box-annealing [**Error! Reference source not found.**].

[6] Comparison with black body's spectra gives the temperature values.

cavitation attack, is relatively weak owing to the high overall pressure in the guide vane passage and the possible cavitating mechanism, which will be addresses later. The existence of this heated zone itself may evidence a relative weak cavitation attack on a relatively high cavitation-resistance material. We may think in this way that heating effect always presents during cavitation attack, but if damage rate is high, the heated portion is removed immediately by bubble strikes. Therefore, we cannot see the heated zone aft wards. The very low erosion rate (much less than 1 mm over 10,000 hours) could support this hypothesis reasonably.

Corrosion appearance on the damaged area

The existence of corrosion on all damaged area combined with the fact of very shallow damage depth (actually touch feeling only) readily tempts one to think that corrosion is the underlying cause responsible for the damage observed as some comments made at the meetings. However, it might be more appropriate to assume the corrosion is a consequence of cavitation damage. The following arguments may provide clues for clearing the cloud shading on the nature of the damage.

The material is a martensitic S S as suggested by its brand, which is roughly equivalent [7] to CA6MNindicated by 'W' in the Schaellfler diagram, referring to Figure 4.13.

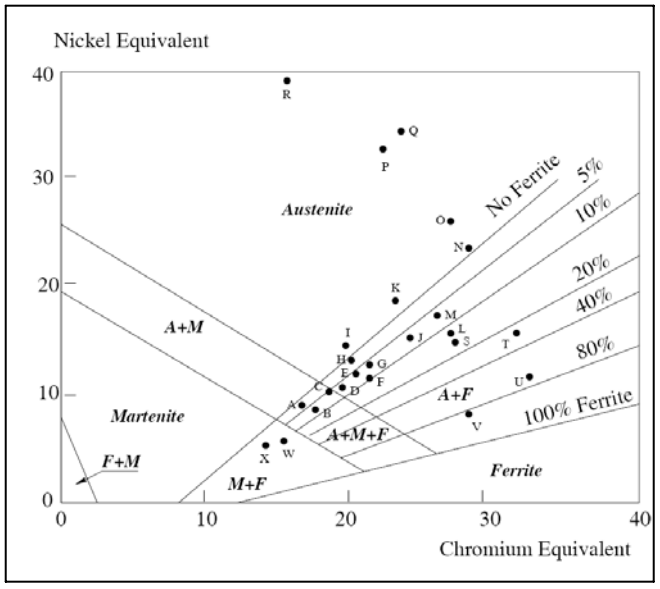

Figure 4.13: Schaeffler diagram [4.3]

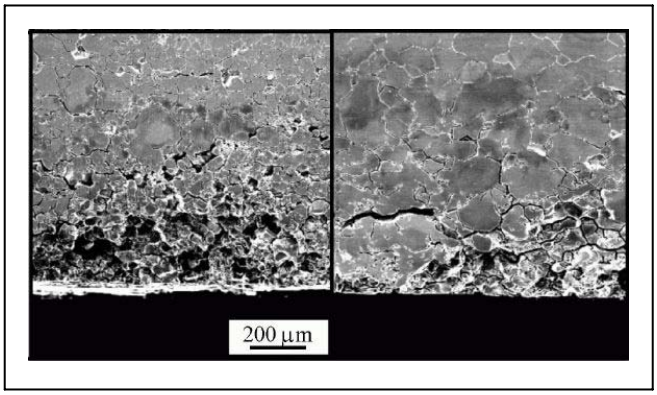

Figure 4.14: Grain de-cohesion due to inter-granular corrosion [4.6]

For Austenite S S, *sensitization* is a well-known phenomenon of heat effect that causes inter-granular corrosions and is a wide spread problem. When an austenitic stainless steel is exposed to a temperature range between $620^0\ C$ to $676^0\ C$, subject to exposure-time as well as its own composition, the carbon will diffuse towards the grain boundaries where the high concentration of carbon ties up the chromium by forming chromium carbides $M_{23}C_6$ at grain boundaries, which leaves a zone of chromium depletion in the immediate area around the grain boundary making this area less corrosion resistant than the bulk material and resulting in inter-granular corrosion [8]. Such typical corrosion (on 304) is shown in Figure 4.14.

The mechanism of sensitisation is conceptually shown by Figure 4.15.

[7] Accurate and detail analysis of chemical composition and metallurgical structures needs to be done.

[8] The *stainless* character occurs when the concentration of chromium exceeds about 12 wt%.

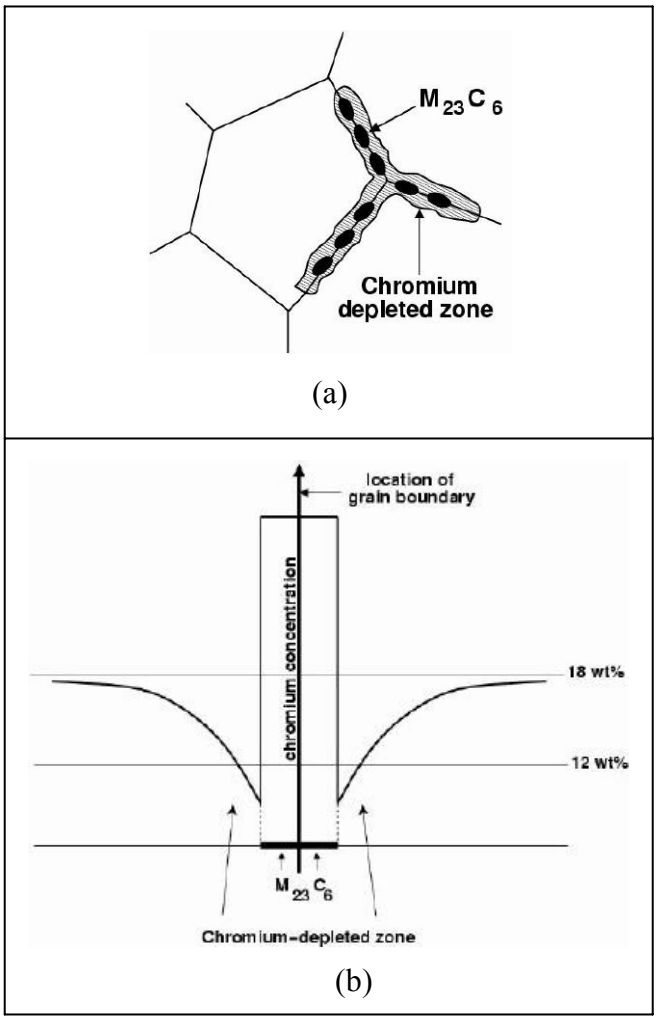

Figure 4.15: Conceptual sketch of sensitisation. (a) Chromium depleted zone susceptible to inter-granular corrosion (b) Chromium distribution across grain boundary [4.5].

Most publications concerning inter-granular corrosion refer to austenitic steels. Study of inter-granular corrosion in martensitic stainless steels is not in current technical literature. Does that mean sensitization is irrelevant or insignificant to martensitic stainless steels? Actually, Inter-granular corrosion is also a potential problem to Martensitic S S because it is a Fe-Cr-C system and always used in tempered condition [9], in which carbides are precipitated. Recent investigations [e.g. **Error! Reference source not found.**], show a trend that the maximum susceptibility to inter-granular corrosion was observed in the condition tempered at $500^0 C$ to $550^0 C$, and a sensitized structure was detected. For lower tempering temperatures, steel was less sensitized, or not at all, and for higher tempering temperatures, steel was less sensitized. A typical case (UNS S41000) is shown in Figure 4.16 ($550^0 C$), and the characteristic value variations with temperature (for two hours) are shown in Figure 4.17. A zone of high sensitization-susceptibility is indicated clearly for temperature ranging from $500^0 C$ to $600^0 C$.

[9] Martensitic S S is often used for fabrication. Both strength and toughness are requested which is achieved through temper treatment. It is known: (1) at 350°C, higher strength and moderate toughness (2) at 650°C, moderate strength and high toughness (3) avoid 500°C, temper embrittlement (i.e. sensitisation) and minimum toughness.

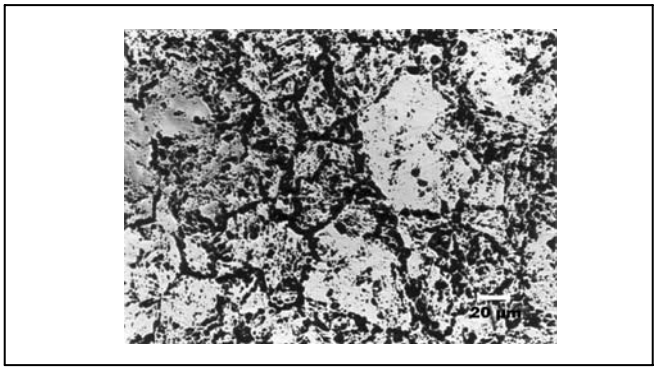

Figure 4.16: Optical micrographs of UNS S41000 steel specimens after oxalic acid etch test: tempered at $550^0 C$ [4.7].

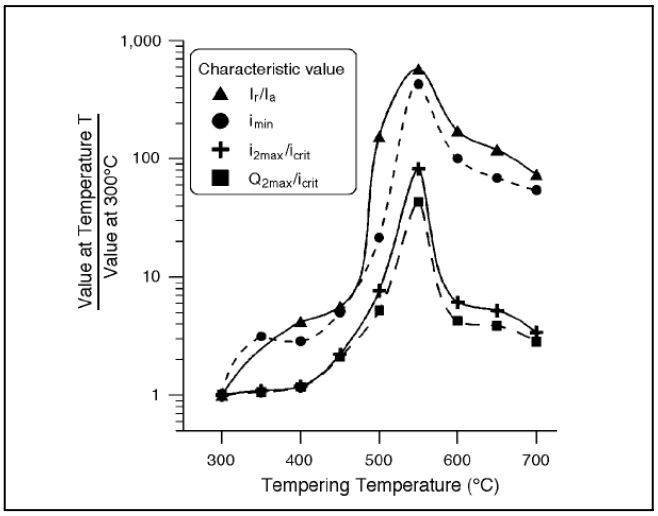

Figure 4.17: Comparison among electrochemical tests to discriminate degrees of sensitisation for different tempering temperatures. Characteristic values are i_r / i_a for the DL-EPR, $i_{\min}$ for the potentiostatic test, and $i_{2\max} / i_{crit}$ and $Q_{2\max} / i_{crit}$ for the potentiokinetic polarization. To make different tests comparable, the ratio was plotted between the characteristic value for the material tempered at different temperatures and the same for the material tempered at $300^0 C$ [4.7].

Now, recall the heated sign left on the tail of damaged area, the blue colour (plus other spectra of colors) strongly suggest a similar heat treatment including the temperature range of $500^0 C$ to $600^0 C$ encountered, which is an ideal environment for sensitization, leading to inter-granular corrosion.

4.4.2 CAVITATION INCEPTION

The damage pattern does not suggest a large structure of cavitating-flow that directly strikes and causes the damage as shown by Figure 4.12, whereas, the wedged head of damage strips gives us a hint: is there any links with the turbulent spot from boundary layer transition to turbulence which is also featured by wedge head?

Inception of cavitation on hydrofoil is closely related with and strongly influenced by boundary layer transition. The main points can be summarized as follows [4.12].

For cavitation in the boundary shear layer, the statistical properties of bubbles are dominated by the pressure fluctuation field in terms of their intensity and duration. Therefore, the distribution of the turbulence level, which varies across the boundary layer, alters the statistical characteristics of the micro-bubbles' inception performance across the boundary layer. This phenomenon was firstly demonstrated by Daily & Johnson [4.8]. This relation indicates that the lowest mean pressure across the boundary layer is at the location where the turbulence level is highest since (referring to Figure 4.18).

$$\bar{p} + \rho\overline{v'^2} = p_1(x) \qquad (1)$$

where $p_1(x)$: pressure in the free flow region beyond the boundary layer where $\overline{v'^2}$ is negligible

$\bar{p}$: mean pressure

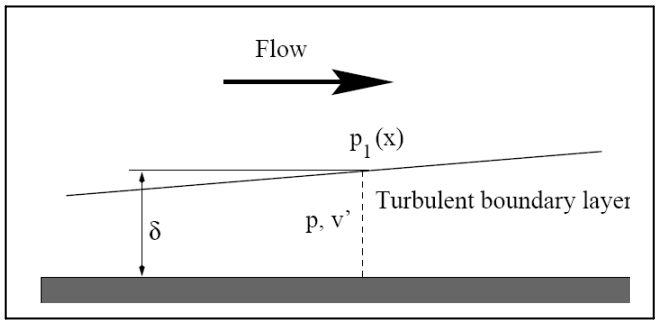

Figure 4.18: Conceptual sketch of (turbulent) boundary layer

It is obvious that bubbles at this particular location have the highest probability to cavitate owing to the minimum value of mean pressure and the maximum value of instant pressure drop.

The influences of magnitude and time scale of turbulence on cavitation inception were also demonstrated by many other studies on inception scale effect. For example as early as 1981, Arakari & Acosta [4.9] already emphasize the importance of time scale by postulating that the turbulent fluctuations may actually stall the local flow near the wall, leading to a brief period of separation or a turbulent burst with reverse flow. Then the nuclei within these regions may be exposed to a low pressure longer than would otherwise be the case, thereby promoting the growth of micro-bubbles. This is supported by their experiment that the frequency of the most unstable Tollmien-Schlichting wave in the laminar boundary layer just prior to transition is about 5 kHz equal to a reference time period of 0.2 msec for growth, which is about the same order as the bubble life-time (0.1 msec) observed. The early work by Huang [4.10] also found that the inception is correlated with the spatial amplification ratio A through the mechanism of laminar to turbulent transition or laminar separation. For the tunnel with low level of free-stream turbulence, the inception is well correlated with the computed amplification ratio value of $A = e^{11}$; and, for higher levels of free-stream turbulence, it takes place in a region where the value of A is less than e^{11}, for say e^9 or even e^7.

As early as 1979, attempt by using the Kolmogorov theory for homogeneous and isotropic turbulence to relate the properties of the temporal pressure field to cavitation inception for both free turbulent shear flow and fully developed boundary

layer flow has been made. For fully developed boundary layer flow, Arndt & George [4.13] suggested that if

$$\left(\frac{u_*^2}{\nu}\right)T_B < 1 \quad \text{for smooth wall;}$$
$$\left(\frac{u_*^2}{h}\right)T_B < 1 \quad \text{for rough wall,} \qquad (2)$$

the nuclei in the flow will have enough time to respond to the entire spectrum. Otherwise only a fraction below the frequency of T_B is sensed by the micro-bubbles[10].

As early as 1979, Gates & Acosta [4.11] have already shown that free-stream turbulence is an important factor for inception scaling; and that the mechanism through which this factor influences inception is the structural alteration of the boundary layer in terms of its separation and/or transition[11]. This is crucial for extremely large turbines, the difference of Reynolds number (based on main flow parameter, reflecting free stream status) between model and prototype is in the order of 10^2, which represents a significant difference on turbulence level, consequently the influence on cavitation inception.

All these make us to think: if for this case (particular large turbines) the scale effect makes it happen[12] that the *turbulent spots* just generated at a right position where flow has a highest susceptivity to cavitation inception and thus trigger the *cavitation-inception* there, In other words, both *turbulent spots* and *inception points* concise for prototype. This could be significant to scientific knowledge and engineering practices.

4.4.3 FREESTREAM TURBULENCE & B.L. TRANSITION

Despite of studies over decades, the origins of turbulent flow and transition from laminar to turbulent flow still remains an unsolved challenge for fluid mechanics. Currently, even for flows over a flat plate, no mathematical model can precisely predict the transition Reynolds number because of variety of influences, such as free-stream turbulence, surface roughness, which are still not fully understood yet. Currently, owing to the availability of linear stability methods and the knowledge of breakdown mechanism being initial condition dependent, studies are aiming at understanding the source of initial disturbances rather than the details of the later stages of transition [4.14]. For turbines, owing to its complexities in geometry and off-design operation, much less is known [4.15]. For hydro turbines, about the interplay of B L transition with cavitation inception, little study has been done. Therefore, understanding the origin of the cavitation on the guide vane, if B L transition does play a significant role on this, is a great challenge to us. The outcome of this study will advance our knowledge about the interaction between cavitation inception and B L transition.

Current knowledge about the process of transition for boundary layers in external flows can be conceptually depicted by a roadmap, referring to Figure 4.19. The transition may develop by following one of the scenarios to turbulence [4.16]. The initial amplitude increases from left to right and disturbances may be too small to measure initially. They can be observed only after the onset of instability. Different instabilities may occur alone or in concert, subject to Reynolds number, wall curvature, sweep, roughness, and initial conditions etc.

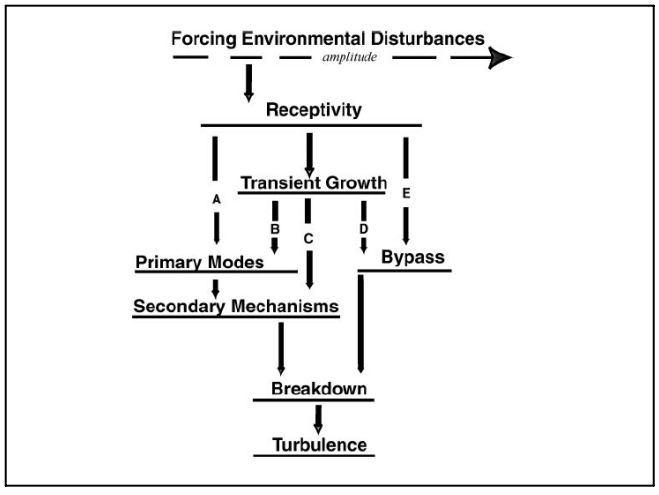

Figure4.19: Roadmap from receptivity to transition [4.14].

[10] For turbulent boundary layer flow, the highest frequency in the flow is $\left(u_*^2/\nu\right)$ for smooth wall and $\left(u_*^2/h\right)$ for rough wall. Thus if the bubble frequency T_B is higher than the highest frequency, the entire spectrum may contribute to bubble growth.

11 See, e.g. § 2.4 'Cavitation Nucleation and Inception' in *Cavitation of Hydraulic Machinery*, ICP, London.

[12] On model tests, no cavitation observed within the allowable operating zone.

For 3D B L flows over (hydro) foil, cross-flow instability may dominate the breakdown while T-S waves act as generators of fundamental low-frequency secondary modes, but are neither important for their growth nor for breakdown [4.17].

For the problem on our hands, the damage pattern on guide vane gives us a clue that it is virtually a 2D flow. The resulting perturbed flows are span-wise-dependent but essentially unidirectional, i.e. the transverse velocity components are much smaller than the stream-wise component. The instability of such transversely sheared flows appears to be related to various aspects of the transition process, such as secondary instabilities and by-pass transition. Many factors [4.19] can cause three-dimensional steady/unsteady distortions in the form of stream-wise or longitudinal vortices. These include small steady or unsteady perturbations superimposed on the oncoming flow, imperfections at the leading edge[13], cross-flow instability, and Görtler vortices induced by surface curvature, as well as certain excitation devices. Distortion of this kind also arises due to the nonlinear interaction between pairs of Tollmien-Schlichting waves.

For the turbines in the left-plant, a guide plate is located in the spiral case prior the entrance of stay-vane passage shown in Figure 4.20. Obvious, the designer intended to reduce the size of spiral case without sacrifice of cross-section area. However, the premature damage (a piece torn off) of the guide plate and subsequent severe pressure-fluctuation and machine-vibration gave us a clear clue: this device might have caused unusual free-stream disturbances in the oncoming flow (i.e. the wake flow of stay-vane) to the guide vane. Will these disturbances cause particular distortion in the boundary layer of guide vane? Researchers have demonstrated a type of span-wise distortion (modulation) induced by various free-stream disturbances. For example, it has been shown in 1936 that small low-frequency three-dimensional perturbations in the free stream can produce significant distortion within the boundary layer, leading to alternating span-wise thickening and thinning [4.20]. Steady disturbances (e.g. artificial roughness, vortices etc) can also cause a similar type of span-wise modulation [e.g. [4.21]]. And these distortions are all in the form of elongated streaks now named as *Klebanoff* mode [4.22, 4.23 and 4.24]. This phenomenon is well summarized by Kendall [4.22].

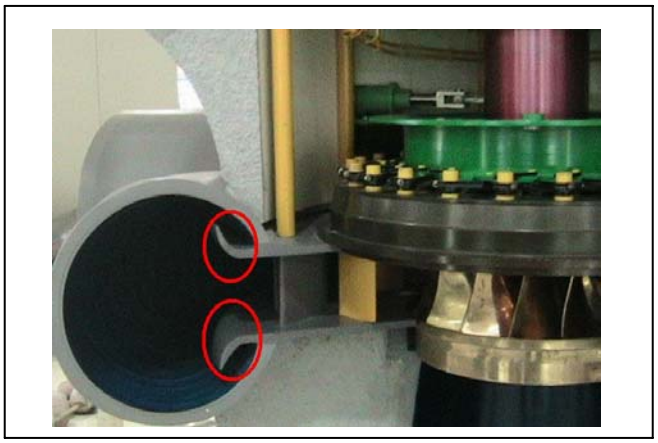

Figure 4.20: Guide-plate (circled) shown on the model of turbine

'Klebanoff recorded the fluctuation development in a flat plate layer at Re_x up to 2.1×10^6 for stream turbulence levels up to 0.3 percent. The turbulence was generated by means of various grids placed in the settling chamber of the tunnel. He showed that low frequency (in comparison with the most amplified TS-waves) fluctuations commenced growth at the plate leading edge and attained an amplitude of five percent at a station well ahead of the onset of transition, with the amplitude along the plate length varying in direct proportion to the boundary layer thickness.'

'The broad band signal amplitude distribution through the layer resembled that which would result from a thicken/thinning oscillation of the layer, and Klebanoff referred to the low frequency motion as the breathing mode of the layer. He found by correlation methods that the broadband disturbances were quite narrow laterally, being no more than a few boundary layer thicknesses wide, although the scale depended upon that of the free-stream turbulence and not upon the layer thickness.'

Currently we have very limited understanding about the instability of Klabenoff mode and its role in the transition owing to the random nature of both the free-stream disturbances and the Klebanoff

[13] And the sealing surface in our case.

motion. Most studies so far investigate steady distortions, induced in a controlled manner through the receptivity at leading edge only [14]. The maximum growth of this K-mode distortion is a function of Reynolds number and wave number, e.g. as demonstrated by Anderson et al [4.25] referring to Figure 4.21. Here, $\bar{\beta}$ is span-wise wave number,

$$\bar{\beta} = \beta^* \nu / U_\infty = \beta / \sqrt{\mathrm{Re}} \qquad (3)$$

with β^* is the dimensional span-wise wave number; β is the non-dimensional span-wise wave number valued as $\beta = 0.45$ for maximum transient growth. They assumed a receptivity at the leading edge and calculated the turbulence gain G of disturbance energy,

$$G(x_f) = \max_{\|\mathbf{u}_{in}\|=\|\mathbf{b}\,\mathbf{q}\|=1} \left\|\mathbf{u}_{out}(x_f)\right\|^2 \qquad (4)$$

based on the periodic initial disturbances which leading to solutions of the form

$$(u,v,w,p) = (u(x,y)\cos\beta z,\, v(x,y)\cos\beta z,\; w(x,y)\cos\beta z,\; p(x,y)\cos\beta z) \qquad (5)$$

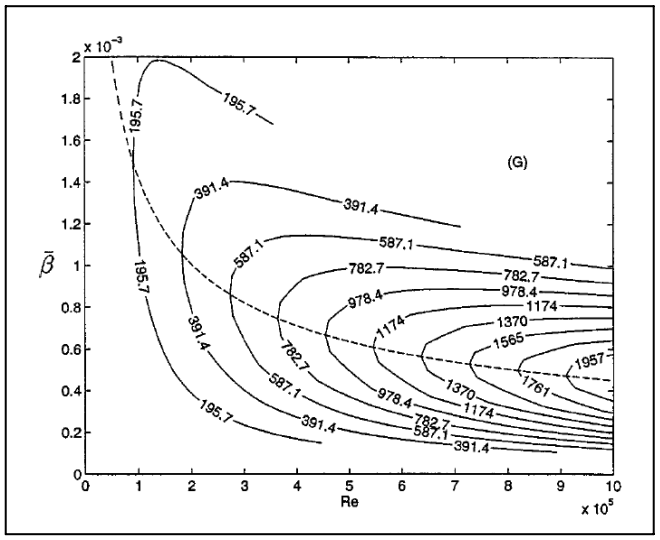

Figure 4.21: Contour plot of maximum transient growth vs. $\bar{\beta}$ and Reynolds number. The dashed line describes $\bar{\beta}$ for which the maximum transient growth occurs given a specific Reynolds number. Here $x_0 = 0$ [4.25].

[14] In reality, there is a continuous receptivity process along the stream-wise extent of the boundary layer, as in flow around the guide-vane.

The mechanism of the downstream response to upstream disturbance is visualized by Figure 4.22. The calculated initial disturbance at $x_0 = 0$ is outside the boundary layer, while its downstream response is inside the boundary layer. Thus, this numerical simulation demonstrate well the receptivity at the leading edge: the disturbances at the leading edge that cause the largest growth of stream-wise streaks inside the boundary layer are vortices aligned in the stream-wise direction outside the boundary layer.

It is suggested that the breakdown into turbulent spots is related to local instabilities of the strong shear layers associated with these streaks. Flow structures typical of the spot precursors are presented and these show important similarities with the flow structures observed in previous studies on the secondary instability and breakdown of steady symmetric streaks [4.26].

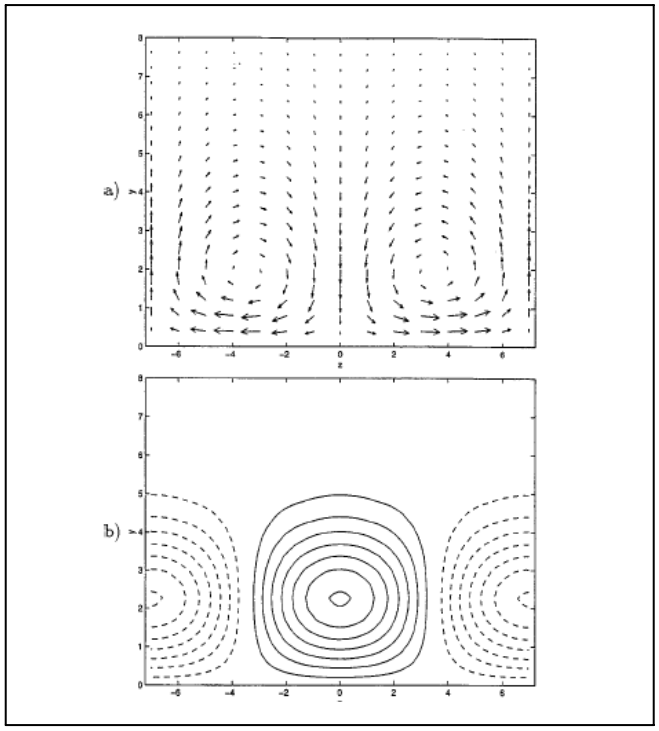

Figure 4.22: (a) Velocity vectors in the z – y plane of the optimal disturbance at $x = x_0$. Here $x_0 = 0$ and $\beta = 0.45$. The u component is zero. (b) Contours of constant stream-wise velocity representing the downstream response at $x = x_f = 1$ corresponding to the optimal disturbance shown in Figure 4.21. The v and w components are zero. Here, the solid lines represent positive values and the dashed lines represent negative values [4.25].

Free-stream turbulence initiates three distinct motions within the boundary layer, as summarised by Saric et al [4.14]. The first motion is a sustained, streaky ($z \approx 2\delta$), high amplitude ($|u'| \approx 5-10\%U_\infty$) motion, which is probably due to stretching of the ingested free-stream vorticity and the growth of transient modes, i.e. the Klebanoff mode. The second is an outer-layer oscillation at T-S frequencies that grows weakly in the stream direction. The third is the usual T-S mode, which exhibits higher growth rates. Kendall found the following:

(a) The T-S waves are wave-packet-like and are of lower amplitude than the other two modes. Thus, an internally generated wave packet behaves differently than an externally generated wave packet.

(b) The Klebanoff modes were unchanged by leading-edge bluntness and lift, and therefore these modes play no part in the T-S wave development. These modes grow as $x^{1/2}$, having connection to transient growth.

(c)The turbulence is continuously feeding into the generation of the T-S wave along the stream direction. This supposes another, as yet unknown, receptivity mechanism in addition to the leading edge.

(d) Transient (algebraic) growth plays a more important role in the boundary layer response as the free-stream turbulence is increased.

(e) Transient growth plays a particularly strong role in the presence of distributed surface roughness.

Based on above main points known so far, despite the fact that the span-wise wave length (correlating to 2δ , i.e. in the order of 10^1 *mm* for our guide vane) of K-mode streak is an order smaller than the dominant span-wise period of the damage strip-pattern (in the order of 10^2 *mm*), the K-mode involvement (responding to the free-stream turbulence) can not be excluded from further considerations because of following reasons.

Firstly, the guide plate increased free-stream turbulence is a primary concern in the sense of receptivity and the transient growth of K-mode instability, which may bypass the primary OSE mode and lead to early and random breakdown/turbulent spot although the flow in the first half of guide-vane passage is a highly accelerating flow [15] , i.e. with strong favourable pressure gradient, which would have a prolong laminar B L until transition if the level of free-stream turbulence was low.

Secondly, the turbulences in the wake of stay vane is likely to possess span-wise structure (say span-wise distributed stream-wise vortices) comparable with the span-wise variation of observed damage strips, and thus the high receptivity occurs only associated with these structures, causing K-mode transient, bypass transition and breakdown to turbulence in such a pattern of strips. The likeliness of this flow structures [16] is evidenced by the heated pattern in Figure 4.9.

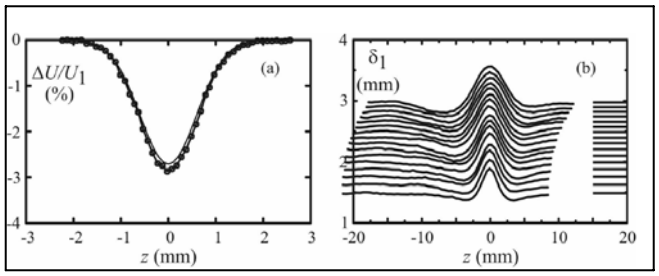

Figure 4.23: (a) Wake profile 63.5 mm upstream of leading edge. Z-relative to wire centreline. (b) Stream-wise growth of span-wise variation of displacement thickness, δ_1 . Z-relative to the peak δ_1 values. Lines in range 15 < z < 20 are Blasius values, i.e. $\delta_1 = 1.7208\left(\nu x / U_1\right)^{1/2}$ [4.27].

Thirdly, the wedged head of damage strips highly resembles the turbulent spots caused by such a streak (K-mode) transient growth and breakdown in a Blasius B L, which leads to a turbulent wedge. As an example, the work by Watmuff [4.27] is worth mentioning here, which demonstrates the evolution of a turbulent wedge from stream-wise streak. In his study, a narrow low-speed streak (i.e. region of elevated thickness) is deliberately introduced into the Blasius boundary layer as a result of the interaction of a laminar wake with the leading edge of the flat plate. The wake is generated

[15] Rough estimation shows that the average velocity increases from 12 m/s at the entrance to 25 m/s at the mid-chord, with a acceleration of $\left.\frac{dV}{dS}\right|_{average} \approx 18\ \mathrm{sec}^{-1}$.

[16] Although the pattern varies azimuthally on the top ring but indicates the likeliness of span-wise variation with similar spacing.

by stretching a fine wire across the full extent of the test section and it is aligned perpendicular to the free-stream and to the leading edge. The wire has a diameter of d=50.8 mm, located 184 mm upstream of the leading edge. Stream-wise development of the span-wise variation of displacement thickness resulting from interaction of the wake (referring to Figure 4.23 (a)) with the leading edge is shown in Figure 4.23 (b) for 16 stream-wise positions, ranging from x=0.3 to 1.8 m. The results clearly demonstrate the narrow region of elevated thickness, i.e. the low-speed streak. The final stages of growth and the ultimate breakdown of the streak are shown in Figure 4.24 (a-c). The breakdown on the centreline and the formation of two regions of highly unsteady flow on either side of the streak are most clearly evident in the contours of the broadband unsteadiness shown in Figure 4.24 (c). It is evident that streak is responsible for introducing a new pair of streaks on either side via some instability mechanism, causing span-wise growth of the wedge since a span-wise succession of new streaks is observed in the early stages of its development.

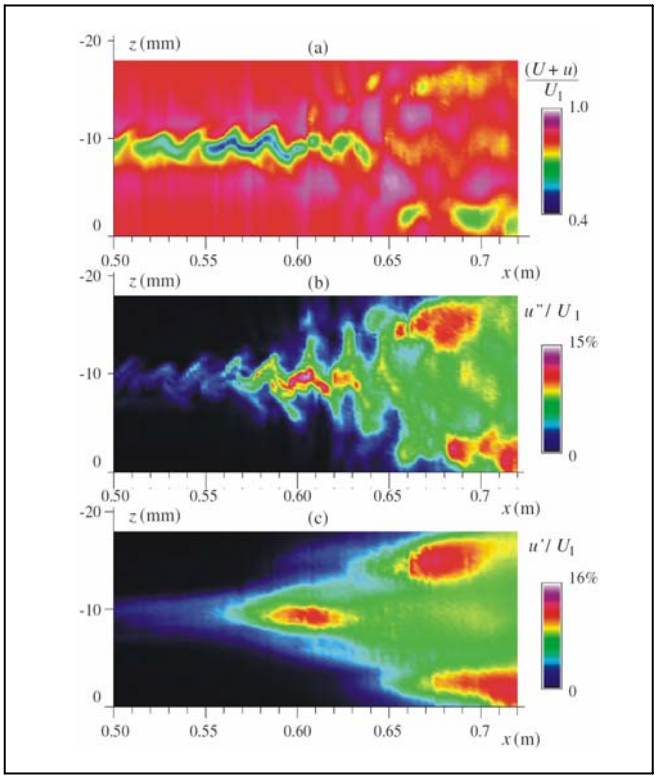

Figure 4.24: True spatial contours in plane, y=2mm (a) $\left(\overline{U}+u_{\phi}\right)/U_1$. (b) u''_{ϕ}/U_1. (c) Broadband unsteadiness, $\overline{u'}/U_1$ [4.27]

Here, $\overline{U}+u_{\phi}$ is the total phase averaged stream-wise velocity; u' is the background (broad band) unsteadiness; and, u'' is the phase averaged unsteadiness.

The wedge-shaped turbulent spot can also be visualized by using both shear sensitive liquid crystal (SSLC) and temperature sensitive liquid crystals (TSLC). The results [4.28] show the dependency of wedge spreading angle on the level of flow acceleration, referring to Table 4.1 and Figure 4.25.

	Zero pressure gradient	Mild pressure gradient	Strong pressure gradient
SSLC	10.3^0	9.4^0	7.8^0
TSLC	5.5^0	4.1^0	2.5^0

Table 4.1: half angles of wedge spreading for zero, mild and strong favourable pressure gradients for SSLC and TSLC [4.28].

Figure 4.25: SSLC results for the turbulent wedge under zero, mild and strong (favourite) pressure gradients respectively [4.28].

Surprisingly, for the case at hands, the features of turbulent-spot above are all supportive to the hypothesis that the cavitation inception points might coincide with the turbulent spots, or in other words, cavitation incepts from these turbulent points. And, a dynamics process follows: once the first damage spot is created at the turbulent spot, it will serves well as a roughness spot create a subsequent damage immediately downstream. This dynamic process progresses stream-wise, resulting in such a horizontal damage strip with a wedged head and heated tail. These span-wise distributed stream-wise damage strips become dominant pattern on the guide vane. This may provide a reasonable route for searching explanation and answer to the problem at hand.

4.6 REMARKS

As this problem has just been discovered, apart from *in situ* inspection, no further study has been conducted yet. The above is only a very preliminary report servicing as guidelines for further investigation and research proposal preparation.

Obviously, this research will be a highly multi-disciplinary investigation. The followings are the main points.

1. Flow analysis of the oncoming flow influenced by the guide plate in terms of flow structure(s) and turbulence level variation is essential. The study should employ the fluid-structure interaction approach because of its comparative thin and plateful geometry without stiffener (constrained by the flow requirement), which readily induces various vibrating modes including extremely low-frequency ones. These low-frequency modes are particular concern because their influences on the growth of boundary layer streaks as mentioned before. The studies may perform numerically first and then followed by experiment study on prototype and model turbines.
2. The information obtained from above flow analysis will facilitate the boundary layer studies [17]. It will look for possible streak formation, receptivity and transition mechanism (including the interaction with T-S waves). It is particular interesting to see if the stream-wise position and the span-wise variation of the breakdown (in particular, the turbulent spots) under such strong influences of the free-stream (flow-structures and turbulence level) agree with the observed pattern of strips. The study may be carried out firstly on flat-plate with added pressure gradients similar to those on the guide vane either numerically or experimentally[18]. As the most interesting issue we want to know is the spatial growth of streaks, a DNS approach in space domain is strongly suggested for numerical study. With the information obtained from flat-plate, we may able to predict the trends about the streak formation, growth, interaction with T-S waves and breakdown. Thus, study on hydrofoil and observation on prototype can be designed and carried more effectively and predictably.
3. The possibility that cavitation inception might occur right at the turbulent spots should be verified through experiments by testing on model foil and monitoring on prototype guide vane. Various approaches can be employed. For example, for prototype, SSLC mentioned before combined with high-speed photography through endoscope is a good choice.
4. The material undergoing this type of cavitation attack should be mimicked through laboratory study in order to understand the heating phenomenon/mechanism associated with this type of damage. It may uncover knowledge yet not known to us. Laboratory study using facilities such as cavitation tunnel or rotating device should be supported by metallurgical and chemical analyses.
5. Developments of novel turbine design/manufacture ideas are encouraged in order to respond to the challenges to extremely large turbines. For example, novel spiral case that has smaller size [19] and better flow conditions should be sought to replace the use of guide plate, which obviously disturbances flow significantly, resulting in high turbulence level in free-stream and consequent problems[20].
6. The B L behavior, such as transition length and scaling laws etc, should be investigated thoroughly This is particularly important for huge turbines. The size of their components[21]

[17] The sealing surface on the guide vane serves as a profile discontinuity which could be another source from generating boundary layer flow distortion. This needs to be considered in the analysis too.

[18] On scaled down model.

[19] As mentioned before, for high and medium specific speed turbine-generator units, spiral case is often the crucial component that determines the overall size of plant. Therefore, reduction of spiral case has a significant impact to the hydro scheme's economic feasibility. This is why manufacturers often take high risks to reduce the size of spiral case in order to win the bidding. No doubt, the idea of using guide plate, which has already encountered a break down event, has to be justified technically and economically.
The author has made a suggestion to the M & E department of CTGPC that the feasibilities of employing oval cross-section spiral case for the size reduction.

[20] The 3-D damage on the fillet of stay-vane immediately down stream of the guide-plate might be well explained by the disturbances introduced by the guide plate.

[21] Such as the chord lengths of stay vane and guide vane is well over one metre.

and the high free-stream velocity[22] make the critical Reynolds number[23],

$$\mathrm{Re}_{crit} = \frac{Ux_{crit}}{\nu},$$

to be reached in the FPG zone instead of APG zone, resulting in more susceptibility to cavitation inception compared with smaller turbines. Therefore, for large turbines, while scaling cavitation test data from model to prototype, the scaling effect due to the boundary property difference must be thoroughly studied. Currently our knowledge about the transition length in turbines is fairly poor compared with that of flat plate B L case. For gas turbines, a correlation[24] is found through experiments. That is, the Reynolds number Re_{lT} calculated with the transition length l_T^* is a linear function of $\mathrm{Re}_{\theta T}^{5/4}$, where $\mathrm{Re}_{\theta T}$ designates the momentum thickness Reynolds number at the end of transition [e.g. 4.29]. But for hydraulic turbines, little work has been done yet neither theoretically nor experimentally.

7. The damage occurred on the turbines presents no urgent need for remedy action, and turbines can be put into operation as usual.
8. The study on these fundamental issues will serve as a sound base for developing next generation of huge turbines (e.g. 1000 MW unit). An effort by multi-disciplinary study at international level is essential.

ACKNOWLEDGMENTS

The author would like to express his sincere thanks to the EPSRC's Warwick-IMRC for their long term financial support (R.ESCM.9001 and SCAP16) on cavitation and turbine technology; and to the CTGPC for their support during his visit to Three Gorge Station from 19th to 20th of March 2006.

[22] In the order of 20-30 m/sec.

[23] $3\times10^5 \sim 3\times10^6$ for flat plate at zero angle of attack, subject to free-stream turbulence level.

[24] Precisely the same correlation stems from processing experimental data for both smooth and rough surfaces.

REFERENCES

[4.1] Three Gorge Power Plant, 2006, 'Damage of Guide Vane Surface (Left Plant)', Document for the *in situ* Investigation Meeting, 12-14 March 2006, Yi Chang, China.

[4.2] S.C. Li. 2000. §6.2 'Cavitation Damage in Turbines', in *Cavitation of Hydraulic Machinery*, ICP, London

[4.3] A.S. Rao and D. Kung. 1987. Metallic Overlay Materials for the Optimum Cavitation Performance of Hydraulic Turbines, Report for the Canadian Electric Association, CEA No.135 G273.

[4.4] S.C. Li. 2000. §6.5 'High Resistance Materials' in *Cavitation of Hydraulic Machinery*, ICP, London.

[4.5] T. Sourmail and H.K.D.H. Bhadeshia. 'Stainless steel', www.msm.cam.ac.uk/phase-trans/2005/Stainless_steels

[4.6] M. Shimada, H. Kokawa, Z.J. Wang, Y.S. Sato and I. Karibe. 2002. 'Optimization of grain boundary character distribution for intergranular corrosion resistant 304 stainless steel by twin-induced grain boundary enngineering', Acta Materialia, 50, pp2331-2341.

[4.7] N. Alonso-Falleiros, M. Magri and I.G.S. Falleiros. 1999. 'Intergranular Corrosion in a Martensitic Stainless Steel Detected by Electrochemical Tests', Corrosion, Vol55, No8.

[4.8] J.W. Daily and V.E. Johnson. 1956. 'Turbulence and Boundary-Layer Effects on Cavitation Inception From Gas Nuclei', Transactions ASME , 78, pp1695-1706.

[4.9] V.H. Arakeri and A. Acosta. 1981. 'Viscous Effects in the Inception of Cavitation', ASME J. Fluid Eng. 103, pp280-287.

[4.10] T.T. Huang. 1981. 'Cavitation Inception Observations on Six Axisymmetric Headforms', ASME J. Fluid Eng. 103, pp273-279.

[4.11] E.M. Gates and A. Acosta. 1979. 'Some Effects of Several Freestream Factors on Cavitation Inception of Axisymmetric Bodies', 12th Symp. Naval Hydrodynamics, Washinfton D. C. pp86-112.

[4.12] S.C. Li. 2000. §3.7.4 'Bubble-Flow Field Interaction' in *Cavitation of Hydraulic Machinery*, ICP, London.

[4.13] R.E.A. Arndt and W.K. George. 1979. 'Pressure Fields and Cavitation in Turbulent Shear Flows', 12th Symp. Naval Hydrodynamics, Washington D. C., pp327-339.

[4.14] W.S. Saric, H.L. Reed and E.J. Kerschen. 2002. 'Boundary-layer Receptivity to Free-stream Disturbances', Annu. Rev. Fluid Mech. 2002. 34:291–319.

[4.15] O.S. Ryzhov. 2005. 'Transition length in turbine & compressor blade flows', Proc. R. Soc. A, doi: 10.1098 / rspa. 2005. 1651.

[4.16] M.V. Morkovin, E. Reshotko and T. Herbert. 1994. 'Transition in open flow systems—a reassessment', Bull. Am. Phys. Soc. 39:1882

[4.17] P. Wassermann and M. Kloker. 2005. 'Transition mechanisms in a three-dimensional boundary-layer flow with pressure-gradient changeover', J. Fluid Mech. (2005), vol. 530, pp. 265–293.

[4.18] Simons Roll Forming Co. 2006. 'Glossary of Metal Terms'. www.rollformedshapes.com/metalterms.htm.

[4.19] X. Wu and J. Luo. 2001. 'Instability of Blasius boundary layer in the presence of steady streaks', *Annual Research Briefs* 2001, Centre for Turbulence Research.

[4.20] H.L. Dryden. 1936. 'Air flow in the boundary layer near a plate', *NACA Report* 562.
[4.21] P. Bradshaw. 1965. 'The effect of wind-tunnel screens on nominally two-dimensional boundary layers', *J. Fluid Mech*. 22, 679-687.
[4.22] J.M. Kendall. 1985. Experimental study of disturbances produced in pre-transitional laminar boundary layer by weak free stream turbulence. AIAA Paper 85-1695.
[4.23] K.J. Westin, A.V. Boiko, B.G.B. Klingmann, V.V. Kozlov and P.H. Alfredsson. 1994. Experiments in a boundary layer subjected to free stream turbulence. Part I. Boundary layer structure and receptivity. *J. Fluid Mech*. 281, 193-218.
[4.24] P.S. Klebanoff. 1971. 'Effect of free-stream turbulence on a laminar boundary layer', *Bulletin. Am. Phys. Soc*. 16.
[4.25] P. Andersson, M. Berggren and D. Henningson. 1999. 'Optimal disturbances and bypass transition in boundary layers', *PHYSICS OF FLUIDS* , 11(1), January 1999
[4.26] L. Brandt, P. Schlatter and D. Henningson. 2004. 'Transition in boundary layers subject to free-stream turbulence', *J. Fluid Mech.* (2004), vol. 517, pp. 167–198
[4.27] J.H. Watmuff. 2004. 'Evolution of a Turbulent Wedge from a Streamwise Streak', 15th Australasian Fluid Mechanics Conference, The University of Sydney, Sydney, Australia, 13-17 December 2004.
[4.28] T. Chong, S. Zhong and H. Hodson. 2005. 'Visulization of Turbulent Wedges under Favourable Pressure Gradients using Shear Sensitive and Temperature-sensitive Liquid Crystals'.
[4.29] O. Ryzhov. 2005. 'Transition length in turbine/compressor blade flows', *Proc. R. Soc*. A, doi:10.1098/rspa.2005.1651.

Invited Lecture

5.6 CAVITATION INSTABILITIES IN TURBO-PUMP INDUCERS FOR ROCKET ENGINES

Professor Yoshinobu Tsujimoto
Engineering Science, Osaka University, Osaka, Japan
tujimoto@me.es.osaka-u.ac.jp

ABSTRACT

In modern turbo-pumps for rocket engines, two-dimensional cavitation instabilities such as rotating cavitation are major concerns, in addition to the classical one-dimensional cavitation instability, cavitation surge. The present paper focuses on these two-dimensional instabilities. Characteristics of rotating cavitation are discussed based on experimental observations. In order to clarify the relations among instabilities in turbo-machines, surge, rotating stall, cavitation surge, and rotating cavitation, a one-dimensional analysis is introduced. In this analysis the characteristics of cavitation are represented by two factors that should be evaluated by other appropriate methods. Next, a closed blade surface cavity model is employed to show various types of cavitation instabilities. Most cavitation instabilities occur when the cavity length is about 65% of the blade spacing, where the performance degradation due to cavitation is insignificant. A cavitation instability associated with the degradation of pressure performance due to cavitation is treated in the last section.

NOMENCLATURE

A : Tank free surface area
a : Non-dimensional cavity volume
B : Greitzer's B factor
C : Compliance of a tank, chord length
f : Frequency, cross-sectional area of inlet pipe
f_0 : Rotational frequency
g : Gravitational acceleration constant
h : Blade spacing
j : Imaginary unit
$k^* = k_R^* + jk_I^*$: Complex frequency
K : Cavitation compliance
L : Inlet conduit length
l : Chord length
l_s : Cavity length
M : Mass flow gain factor
p : Pressure
p_v : Vapor pressure
Q : Flow rate
R : Resistance of exit valve
St : Strouhal number
U_T : Rotor tip velocity
U : Mean axial velocity
V : Tank volume
V_p : Propagation velocity
V_c : Cavity volume
α : Incidence angle
β : Blade angle
$\theta_{n,n+1}$: Inter-blade phase difference of disturbance
P : Density
σ : Cavitation number
τ : Cavitation number
ϕ : Flow coefficient
ψ : Head coefficient
ω : Complex frequency
Ω : Rotational frequency of rotor

5.1 ROTATING CAVITATION

Extensive studies on unsteady cavitation in turbopump inducers (C.E. Brennen, and A.J. Acosta, [5.1], C.E. Brennen, [5.2], C.E. Brennen, C. Meissner, E.Y. Lo and G.S. Hoffmann, [5.3]) have been made during 1960-1982 associated with POGO instability (Rubin, [5.4]), which is a coupled instability between longitudinal structural vibration and the propulsion system. From the viewpoint of propulsion system including turbo-pump, the oscillation is one-dimensional with the same phase disturbances for all of the blades. For this case the unsteady cavitation characteristics can be represented by a transfer matrix, which correlates the flow rate and pressure fluctuations at the pump inlet and discharge. Even without the coupling with the structural mode, cavitating turbo-pump systems may suffer from one-dimensional system instability called cavitation surge. In addition to these system instabilities, modern turbo-pumps are suffering from local two-dimensional instabilities such as rotating cavitation. The present paper focuses on these local two-dimensional instabilities.

5.1.1 ROTATING CAVITATION IN 3-BLADED INDUCERS

The first detailed report of rotating cavitation was made by Rosenmann [5.5] on a three bladed inducer with the blade angle of 8.99^{o} and the solidity of 1.99 at the tip, with the design flow coefficient of $\phi_d = 0.111$ corresponding to a tip incidence angle of 2.66 degrees. The observation was made by the unsteady force measurement on the rotor. Figure 5.1 shows the results obtained at the design flow coefficient. Here, $\tau = (p_1 - p_v)/(\rho U_T^2/2)$ is the cavitation number, $\psi_H = \Delta p_t/(\rho U_T^2)$ the head coefficient, $\psi_p = \psi_H/\eta$ the power coefficient with the hydraulic efficiency η, C_s the force vector rotation coefficient defined as (rotational speed of radial force vector)/(shaft rotational speed) which corresponds to the propagation velocity ratio defined as (rotational speed of cavitating region)/(shaft rotational speed). C_R is the radial force vector coefficient normalized by the axial force evaluated as the product of the pressure difference across the inducer and the cross sectional blade area at inducer exit.

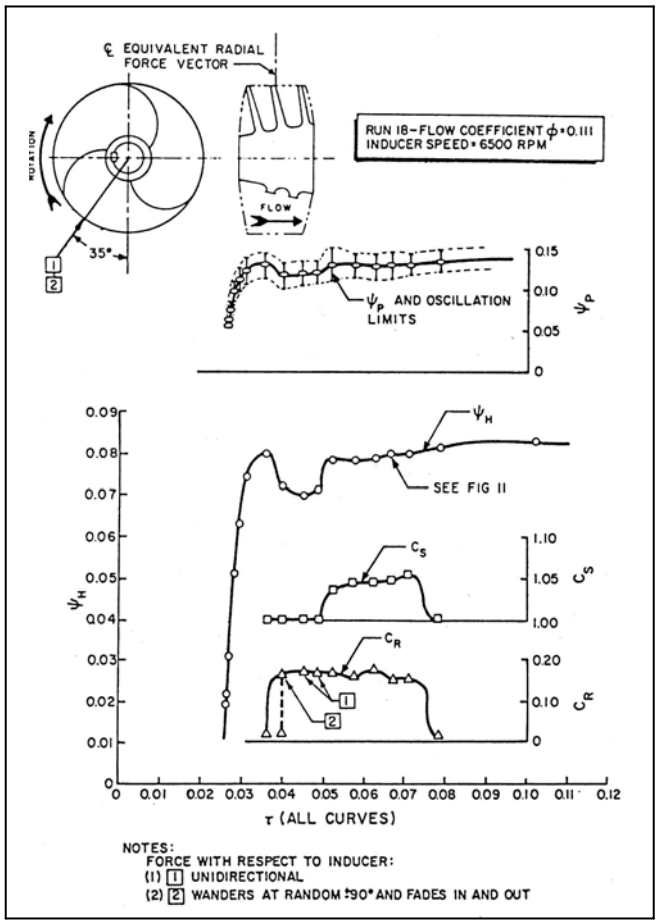

Figure 5.1: Radial forces, head coefficient vs cavitation number

We observe the following important characteristics of rotating cavitation:

(1) The rotating cavitation is observed at the design flow rate. This is quite different from the rotating stall that occurs at partial flow rate.

(2) The force vector rotation coefficient C_s is larger than 1, which means that the cavitating region rotates faster than the impeller. This is also different from rotating stall in which the stalled region rotates slower than the impeller.

(3) As the cavitation number τ is decreased, the radial force C_R suddenly increases at a certain cavitation number τ. There, the rotation coefficient is $C_S \approx 1.05 > 1$ and then it decreases to 1 with further decrease in τ.

(4) In a certain range of cavitation number ($0.035 < \tau < 0.050$) the radial force rotates fixed to the rotor and sometimes wanders at random. This is called attached asymmetric cavitation.

The radial force decreases when the head starts to decrease steeply (this is called "head breakdown"). This means that rotating cavitation occurs in a range of cavitation number just above the head breakdown cavitation number. The small head decrease under the occurrence of rotating cavitation and the attached asymmetric cavitation is a result of those cavitation instabilities.

The first visual observation of rotating cavitation was made by Kamijo et al. [5.6] on a three bladed inducer with the inlet blade angle 10^o and the solidity 2.5 at the tip. Figure 5.2 shows the pictures from a high-speed film arranged to show the size of the cavity on each blade on every turn.

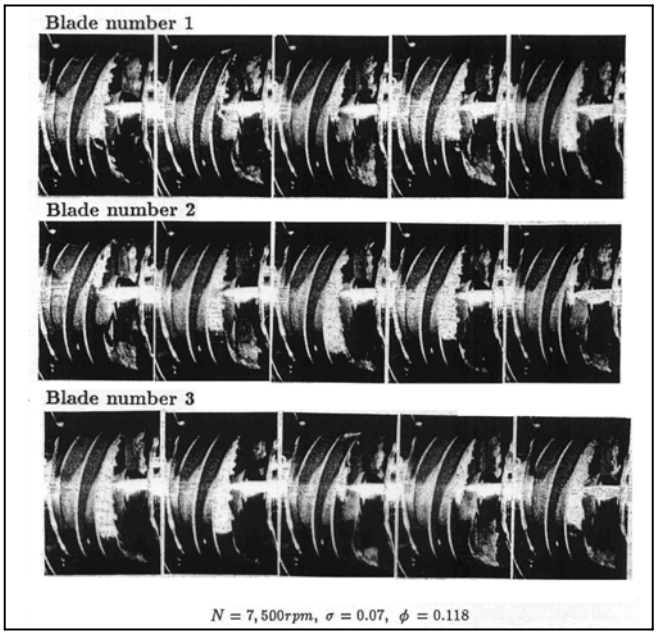

Figure 5.2: Rotating cavitation. Pictures are arranged to show the cavity size on each blade. The blades pass in the order of Blade number 1, 2, and 3. Time proceeds from left to right.

The blade passes in the order of blade number 1, 2 and 3. The time proceeds from left to right. Here we focus on the shorter cavity. It moves from blade number 2 to 1 then 3 and returns to the original blade 2, in 4 turns of the impeller. Thus the cavity moves in the direction of impeller rotation and makes complete one turn relative to the impeller, while the impeller makes 4 turns. This means that the propagation velocity ratio is (4+1)/4=1.25.

5.1.2 ROTATING CAVITATION AND ALTERNATE BLADE CAVITATION IN 4-BLADED INDUCERS

To study the cavitation instabilities in a 4-bladed inducer, water and liquid hydrogen tests were made with VULCAIN liquid hydrogen turbo-pump inducer (Goirand et al.,[7]). Figure 5.3 shows the sketch of the cavity and the spectrum of pressure fluctuation at nominal flow coefficient obtained from a water test.

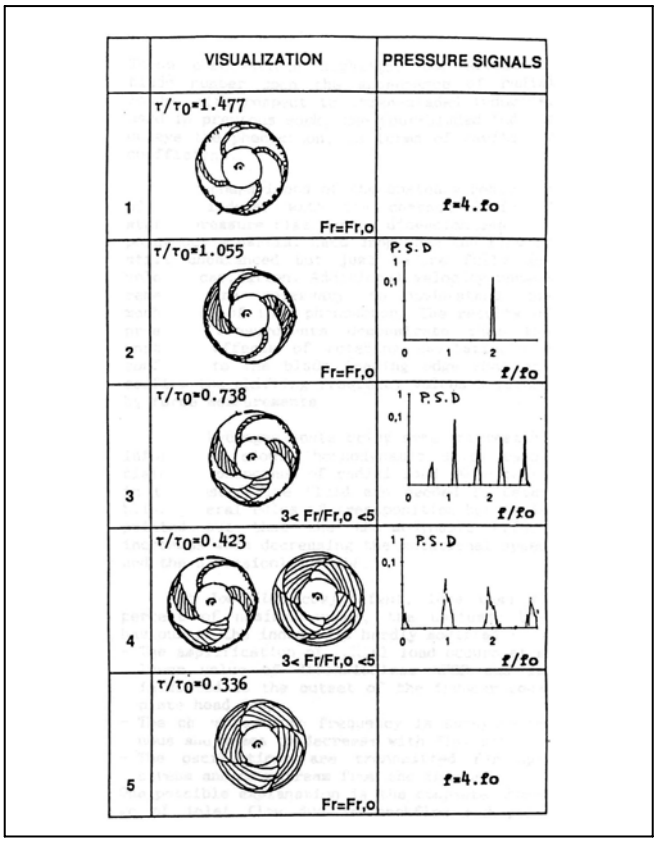

Figure 5.3: Cavity pattern at nominal flow rate

It is reported that no significant dependence on the rotational speed was found in the water tests. In this figure, τ and τ_0 are the cavitation number and the reference cavitation number, f and f_0 are the frequency of the pressure fluctuation and the rotational frequency of the impeller, F_r and $F_{r,0}$ are the radial forces under cavitating and non-cavitating conditions, respectively.

(1) At sufficiently large cavitation number with $\tau/\tau_0 = 1.477$, equal cavity appears on each blade and the frequency of the pressure fluctuation is $4f_0$, the blade passing frequency.

(2) At $\tau/\tau_0 = 1.055$, alternate blade cavitation appears with stable and balanced pattern, with the pressure fluctuation of $f/f_0 = 2.0$.

(3) At $\tau/\tau_0 = 0.738$, rotating cavitation with unbalanced geometry appears. The frequency of pressure fluctuation is slightly higher than the rotational frequency. Radial force is 3 to 5 times that under non-cavitating condition.

(4) At $\tau/\tau_0 = 0.423$, either of the following two modes occurs. One is the unbalanced pattern fixed to the impeller with the pressure fluctuation of $f/f_0 = 1.0$. The other is balanced equal cavitation.

(5) At $\tau/\tau_0 = 0.336$, stable and balanced flow with fully developed cavitation occurs at the beginning of inducer head drop.

The frequency ratio f/f_0 of the rotating cavitation is summarized in Figure 5.4.

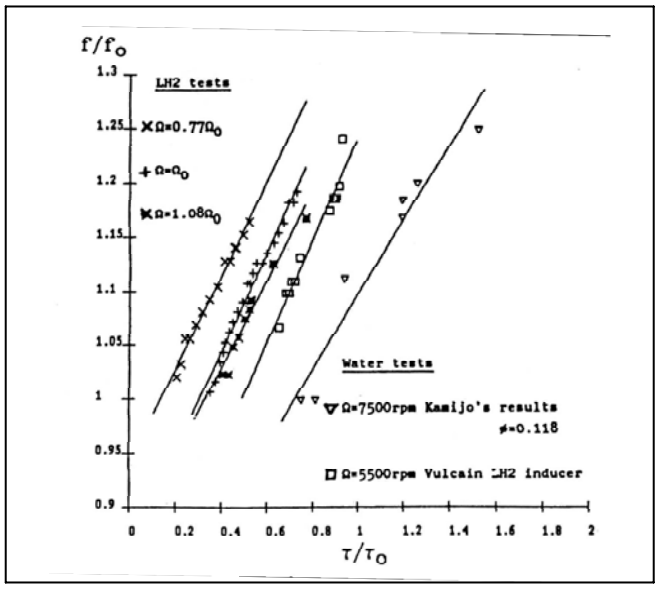

Figure 5.4: Propagation velocity ratio f/f_0 against cavitation number τ/τ_0.

The results of liquid hydrogen (LH2) tests with three rotational speeds $\Omega = 0.77\Omega_0, 1.0\Omega_0, 1.08\Omega_0$ (Ω_0 is the reference speed) and the results of 3-bladed inducer by Kamijo et al. [5.6] are also shown. The range of frequency and its dependence on the cavitation number are the same for all cases. If we compare the results of water tests with three (Kamijo's) and four (Vulcain LH2) bladed inducers, we find that the onset cavitation number is shifted to lower values for the case with the four bladed inducer. This is caused by the alternate blade cavitation, which occurs at a larger cavitation number for the case with 4-bladed inducer. In the LH2 test, the occurrence region is shifted to still smaller cavitation number, caused by the thermal effect.

5.2 ONE DIMENSIONAL STABILITY ANALYSIS

Cavitation instabilities in inducers can be sorted into two types, cavitation surge and rotating cavitation, although they include various higher order modes. Cavitation surge is a system instability in which the flow rate of the hydraulic system fluctuates with in-phase cavity fluctuations on each blade. The effects of various system parameters on cavitation surge are examined in detail by Young [5.8]. Rotating cavitation is a local cavitation instability in which the cavities propagate from blade to blade in the same way as rotating stall. In the most typical mode, the cavitating region rotates faster than the impeller for rotating cavitation, while the stalled region rotates slower than the impeller in rotating stall.

Rotating cavitation, as well as cavitation surge, can be treated by assuming that the cavity volume V_c is a function of the cavitation number $\sigma_1 = (p_1 - p_v)/(\rho W_1^2/2)$, (p_1: inlet pressure, p_v: vapour pressure, ρ: liquid density, W_1: inlet relative velocity) and the local incidence angle to the blade α_1 (Tsujimoto et al., [5.9]). The cavity volume is normalized by using the blade spacing h and is represented by a:

$$a(\sigma_1, \alpha_1) = V_c/(h^2 \times 1) \qquad (1)$$

Then, the mass flow gain factor M and the cavitation compliance K are defined as

$$M = \frac{\partial a}{\partial \alpha_1} \quad \text{and} \quad K = -\frac{\partial a}{\partial \sigma_1} \qquad (2)$$

Since the cavity volume will increase if the incidence angle is increased or the inlet pressure is decreased, both mass flow gain factor and cavitation compliance should have positive values. These parameters are introduced by Brennen and Acosta [5.1] and evaluated from quasi-steady calculations

of blade surface cavitation. An extensive series of experiments were carried out and the results are reported in Ng and Brennen [5.10] and Brennen et al. [5.3]. These are still the only reliable data and are recently assessed to include the dependence on the frequency (Rubin, [5.11]). A bubbly flow model was proposed by Brennen [5.2] which can predict not only the values of M and K but also of all the transfer matrix elements correlating the pressure and mass flow fluctuations at the pump inlet and exit. Otsuka et al. [5.12] carried out unsteady calculations of blade surface cavitation and represented M and K as complex functions of the frequency.

One-dimensional linear stability analyses are possible for surge, rotating stall, cavitation surge, and rotating cavitation (Tsujimoto et al., [5.13]). We consider a system composed of an inlet conduit, an impeller cascade with infinite number of blades, a downstream tank, and an exit valve, as shown in Figure 5.6.

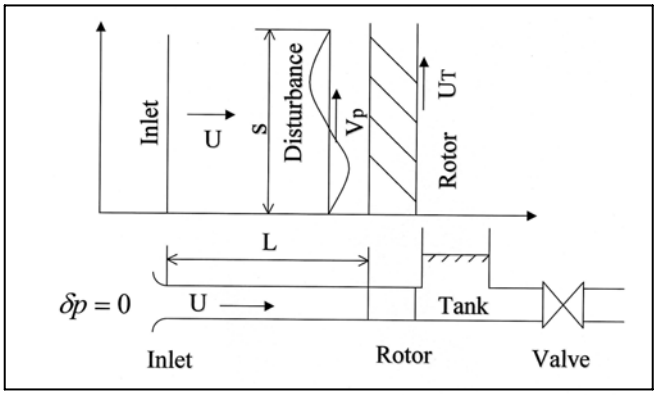

Figure 5.6: The hydraulic system for the analysis of instabilities in turbo-machinery

The velocity triangle at the inlet of the impeller is shown in Figure 5.7. For one-dimensional instabilities of surge and cavitation surge, an axial velocity disturbance in a finite length upstream pipe is considered. For two-dimensional instabilities of rotating stall and rotating cavitation, a two-dimensional sinusoidal potential flow disturbance is assumed in the upstream of the impeller. In both cases the pressure fluctuation at the inlet of the impeller can be correlated with the axial flow velocity disturbance by applying the momentum equation to the inlet flow.

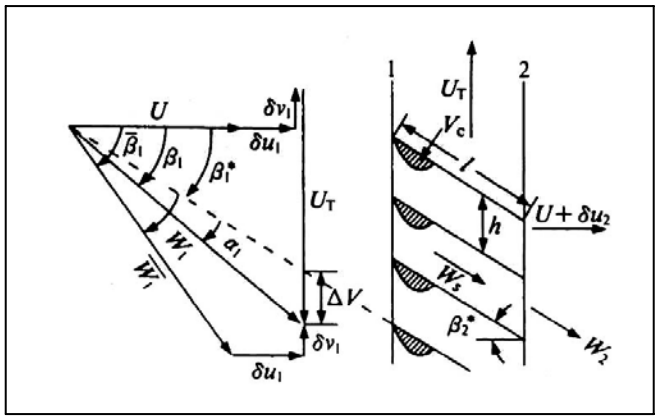

Figure 5.7: Velocity triangle at the inlet

This is why one-dimensional stability analysis is possible also for two-dimensional instabilities such as rotating stall and rotating cavitation. The pressure increase in the impeller is obtained by assuming that the flow in the impeller is perfectly guided by the blades. To simulate surge and rotating stall, two types of loss are assumed: an incidence loss proportional to the loss coefficient ς_s and the square of the incidence velocity ΔV at the inlet, and a through flow loss proportional to the loss coefficient ς_Q and the square of the relative flow velocity W_s through the impeller flow channel.

The effect of cavitation is taken into account in the continuity relation across the impeller by representing the cavitation characteristics by M and K. If we represent the axial velocity disturbance at the inlet and the outlet of the impeller by δu_1 and δu_2, respectively, and represent the cavity volume per blade by V_c, the continuity equation across the impeller can be represented by

$$h(\delta u_2 - \delta u_1) = (\partial / \partial t)\delta V_c \qquad (3)$$

If we consider that the cavity volume is a function of the cavitation number σ_1 and the incidence angle α_1, the cavity volume fluctuation can be expressed as

$$\delta V_c = h^2 (M\delta\alpha_1 - K\delta\sigma_1) \qquad (4)$$

with the mass flow gain factor M and the cavitation compliance K defined in Eq.(2). The effect of cavitation on the pressure performance of the impeller is neglected since most of cavitation instabilities occur in a range where the pressure

performance is not affected by the existence of cavitation.

5.2.1 SURGE, ROTATING STALL, CAVITATION SURGE, AND ROTATING CAVITATION

To obtain simple expressions of the onset condition and the frequency of surge, rotating stall, cavitation surge, and rotation cavitation, various simplifying assumptions are made for each instability. For cavitation surge and rotating cavitation, it is assumed that the downstream flow rate fluctuation does not occur. This is a good approximation for typical inducers with a smaller blade angle. For surge, it is assumed that the flow from the rotor is discharged to a surge tank followed by an exit valve. For rotating stall, it is assumed that the flow from the impeller is discharged directly to a space of constant pressure. By writing down the relations connecting the flow disturbances in the upstream and the downstream of the impeller, we obtain a set of linear equations in terms of the amplitudes of fluctuations. From the coefficient matrix of the linear equations, we obtain a polynomial characteristic equation in terms of a complex frequency whose real part represents the frequency and the imaginary part the damping rate of possible instability mode.

Instability	Onset condition	Frequency
Surge	$\frac{\partial \psi_{ts}}{\partial \phi} > \frac{1+(1/\cos\beta^*)(l/L)}{B^2\phi R}$	$n=\frac{1}{2\pi}\frac{1}{\sqrt{\rho CL}}\sqrt{\frac{1+(1/R)\left[L_u+\left(1/\cos^2\beta_2^*\right)\right]}{[1+(1/\cos\beta^*)l/s]}}$
Rotating stall	$\frac{\partial \psi_{ts}}{\partial \phi} > 0$	$\frac{V_p}{U_T}=1-\frac{2\zeta_s[1-(\phi/\phi^*)]}{1+(2\pi/\cos\beta_1)l/s]}<1$
Cavitation surge	$M > 2(1+\sigma)\phi K$	$n=\frac{U_T}{2\pi}\frac{1}{\sin\bar{\beta}_1}\frac{1}{\sqrt{2KLh}}$
Rotating cavitation	$M > 2(1+\sigma)\phi K$	$V_p/U_T > 1, \quad V_p/U_T < 0$

Table 5.1 The onset condition and the frequency of instabilities in turbo-machinery

The onset conditions and the frequencies obtained by solving the characteristic equations are summarized in Table 5.1, where $\psi_{ts}=(p_2-p_{t1})/(\rho U_T^2)$ is the inlet total to outlet static pressure coefficient of the impeller, $\phi=U/U_T$ is the flow coefficient, with the mean axial velocity U and the circumferential velocity of the impeller U_T, β*is the mean blade angle measured from axial direction, l is the chord length of the blades, L is the length of the inlet conduit, R is the resistance of the exit valve, $B=\sqrt{\rho C/L}U_T$ is called Greitzer's B factor, with the compliance of a tank placed downstream of the impeller $C=V/(\rho a^2 f)$ for liquids or $C=A/(\rho g f)$ for gas, V the volume of the tank, a the speed of sound, f the cross-sectional area of the inlet pipe, A the free surface area of the surge tank, and g the gravitational acceleration constant. L_u is an impeller loss coefficient and β_2^* the blade outlet angle. s is the circumferential wavelength of the disturbance, $\bar{\beta}_1$ the mean flow angle at the inlet and ϕ^* the incidence free flow coefficient. V_p is the propagation velocity of rotating stall and rotating cavitation observed in a stationary frame, and n is the frequency of surge and cavitation surge.

The results shown in Table 5.1 show the following characteristics.

(1) Both surge and rotating stall occur at small flow rates with a positive slope of $\psi_{ts}-\phi$ performance. Under this condition, the head produced by the rotor will increase if the flow rate is increased, which accelerate the flow and results in further increase of the flow rate. This positive feedback is the cause of surge and rotating stall.

(2) Both cavitation surge and rotating cavitation occur when $M > 2(1+\sigma_1)\phi K$.

(3) The frequency of surge is basically identical to $n=1/(2\pi\sqrt{\rho CL})$, the natural frequency of a Helmholtz resonator composed of a tank with the compliance C and an inlet pipe with the length L, and does not depend on the impeller speed.

(4) The frequency of cavitation surge is proportional to the impeller speed U_T and inversely proportional to the square root of L and K. This shows that cavitation surge is an oscillation of the upstream fluid associated with the compliance of cavitation in the impeller.

(5) The propagation velocity ratio defined as V_p/U_T for rotating stall is less than 1, suggesting that the stalled region rotates slower than the impeller.

(6) Two modes of rotating cavitation are predicted. One of them rotates faster than the impeller and this mode is generally observed in experiments (Tsujimoto et al., [5.14]). The other mode

rotates slower than the impeller and occasionally observed as a mode rotating in the opposite direction of the impeller. This will be discussed in the following section.

The criterion $M > 2(1+\sigma_1)\phi K$ for the onset of cavitation surge and rotating cavitation clearly shows the importance of the positive mass flow gain factor for which the cavity volume decreases as the flow rate increases. The mechanism of the instability can be explained as follows. When the flow rate is increased, the angle of attack to a rotor blade is decreased. If the value of mass flow gain factor is positive, the cavity volume will also decrease from the definition of mass flow gain factor. If the cavity volume is decreased, the inflow to the rotor will increase to fill up the space occupied by the cavity volume decreased. Thus, the increase of flow rate results in further increase of flow rate. This mechanism of instability depends totally on the continuity relation and is not associated with impeller performance. Actually, both rotating cavitation and cavitation surge occur at a higher inlet pressure where the performance degradation due to cavitation is insignificant.

On the contrary, positive cavitation compliance has an effect to suppress instabilities: when the inlet flow rate is increased, the inlet pressure will decrease due to the Bernoulli effects and the cavity volume will increase if $K > 0$, resulting in the decrease of the inlet flow rate. So, $K > 0$ provides negative feedback and stabilizes the system. The onset condition of cavitation surge and rotating cavitation does not depend on the steady $\psi_{ts} - \phi$ performance and they may occur even at the design flow rate. This makes the cavitation instabilities more serious than surge and rotating stall that occur at off design points. The mechanism of instabilities in turbo-machinery is summarized in Figure 5.8.

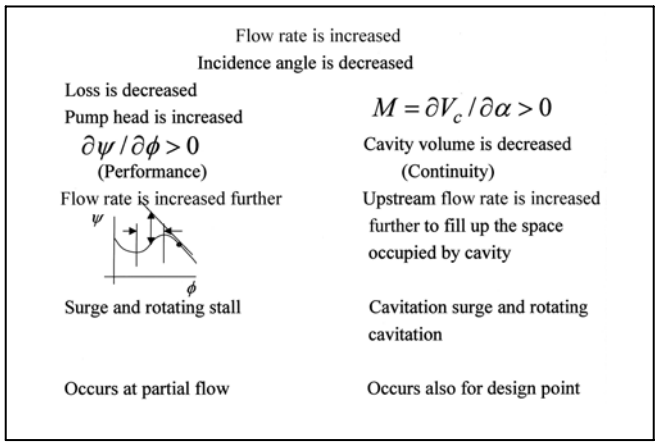

Figure 5.8: Mechanisms of instabilities in turbo-machinery

5.2.2 RELATION BETWEEN ROTATING STALL AND ROTATING CAVITATION

In order to illustrate the relation between rotating stall and rotating cavitation, a stability analysis was made under the assumption that the two-dimensional flow extends to upstream and downstream infinity (Tsujimoto, [5.9]). In the downstream, the flow is composed of a potential flow disturbance and a vortical flow disturbance due to the vorticity shed from the impeller caused by the unsteadiness of the flow. The mass continuity and pressure rise relations across the cascade result in a third order characteristic equation of the non-dimensional frequency k^* whose real part k_R^* gives the propagation velocity ratio V_p/U_T and the imaginary part k_I^* the damping rate:

$$(k^* - k_1^*)(k^* - k_2^*)(k^* - k_3^*) = 0 \qquad (5)$$

Examination of three roots of Eq.(5). Figure 5.9 shows the roots for an inducer tested by Kamijo et al. [5.6] for which the first detailed visual observation of rotating cavitation was made.

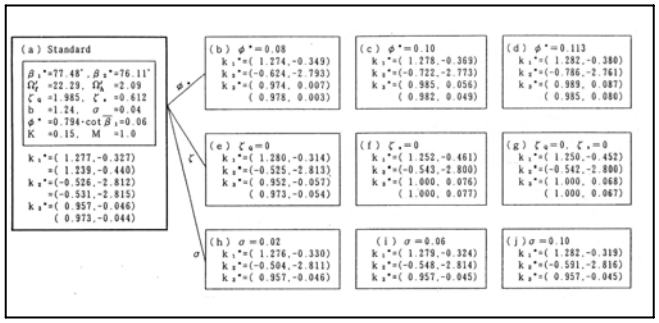

Figure 5.9: Solutions of Eq.(5) showing rotating cavitation (k_1^*, k_2^*) and rotating stall k_3^*

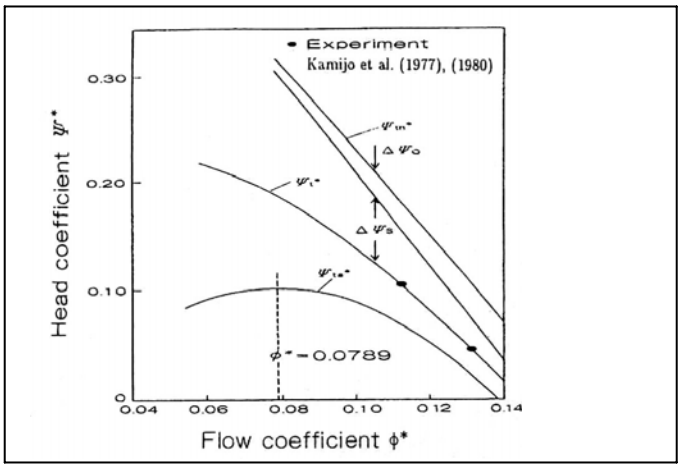

Figure 5.10: Static performance of the inducer

The static performance of the inducer is shown in Figure 5.10, from which the values of the loss coefficients ζ_Q and ζ_S are determined. In this figure, ϕ^* and ψ^* are the flow and pressure coefficients normalized by using the inducer tip speed. $\psi_{th}{}^*$ is the Euler's head at the mean radius, $\psi_t{}^*$ is the total head and $\psi_{ts}{}^*$ is the inlet total to outlet static pressure coefficient. Figure 5.9 (a)-(j) show the three roots, $k_i{}^* = (k_{Ri}{}^*, k_{Ii}{}^*), i = 1,3$, of the characteristic equation (5), with the value of parameters which is different from the standard values shown in (a). They are assigned to $k_1{}^*, k_2{}^*$ and $k_3{}^*$ following the criteria ($k_{R1}{}^* > 1$, $k_{R2}{}^* < 0$ and $k_{R3}^* < 1$). The values in the lower line of $k_1{}^*$ and $k_2{}^*$ in (a) are the values for the rotating cavitation obtained from the simplified analysis discussed in the preceding section, and the values in the lower line of $k_3{}^*$ in (a)-(g) are the values for rotating stall by the simplified analysis.

As shown in Figure 5.9(a), the values of $k_1{}^*$, $k_2{}^*$ and $k_3{}^*$ are close to the values determined from the simplified analysis. This suggests that $k_1{}^*$ and $k_2{}^*$ represent the rotating cavitation and $k_3{}^*$ the rotating stall, and that they can be approximately treated by the simplified method outlined in the last section. For the standard case (a), the imaginary parts of $k_1{}^*, k_2{}^*$ and $k_3{}^*$ are all negative, showing that both rotating cavitation and rotating stall can occur simultaneously. The fact that the root $k_3{}^*$, which represents rotating stall estimated under the effect of cavitation, is close to the non-cavitating rotating stall solution, means that the rotating stall is not affected largely by the cavitation. As shown in (b)-(g), the rotating stall is damped ($k_{I3}{}^* > 0$) when ϕ^* increases or the shock loss is neglected. On the other hand, the values of $k_1{}^*$ and $k_2{}^*$ are almost independent on the values of ϕ^*, ζ_Q, ζ_S and σ, so long as the values of M and K are kept constant. Rotating cavitations are amplified even with a negative slope of $\psi_{ts}{}^*$ at larger ϕ^* or with $\zeta_S = 0$, which is quite different from the case of rotating stall.

		$k^* = k_1^*$	$k^* = k_2^*$	$k^* = k_3^*$
$\lvert\delta p_2/\rho U_2^2\rvert$	=	(0.0591)	(0.00836)	(0.0497)
$\lvert\delta u_1/U_1\rvert$	=	(0.0563)	(0.00257)	(0.0783)
$\lvert\delta u_2/U_2\rvert$	=	(0.0129)	(0.00020)	(0.0713)

Table 5.2: Amplitudes of pressure and velocity fluctuations

Table 5.2 shows the relative amplitudes of the pressure and axial velocity fluctuations at the inlet and outlet of the cascade, for the case of Figure 5.9(a) and corresponding to $\delta p_1 / \rho U_1^2 = 1$. For each case δp_2 is much smaller than δp_1. For rotating cavitation ($k_1{}^*$ and $k_2{}^*$), δu_2 is small compared with δu_1, showing that the fluctuation at the inlet is almost absorbed by the change of cavity volume. This is caused by the fact that the blade angle $\beta_2{}^*$ is close to $\pi/2$, and supports the experimentally obtained conclusion (Kamijo et al., [5.6]) that "rotating cavitation is related mainly to the inlet flow conditions." On the other hand, for rotating stall ($k_3{}^*$), δu_2 is nearly equal to δu_1, with a small effect of cavity volume change.

As shown above, direct effects of ϕ^* and σ on $k_1{}^*$ and $k_2{}^*$ are small. It can be shown that $k_1{}^*$ and $k_2{}^*$ are mainly dependent on M and K. Since M and K are functions of ϕ^* and σ, rotating cavitations are affected by ϕ^* and σ through the values of M and K.

Rotating cavitation. Contour maps of k_1* and k_2* in the M - K plane are shown in Figures 5.11 and 5.12.

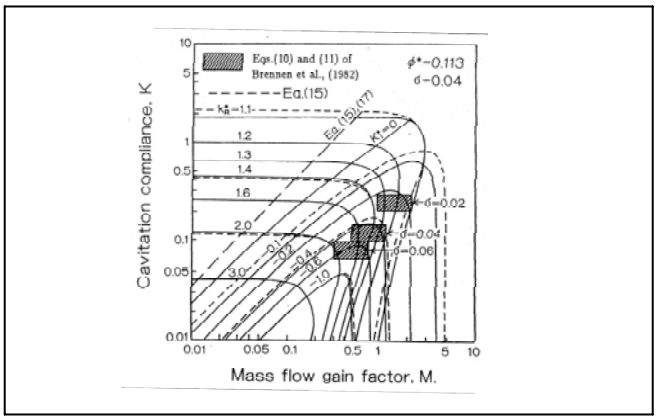

Figure 5.11: Forward mode k_1*

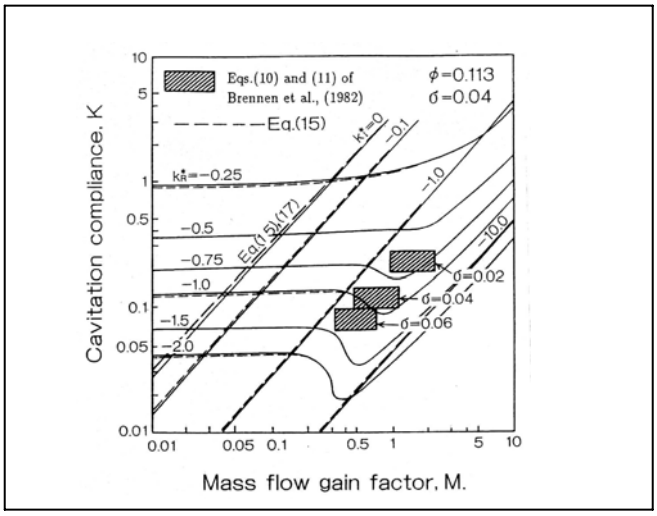

Figure 5.12: Backward mode k_2*

The values of parameters not specified in the figures are the same as those in Figure 5.9 (a). The solid lines are obtained from Eq.(5), while the broken lines are determined from the simplified analysis ("Eqs.(15), (17) " in the figure show the results of the simplified analysis). The difference between these results is small, showing that the simplified analysis simulates rotating cavitation very well. The neutral stability curve is shown by the solid line of k_I* = 0, which is close to the criterion obtained by the simplified analysis. The rotating cavitation grows in the region with k_I* < 0, beneath the neutral stability curve.

In order to make comparisons with experimental results, calculations were made also for $\sigma = 0.06$ and 0.02. It was found that the contour maps are almost unchanged. Hence, the ranges of M and K for three values of σ are shown in the figures, estimated from Brennen et al., [5.3]. For k_1* shown in Fig.2.6, the propagation velocity ratio for $\sigma = 0.02$ is k_R* = 1.1 – 1.4, which is close to the experimental value of k_R* = 1.16 (Kamijo et al., [5.6]). As we reduce the cavitation number, the estimated ranges of M and K shifts to the location with smaller propagation velocity ratio k_R*. The experiment shows a similar tendency. Figure 2.8 shows the super synchronous shaft vibration of LE-7 LOX turbo-pump caused by the k_1* rotating cavitation.

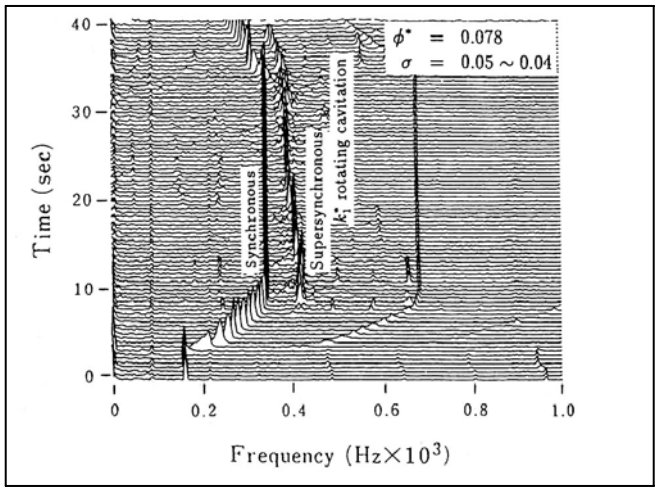

Figure 5.13: Super synchronous shaft vibration caused by forward rotating cavitation

The reduction of the super synchronous frequency with time is caused by the reduction of the inlet pressure with time, showing the above-mentioned tendency.

Since k_{R2}* < 0, the characteristic root k_2* corresponds to a mode of rotating cavitation, which propagates in the direction opposite that of the impeller rotation. This backward rotating cavitation was found later by Hashimoto et al. [5.15]. The propagation velocity ratio V_p / U_T observed was –1.36 at $\sigma = 0.072$, which agrees with the result in Fig.2.7 k_R* ≈ –1.25 for $\sigma = 0.06$.

Usually, only forward rotating cavitation corresponding to k_1* is observed and the observation of the backward rotating cavitation corresponding to k_2* is limited to a few cases. This contradicts to the results of Figures 5.11 and 5.12, in which the amplifying rate $-k_I$* is much larger for the backward rotating cavitation k_2*.

5.3 2-D FLOW STABILITY ANALYSIS BASED ON CLOSED CAVITY MODEL

The analysis in the preceding section is basically one-dimensional and only the effect of total cavity volume fluctuation is included. The stability analysis of two-dimensional cavitating flow using a closed model of blade surface cavitation is presented in this section.

5.3.1 METHOD OF STABILITY ANALYSIS

We consider a cascade as shown in Figure 5.14 (Horiguchi et al., [16-17], Watanabe et al., [18]).

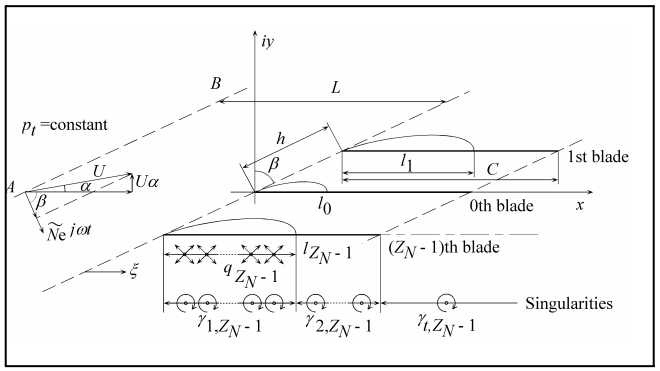

Figure 5.14: 2D stability analysis of cavitating flow through a cascade

For simplicity, we assume that the downstream conduit length is infinite and no velocity fluctuation occurs there. The upstream conduit length is assumed to be finite, L, in the x -direction and connected to a space with constant (static = total) pressure at the inlet AB.

We assume small disturbances with time dependence $e^{j\omega t}$ where $\omega = \omega_R + j\omega_I$ is the complex frequency with ω_R the frequency and ω_I the damping rate, to be determined from the analysis. The velocity disturbance is represented by a source distribution $q(s_1)$ on the cavity region, vortex distributions $\gamma_1(s_1)$ and $\gamma_2(s_2)$ on the blades, and the free vortex distribution $\gamma_t(\xi)$ downstream of the blades, shed from the blades associated with the blade circulation fluctuation. We divide the strength of those singularities and the cavity length into steady and unsteady components, and represent the velocity with steady uniform velocity $(U, U\alpha)$, the steady disturbance (u_s, v_s), and the unsteady disturbance $(\tilde{u}, \tilde{v})$. We assume that $\alpha << 1$, $|\tilde{u}|, |\tilde{v}| << |u_s|, |v_s| << U$ and neglect higher order small terms.

The boundary conditions are:

(1) The pressure on the cavity should be vapour pressure.

(2) The normal velocity on the wetted blade surface should vanish.

(3) The cavity should close at the (moving) cavity trailing edge (closed cavity model).

(5) The pressure difference across the blades should vanish at the blade trailing edge (Kutta'scondition).

(6) Upstream and downstream conditions: the total pressure along AB is assumed to be constant and the downstream velocity fluctuation is assumed to be zero.

By specifying the strength of the singularity distributions at discrete points on the coordinates fixed to the fluctuating cavity as unknowns, the boundary conditions can be represented by a set of linear equations in terms of those unknowns. If the unknowns are separated into steady and unsteady components, the steady boundary conditions result in a set of non-homogeneous linear equations. This set of equations can be used to show that the steady cavity length l_s normalized by the blade spacing h, l_s/h is a function of $\sigma/2\alpha$. On the other hand, the unsteady component of the boundary conditions results in a set of homogeneous linear equations. For non-trivial solutions, the determinant of the coefficient matrix should be zero. Since the coefficient matrix is a function of the steady cavity length and complex frequency, the complex frequency $\omega = \omega_R + j\omega_I$ is determined from this relation as a function of the steady cavity length l_s/h, or equivalently of $\sigma/2\alpha$. This shows that the frequency ω_R and the damping rate ω_I, as well as

possible modes of instability, depend only on the steady cavity length l_s / h, or equivalently on $\sigma / 2\alpha$, once the geometry and other flow conditions are given.

5.3.2 RESULTS OF STABILITY ANALYSIS

The steady cavity length obtained by assuming equal cavity on each blade is plotted in the upper part of Figure 5.15a (Horiguti et al., [5.17]), for a cascade with the stagger $\beta = 80$ deg and the chord-pitch ratio $C / h = 2.0$, typical for turbo-pump inducers. In this calculation, a periodicity over 4 blades is assumed and hence it corresponds to the case of a 4-bladed inducer. It is well known that alternate blade cavitation, in which the cavity length differs alternately, may occur for inducers with an even number of blades. The cavity lengths of alternate blade cavitation are shown in the upper part of Figure.5.15b. Alternate blade cavitation starts to develop when the cavity length, l_s, of equal cavitation exceeds 65% of the blade spacing, h.

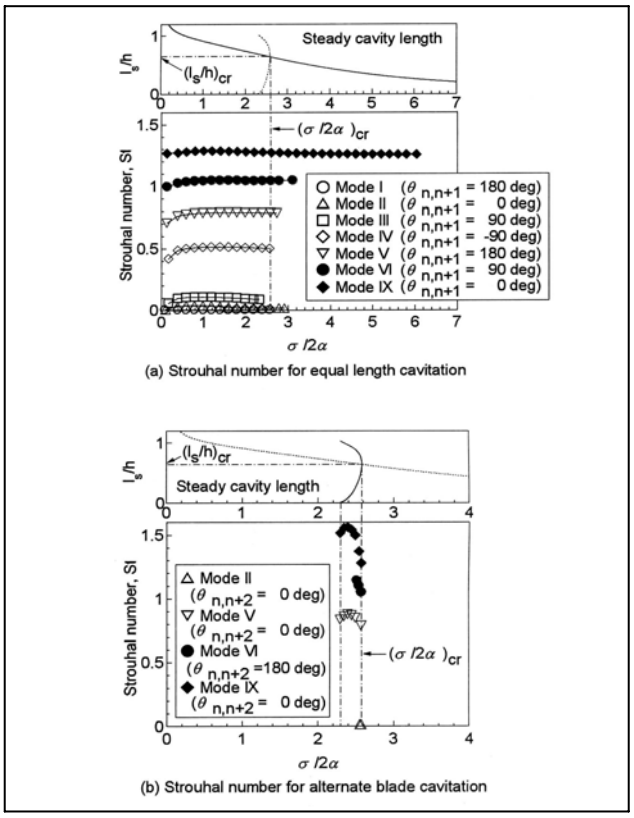

Figure 5.15: Steady cavity length (upper figures) and Strouhal number (lower figures) of various modes of cavitation instabilities, for a 4-bladed inducer with the solidity $C / h = 2.0$, stagger $\beta = 80^o$ and the inlet duct length $L / C = 1000$.

Figure 5.16 shows the flow field around alternate blade and equal length cavitations. Near the trailing edge of cavities, we can observe a region where the flow is inclined towards the suction surface. In this region the incidence angle to the neighbouring blade on the suction side is smaller. This region starts to interact with the leading edge of the next blade when the cavity length becomes about 65% of the blade spacing. If the cavity length on one blade becomes longer than 65% of the blade spacing, the incidence angle to the next blade on the suction side becomes smaller and hence the cavity length on the next blade will decrease. This is the mechanism of the development of alternate blade cavitation.

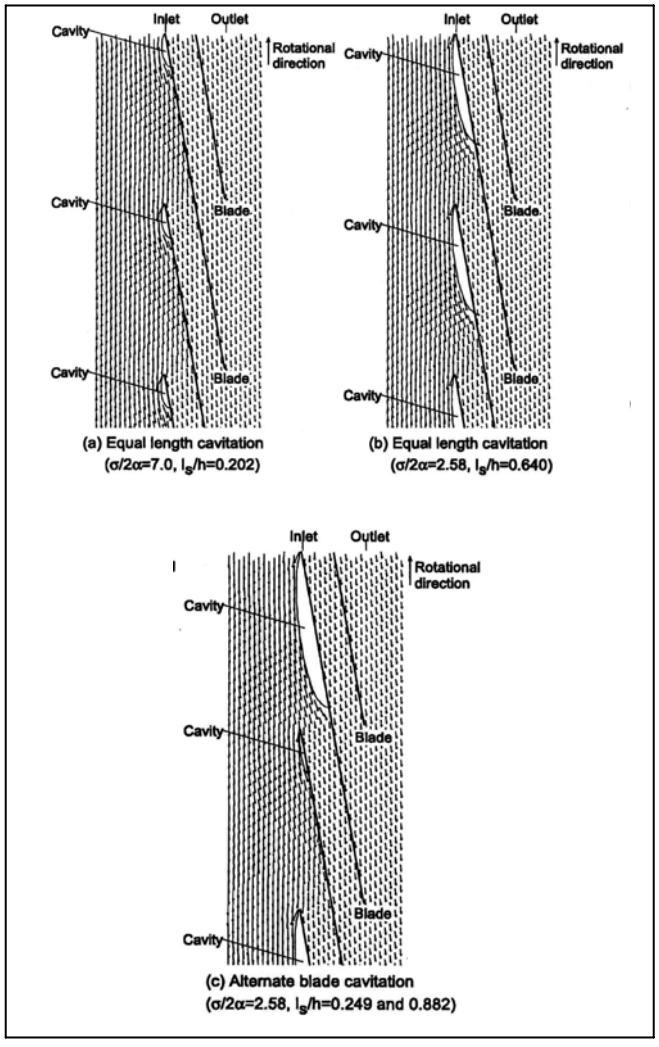

Figure 5.16: Alternate blade and equal cavitation in a cascade with the solidity $C / h = 2.0$, stagger $\beta = 80^o$ and the inlet duct length $L / C = 1000$. The incidence angle is $\alpha = 4^o$.

Strouhal numbers $St = \omega_R l_s / 2\pi U$ of various amplifying modes are shown in the lower part of Figure 5.15(a) and (b) for equal length cavitation and alternate blade cavitation. The symbol $\theta_{n,n+1}$ shows the phase advance of the disturbance on the upper blade (n+1) with respect to that on the lower blade (n) by one pitch, which is obtained as a result of the stability analysis. Here we focus on Mode I. For Mode I, the frequency is zero and the phase difference $\theta_{n,n+1}$ is 180 deg, corresponding to exponential transitions between equal and alternate blade cavitation. This mode appears for equal cavitation longer than 65% of the blade spacing, h, which shows that longer equal cavitation is statically unstable to a disturbance corresponding to the transition to alternate blade cavitation. Alternate blade cavitation does not have this mode and hence it is statically stable.

We now return to Figure 5.15(a). Mode II is a surge mode oscillation without interblade phase difference: $\theta_{n,n+1} = 0$. It was found that the frequency of this mode correlates with $1/\sqrt{L}$ where L is the length of the upstream conduit. So this mode represents normal cavitation surge. Mode II is system dependent while all other modes are system independent. Mode IX is also a surge mode oscillation with no interblade phase difference but has higher frequency. This mode is herein called "higher order surge mode oscillation". Figure 5.17 shows the shape of cavity oscillations for these modes. The cavity volume fluctuation of Mode IX is much smaller than that of conventional cavitation surge, Mode II. For this reason the frequency does not depend on the inlet conduit length. In addition, the frequency of this mode does not depend on the geometry of the cascade and this mode occurs also for single isolated hydrofoils (Watanabe et al. [5.18]). This mode starts to appear at much larger values of $\sigma/2\alpha$ than other modes.

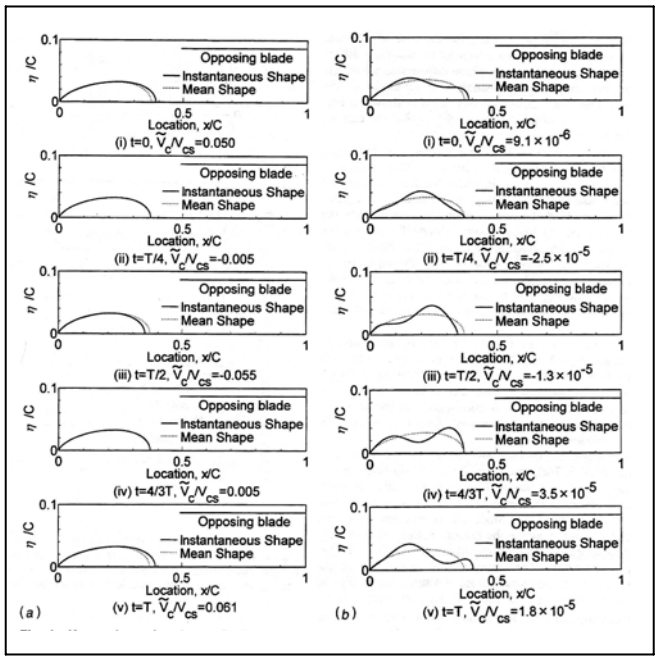

Figure 5.17: Oscillating cavity shape under (a) cavitation surge (Mode II) and (b) higher order surge mode oscillation (Mode IX). $\sigma/2\alpha = 2.0$ and $\alpha = 4.0^o$.

Modes III-VI are various modes of rotating cavitation with various interblade phase differences. Observed from a stationary frame, the disturbance of Mode III rotates around the rotor with an angular velocity higher than the impeller speed. This is conventional rotating cavitation. Mode IV represents one-cell rotating cavitation propagating in the opposite direction of the impeller rotation and is called "backward rotating cavitation". Mode V represents 2-cell rotating cavitation. Mode VI is one-cell forward rotating cavitation with a larger propagating speed than Mode III and this mode is called "higher-order rotating cavitation". All modes except for Mode IX start to occur when the cavity length exceeds 65% of the spacing. So, those modes might be caused by the interaction of the local flow near the cavity trailing edge with the leading edge of the opposing blade, as for alternate blade cavitation. Mode IX occurs for much shorter cavities and no physical explanation has been given so far.

By the two-dimensional stability analysis, various types of higher order modes are predicted in addition to cavitation surge, forward and backward propagating modes of rotating cavitation. These

higher order modes are experimentally observed less frequently compared to cavitation surge and forward rotating cavitation but they do occur (Tsujimoto et al., [5.19]). Since the frequencies of those higher order modes are high enough, resonance with blade bending mode vibration is possible (Tsujimoto et al., [5.20]). So, it is important to confirm that those instabilities are adequately suppressed by testing the inducer under all conditions encountered in real flight. It is also important to identify the reason why they occur in some cases and not in others.

Although the critical values of $\sigma/2\alpha$ do not agree with experiments, the critical value in terms of cavity length $l_s = 0.65h$ agrees with experiments reasonably if applied at the tip. The one-dimensional criterion $M > 2(1+\sigma_1)\phi K$ is satisfied under the condition $l_s = 0.65h$. So, the two-dimensional analysis gives more useful guideline for the prediction of cavitation instabilities although the one-dimensional criterion is more useful in considering the effects of various types of cavitation.

5.4 CAVITATION INSTABILITY CAUSED BY CHOKE

As treated in the preceding sections, most of cavitation instabilities occur in the range of cavitation number where head degradation due to cavitation is not significant. However, a cavitation instability caused by the head decrease due to cavitation has also been observed. This type of instability is treated in this section.

5.4.1 EXPERIMENTAL OBSERVATION OF ROTATING CHOIKE

During the firing test of the LE-7A LOX/LH2 engine of the HIIA rocket, a large amplitude rotor vibration of the fuel turbo-pump occurred at a frequency of about 350Hz which is about one-half of the shaft rotational speed Ω =700Hz. The vibration occurred when the pump inlet pressure was reduced. This vibration caused the failure of the bolts fastening the bearing cartridge. To investigate into this phenomenon, a series of tests was conducted at full speed with liquid hydrogen. The test results are reported by Shimura et al. [5.21].

Figure 5.18 shows the suction performance and the amplitude of the shaft vibration for two groups of flow rates around $Q/Q_d = 0.98$ and $Q/Q_d = 0.95$. For $Q/Q_d = 0.95$, the amplitude becomes larger at the cavitation number where the inducer head decreases rapidly.

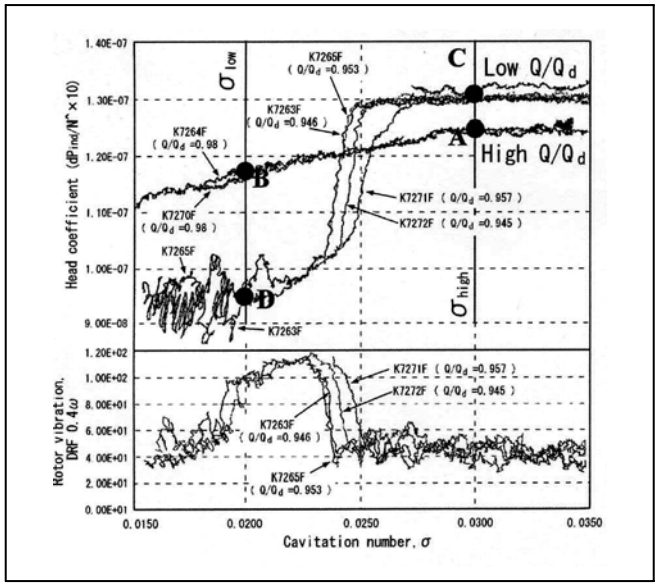

Figure 5.18: Suction performance and shaft vibration amplitude, with two groups of flow rate.

The head is kept nearly constant, above and below the cavitation number. The head decrease is not caused by the instability since the head decrease is not recovered at smaller cavitation number where the amplitude of vibration is smaller again. At a cavitation number higher than the breakdown cavitation number, σ_{high} , the head is larger for smaller flow rate and the performance curve has a negative slope in the flow rate vs. head plane. On the other hand, at a lower cavitation number than the breakdown, σ_{low}, the head is smaller for smaller flow rate and the performance curve has a positive slope. These relations are sketched in Figure 5.19. For compressors and fans, it is well known that the positive slope of the performance curve can cause surge and rotating stall at a smaller flow rate. Without cavitation, inducers with smaller blade angle from tangent never stall and the performance curve has positive slope for all flow rate.

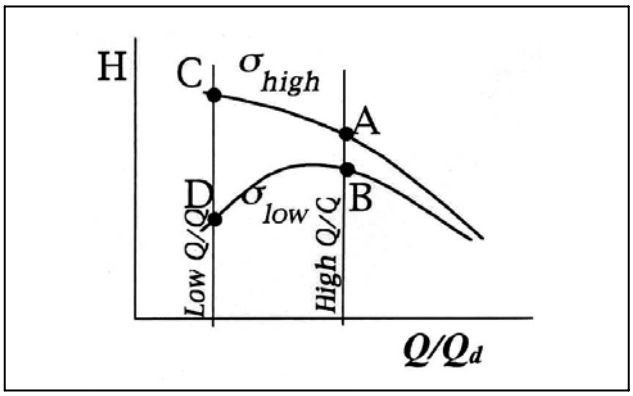

Figure 5.19: Sketch of head-flow rate curve at higher and lower cavitation number

On the other hand, the head starts to decrease when the cavity extends into the flow channel between blades. It was shown by Stripling and Acosta [5.22] that the head decrease due to cavitation can be explained by the mixing loss downstream of the cavity terminus. This is called "choke (by cavitation)". The cavity thickness is larger for smaller flow rate and hence the head decrease due to cavitation is larger, as sketched in Figure 5.20.

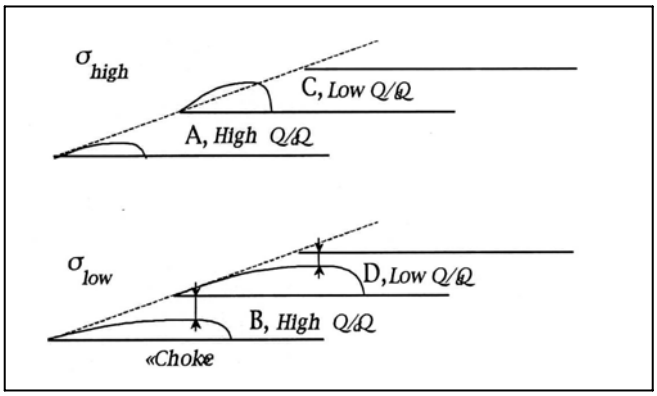

Figure 4.20: Sketch of cavity shape at higher and lower cavitation number.

If the head decrease due to cavitation associated with the reduction of flow rate is larger than the increase of Euler's head, the performance curve will have a positive slope. So, it is quite possible that the positive slope at smaller cavitation number is caused by the choke.

Figure 5.21 shows the spectrum of the inlet pressure fluctuation and the phase difference of the signals from two pressure transducers located apart by 144 degrees circumferentially (Shimura, et al., [5.21]). The rotational frequency of the impeller is 723Hz. The phase difference at the spectrum peak, 366Hz, is 147 degrees, which is close to the geometrical separation of 144 degrees.

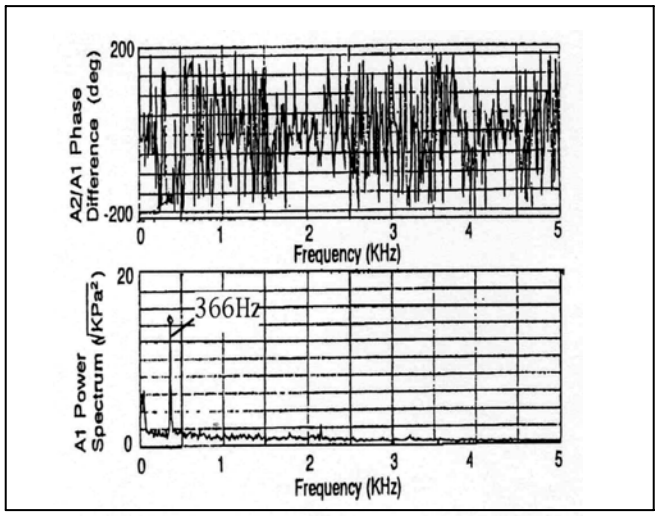

Figure 5.21: Spectrum of inlet pressure fluctuation and the phase difference between two pressure sensors.

This suggests that a disturbance with one cell is rotating around the rotor at 366Hz, with the rotational speed ratio 366/723=0.506. Since the head decrease due to cavitation is caused by choke, it is appropriate to call the instability "rotating choke". All reported cavitation instabilities occur in a range of cavitation number where degradation of performance due to cavitation is limited. So, this is a new type of cavitation instability caused by the positive slope of pressure performance due to cavitation choke. We should note here that the positive slope of suction performance has a stabilizing effect, as shown by Young et al. [5.8] for surge mode oscillation.

5.4.2 THEORETICAL ANALYSIS OF ROTATING CHOKE

Since the instability is associated with the head breakdown due to cavitation, the analytical model should be able to simulate the head breakdown. The closed cavity model cannot predict the head decrease due to cavitation and the results of stability analysis shown in Figure 5.7 does not include such instabilities associated with choke. To simulate rotating choke, a cavity model with a cavity wake is applied.

The viscous/inviscid interaction approach developed for cavitation-free flows is used.

According to this approach the flow is divided into an internal turbulent flow behind the cavity and an external inviscid flow in which the cavity is closed on the body of viscous layer displacement (Semenov et al., [5.23]). In the cavity wake three specific regions are considered as shown in Figure 5.22.

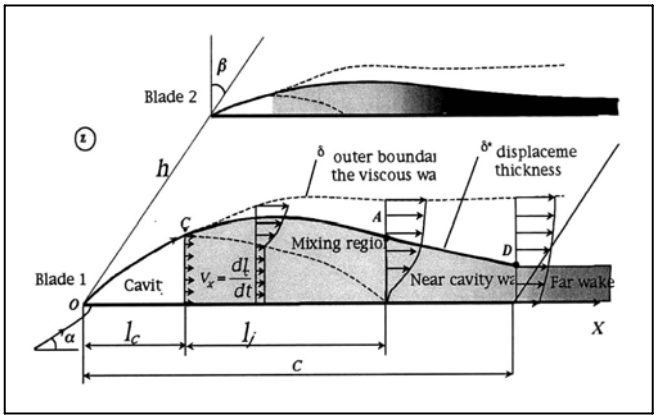

Figure 5.22: Waked cavity model

The first is the transitional mixing region where the velocity profile across the wake is under formation and the density changes smoothly due to flow re-circulation. This region is needed to provide a good agreement of suction performance with experiment (Semenov et al., [5.23]). The second is the near wake in which the velocity profile changes according to the external pressure gradient along the wake. Von Karman's integral equation is used and it is assumed that the coefficient of turbulent mixing is constant (Gogish et al., [5.24]). The third is the far wake, which starts from the trailing edge of blades and adjusts itself on the downstream flow. The conditions of interaction between viscous and inviscid flows in the near wake make it possible to find the shape of the boundary of the inviscid flow and to calculate both steady and unsteady flows. The normal velocity of the outer flow on the boundary is equated with that determined from the change of the wake thickness.

The head decrease due to cavitation is associated with the increase of relative velocity caused by the displacement effect of the cavity wake. The stability analysis [5.25] is similar to that with closed cavity model (Horiguchi et al., [5.17]) described in section 3. The problems for the inviscid and viscous flow are reduced to a system of linear equations by using linear interpolation of source and vortex and finite difference approximation of the ordinary differential equations for the viscous wake. The solution of the eigenvalue problem makes it possible to determine the frequencies and the stability of the various modes of cavitation instabilities.

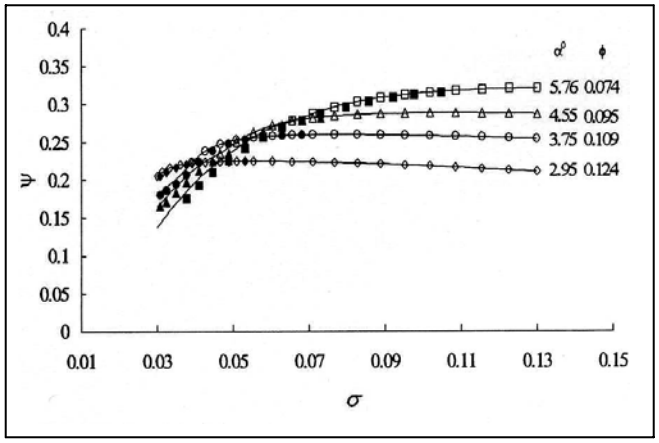

Figure 5.23: Suction performance predicted by the waked cavity model

Figure 5.23 shows the suction performance predicted by the model. On the suction performance curves, the occurrence of rotating cavitation is shown by open symbols, while the occurrence of rotating choke is shown by closed symbols. The present model also predicts other types of instabilities such as shown in Figure 5.7, but they are not shown here. We note that the rotating cavitation mainly occurs in the range where the performance degradation is insignificant, while rotating choke occurs where the head is decreased due to cavitation.

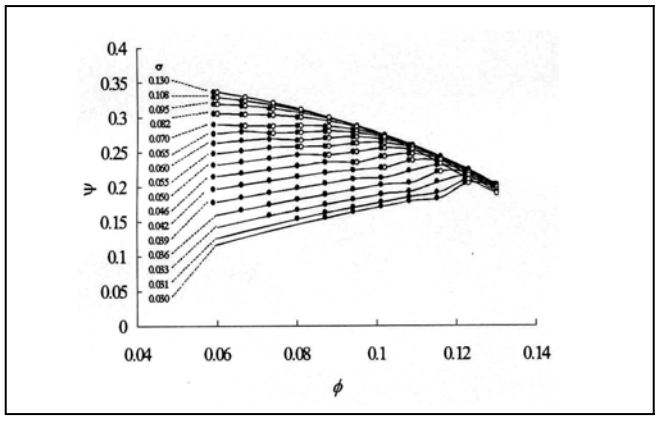

Figure 5.24: Head coefficient-flow coefficient curves for various cavitation numbers.

The performance curve in the flow coefficient vs. head plane is shown in Figure 5.24, where the occurrences of rotating cavitation and rotating choke are also shown by open and closed symbols, respectively. The same observations as with Figure 5.23 are also evident in this figure. Rotating choke occurs typically in the region with positive slope of the performance curve, which is quite different from rotating cavitation. This clearly shows that rotating choke is caused by the positive slope of the performance curve due to choke.

Figure 5.25 shows the propagation velocity ratio of rotating cavitation and rotating choke. Rotating choke is found only in a region with smaller σ. Rotating cavitation rotates faster than impeller but rotating choke rotates about a half of the impeller speed. Rotating stall in impellers with longer blade rotates with a speed only slightly smaller than the impeller speed, caused by the inertia effect of the fluids in the impeller (Tsujimoto, et al., [5.9], Tsujimoto et al., [5.13]). Lower speed of the rotating choke may be caused by the decrease of the inertia effect due to cavitation.

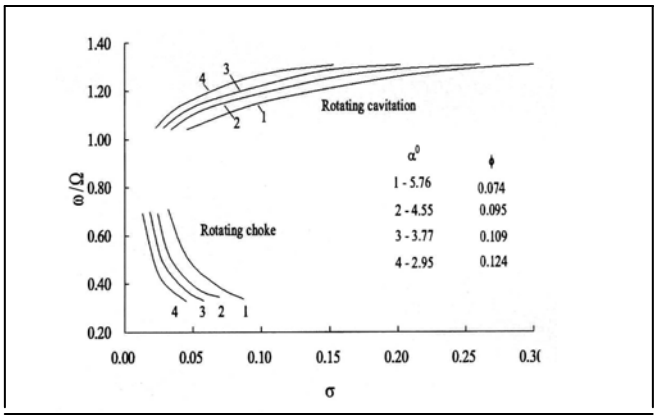

Figure 5.25: Propagation velocity ratio of rotating cavitation and rotating choke

Figure 5.26 shows the cavity shapes under rotating cavitation and rotating choke at their onset points (the largest cavitation number). For rotating choke the mixing region extends to the throat of the blade channel. On the other hand, rotating cavitation starts to occur with much shorter cavity. With a closed cavity model, it has been shown that various types of cavitation instability start to occur when the cavity length reaches about 65% of the spacing as mentioned in section 3.

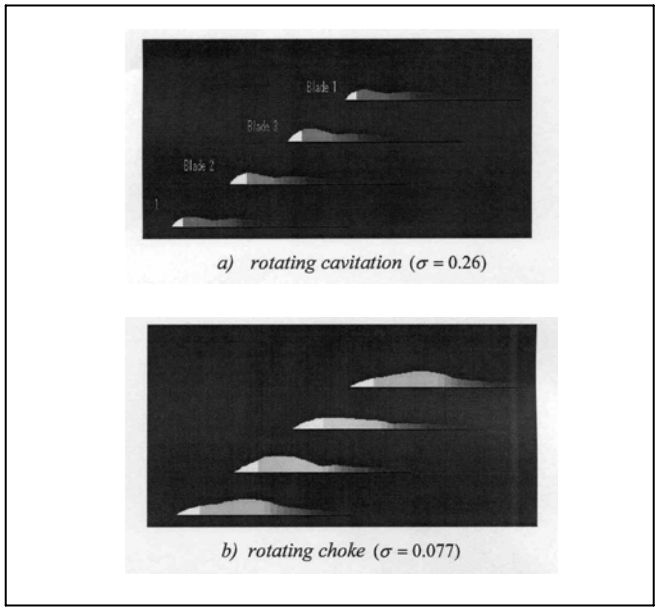

Figure 5.26: Cavity shapes at the onset point of rotating cavitation and rotating choke at $\phi = 0.095$ .Cavity is shown by the white area. The density in the mixing region and the wake is shown by the darkness. Vertical dimension is magnified with a factor 3.

Figure 5.27 shows the steady cavity length l_c of the closed cavity model and the total length of cavity and mixing region $l_c + l_m$ of the waked cavity model, normalized by the blade spacing h, plotted against $\sigma/(2\alpha)$.

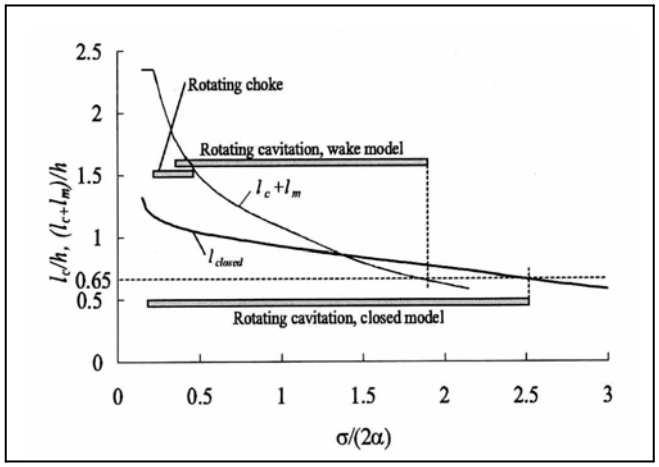

Figure 5.27 Cavity length of closed cavity model l_{closed}, and the total length of cavity and mixing region $l_c + l_m$ of the waked cavity model. The gray bars show the range of rotating cavitation and rotating choke. ($\beta = 80^o$, $C/h = 2.35$, $\alpha = 4^o$)

The regions of rotating cavitation and rotating choke occurrence are also shown. It is clearly shown that rotating cavitation starts to occur when the cavity length (closed cavity model) or the total length of cavity and mixing region (waked cavity model) exceeds 65% of the blade spacing, h. This suggests that the total length of cavity plus mixing region plays an important role in the present model. On the other hand, rotating choke starts to occur when the total length of cavity and mixing region exceeds 150% of the spacing. Thus, the present model can simulate two important characteristics of rotating choke, the onset condition and frequency. However, predicted suction performance shown in Figure 5.26 is significantly different from the experimental curve as shown in Figure 5.18. This may be caused by non-linear and/or three-dimensional effects. Positive slope and hence rotating choke are unusual and not observed for many inducers. Further research is needed for the complete understanding of rotating choke.

5.5 CONCLUSIONS

The one-dimensional stability analysis shows that the onset condition of cavitation surge and rotating cavitation can be represented by $M > 2(1+\sigma_1)\phi K$ and is independent on the pressure rise performance of the impeller. This shows that cavitation instabilities may occur at the design flow coefficient. The frequency of cavitation surge is proportional to the rotational frequency of the rotor. Rotating cavitation has a mode, which rotates faster than impeller rotation.

The two dimensional cavitating flow analysis using a closed cavity model shows that the cavitation instability depends on the steady cavity length l_s / h, or equivalently on $\sigma / 2\alpha$. Various modes of cavitation instabilities start to occur when the steady cavity length becomes larger than 65% of the blade spacing, caused by the interaction of the local flow near the cavity closure with the leading edge of the opposing blade. In addition to alternate blade cavitation, cavitation surge and rotating cavitation, and various higher order modes are predicted.

Rotating choke which occurs caused by the positive slope of the performance due to the blockage effect of cavitation could be predicted by using a waked cavity model. It starts to occur when the cavity-wake system extends into the blade passage, and the cavitating region rotates about 50% of the impeller speed.

Although real inducer flows are far more complicated with three-dimensional cavities such as tip leakage and backflow cavitation, the results of the two-dimensional flow stability analysis predicts cavitation instabilities surprisingly well if we apply them at the blade tip. However, in real engineering, the problem is to identify whether or not the predicted modes actually occurs or not under a certain geometry. To satisfy this requirement, we need to integrate the effects of the 3-D cavitations in the stability analysis.

ACKNOWLEDGMENTS

First of all, the author would like to express his sincere thanks to Professors Allan Acosta and Christopher Brennen, for their continued guidance and suggestions in conducting research. Professor Kenjiro Kamijo introduced the author to the interesting field and worked together with the author. Most of the results were obtained by Ph.D students at Osaka University, Professors Satoshi Watanabe and Hironori Horiguchi, and Dr. Akira Fujii. Dr.Yury Semenov at the National Space Agency of Ukraine and Dr.Yoshiki Yoshida at JAXA should also be acknowledged for their contributions.

In the last place, the author would like to thank Professor Shengcai Li, for offering the opportunity of introducing the interesting problems of cavitation instabilities in rocket turbo-pumps.

REFERENCES

[5.1] C.E. Brennen and A.J. Acosta. (1976). The Dynamic Transfer Function for a Cavitating Inducer. *ASME Journal of Fluids Engineering*, Vol.98, No.2, 182-191.

[5.2] C.E. Brennen. (1982). Bubbly Flow Model for the Dynamic Characteristics of Cavitating Pumps. *J. Fluid Mech.,* Vol.89, Part 2, 223-240.

[5.3] C.E. Brennen, C. Meissner, E.Y. Lo and G.S. Hoffmann. (1982). Scale Effects in the Dynamic Transfer Functions for Cavitating Inducers. *ASME Journal of Fluids Engineering*, Vol.104, No.4, 428-433.

[5.4] S. Rubin, S. (1966). Longitudinal Instability of Liquid Rockets Due to Propulsion Feedback (POGO), Journal of Spacecraft, Vol.3, No.8, pp.1188-1195

[5.5] W. Rosenmann, (1965). Experimental Investigations of Hydrodynamically Induced Shaft Forces With a Three Bladed Inducer. *Symposium on Cavitation in Fluid Machinery, ASME Winter Annual Meeting,* 172-195.

[5.6] K. Kamijo, T. Shimura and M. Watanabe. (1980). A Visual Observation of Cavitating Inducer Instability. *Technical Report of National Aerospace Laboratory*, TR-598T.

[5.7] B. Goirand, A.L. Mertz, F. Jousellin and C. Rebattet. (1992). Experimental Investigations of Radial Loads Induced by Partial Cavitation with a Liquid Hydrogen Inducer. *ImechE*, C453/056, 263-269.

[5.8] W.E. Young. (1972). Study of Cavitating Inducer Instabilities. *Final Report, NACA-CR- 123939*, 1972-8.

[5.9] Y. Tsujimoto, K. Kamijio and Y. Yoshida. (1993). A Theoretical Analysis of Rotating Cavitation in Inducers. *ASME Journal of Fluids Engineering*, Vol.115, No.1, 135-141.

[5.10] S.L. Ng and C.E. Brennen. (1978). Experiments on the Dynamic Behavior of Cavitating Pumps. *ASME Journal of Fluids Engineering*, Vol.100, No.2, 166-176.

[5.11] S. Rubin. (2004). An Interpretation of Transfer Function Data for a Cavitating Pump. *40th AIAA/ASME/SAE/ASEE Joint Propulsion Conference,* 11-14 July, Fort Launderdale, Florida, AIAA-2004-4025.

[5.12] S. Otsuka, Y. Tsujimoto, K. Kamijo and O. Furuya. (1996). Frequency Dependence of Mass Flow Gain Factor and Cavitation Compliance of Cavitating Inducers. *ASME Journal of Fluids Engineering*, Vol.118, No.2, 400-408.

[5.13] Y. Tsujimoto, K. Kamijo and C.E. Brennen. (2001). Unified Treatment of Cavitation Instabilities of Turbomachines. *AIAA Journal of Propulsion and Power*, Vol.17, No.3, 636-643.

[5.14] Y. Tsujimoto, Y. Yoshida, Y. Maekawa, S. Watanabe and T. Hashimoto. (1997). Observations of Oscillating Cavitation of an Inducer. *ASME Journal of Fluids Engineering*,Vol.119, No.4, December, 775-781.

[5.15] T. Hashimoto, M. Yoshida, K. Kamijyo and Y. Tsujimoto. (1997). Experimental Study on Rotating Cavitation of Rocket Propellant Pump Inducers. *AIAA Journal of Propulsion and Power*, Vol.13, No.4, 488-494.

[5.16] H. Horiguchi, S.Watanabe, Y. Tsujimoto and M. Aoki. (2000). Theoretical analysis of Alternate Blade Cavitation in Inducers. *ASME Journal of Fluids Engineering*, Vol.122, No.1, 156-163.

[5.17] H. Horiguchi, S. Watanabe and Y. Tsujimoto. (2000). A Linear Stability Analysis of Cavitation in a Finite Blade Count Impeller. *ASME Journal of Fluids Engineering*, Vol.122, No.4, 798-805.

[5.18] S.Watanabe, Y. Tsujimoto, J.P. Franc and J.M. Michel. (1998). Linear Analysis of Cavitation Instabilities. *Proc. Third International Symposium on Cavitation,* April, Grenoble, France, 347-352.

[5.19] Y. Tsujimoto, H. Horiguchi and A. Fujii. (2004). Non-Standard Cavitation Instabilities in Inducers. *Proceedings of the 10th International Symposium on Heat Transfer and Dynamics of Rotating Machinery*, March 7-11, Honolulu, Hawaii.

[5.20] Y. Tsujimoto and Y. Semenov. (2002). New Types of Cavitation Instabilities in Inducers. *Proceedings of the 4th International Symposium on Launcher Technology*, 3-6 December, Liege, Belgium.

[5.21] T. Shimura, M. Yoshida, K. Kamijo, M. Uchiumi, Y. Yasutomi. (2002). Cavitation Induced Vibration Caused by Rotating-stall-type Phenomenon in LH2 Turbopump. *Proceedings of the 9th of International Symposium on Transport Phenomena and Dynamics of Rotating Machinery*. Honolulu, Hawaii, February 10-14.

[5.22] L.B. Stripling and A.J. Acosta. (1962). Cavitation in Turbopump – Part 1. *ASME Journal of Fluids Engineering*, Vol.84, No.3, 326-338.

[5.23] Y. Semenov and Y. Tsujimoto. (2003). A Cavity Wake ModelBased on the Viscous/Inviscid Interaction Approach and Its Application to Nonsymmetric Cavity Flows in Inducers. *ASME Journal of Fluids Engineering*, Vol.125, No.5, 758-766.

[5.24] L.V. Gogish and G.Yu. Stepanov. (1979). *Turbulent Separated Flows* (in Russian), Moscow, Nauka.

[5.25] Y, Semenov, A. Fujii and Y. Tsujimoto. (2004). Rotating Choke in Cavitating Turbopump Inducer. *ASME Journal of Fluids Engineering*, Vol.126. No.1, 87-93.

Invited Lecture

6. CAVITATION FLOW COMPUTATION THROUGH HYDRAULIC FRANCIS TURBINES

Professor Wu Yulin, Zhang Liang & Liu Shuhong
Thermal Science & Power Engineering Key Laboratory of Ministry
of Education, Tsinghua University, China
wyl-dhh@tsinghua.edu.cn

ABSTRACT

In this paper, the mixture model which describes an homogeneous multiphase flow is adopted to simulate the cavitation flow through the entire flow passage of Francis turbine with the full cavitation model and the RNG $k-\varepsilon$ turbulence model. The simulation results of a prototype Francis turbine indicate the flow situation and bubble fraction distribution through the turbine. And the results of a model turbine are compared with test results and they agree well with each other.

NOMENCLATURE

C_e: Experience factor
C_c: Experience factor
D_1: Runner diameter
f: Mass factor
$\boldsymbol{g}$: Gravity vector
H: Head
k: Turbulent kinetic energy
M: Molecular weight of the gas
n: Bubble number in unit volume
p: Pressure
R: The pure phase change rate
R: General gas constant
r: Radius
T: Absolute temperature
t: Time
$\boldsymbol{V}$: Velocity vector
V: Velocity, volume
v: Velocity component
We: Webber number

Greek

α: Volume fraction, cavity fraction
σ: Tension of cavity
σ: Cavitation number of hydraulic machinery
ρ: Density
μ: Dynamic viscosity
ε: Turbulent kinetic energy dispassion rate
η: Efficiency
': Fluctuation

Subscripts

a: Atmospheric
B: Bubble
c: Condensation rate
ch: Characteristic velocity
e: Evaporation rate
g: Unsolved gas
l: Liquid
rel: Relative
sk: Suction
sat: Saturated vapor
t Turbulence
v: Vapor
VA: Vacuum

6.1 INTRODUCTION

In the field of hydraulic machinery, the study on cavitation phenomenon is very necessary because serial problems emerge with cavitation, such as the

change of operating characteristics, performance decrease, cavitation erosion, vibration, noise and so on. Concerning the cavitation experimental study, there are some difficulties existed due to its complexity. For example, the scale effect, which still needs further study, will affect the results of the model test for large unit. Therefore, the numerical simulation of cavitation flow is becoming more and more important.

In this paper, the mixture model, which describes a homogeneous multiphase flow, is adopted. The bubble phase and the water phase are considered to be at the balance of dynamics and diffuseness. The variable is the average one of the two phases according to their volume fraction. The full cavitation model is used for the mixture flow model computation of the cavitation two-phase flow. In the full cavitation model, most of the physics processes during cavitation are considered. The RNG (Renormalization Group) $k-\varepsilon$ turbulence model is used to simulate the separate flow and swirl flow better.

The simulation of the two-phase cavitating flow through both a prototype Francis turbine and a model Francis turbine have been carried out. The whole passage of the turbine is the computation domain and is filled with unstructured grids. The control equations are discreted by the finite volume method. The simulation is performed under serial running conditions.

According to the simulation results, the effect of cavitation on turbine performances can be considered and the cavitation region and degree under varied running condition can be observed. The conclusion drawn from the simulation results agrees with it from the experiment results. The mixture full cavitation model can be used to simulate cavitation flow in a water turbine and other fluid machinery.

Key words: 3D cavitation flow, mixture model, RNG $k-\varepsilon$ turbulence model, Francis turbine

6.2 THE MIXTURE MODEL OF TWO-PHASE CAVITATION FLOW WITH FULL CAVITATION MODEL

In this section, the cavity turbulent flow simulation is carried out by using the non-slip model of mixed fluid in multiphase flow. In this model, it is assumed that there is an equilibrium of the momentum and diffusion of two phases, they are, the liquid phase and bubble phase. At this equilibrium, the velocity of cavity equals to that of fluid flow at every position of the flow field.
In the cavity phase simulation, the Full Cavitation Model has been applied to consider the full process of the bubble development [6.1], in which production and collapsing of bubble, its transport, turbulence pressure and velocity fluctuation and unsolvable gas in water have been considered in the process of bubble.

6.2.1 FULL CAVITATION MODEL

The Rayleigh-Plesse equation (1) can be used to describe the bubble dynamic character when there is not slip between the liquid phase flow and bubble movement [6.2].

$$r_B\frac{\mathrm{D}^2 r_B}{\mathrm{D}t^2}+\frac{3}{2}\left(\frac{\mathrm{D}r_B}{\mathrm{D}t}\right)^2=\left(\frac{p_B-p}{\rho_l}\right)-\frac{4\nu_l}{r_B}\frac{\mathrm{D}r_B}{\mathrm{D}t}-\frac{2\sigma}{\rho_l r_B} \qquad (1)$$

where r_B is radius of bubble, p_B is pressure on bubble wall, ν_l the kinetic viscosity of fluid, ρ_l is the density of fluid and σ is the tension of bubble.
After introducing Eq. (1) then the continuity equation of the mixed flow of liquid phase and cavity phase is as follows:
For liquid phase

$$\frac{\partial}{\partial t}\left[(1-\alpha)\rho_l\right]+\nabla\cdot\left[(1-\alpha)\rho_l\boldsymbol{V}\right]=-R \qquad (2\text{-}1)$$

For cavity phase:

$$\frac{\partial}{\partial t}(\alpha\rho_v)+\nabla\cdot(\alpha\rho_v\boldsymbol{V})=R \qquad (2\text{-}2)$$

For mixed flow:

$$\frac{\partial}{\partial t}(\rho\ )+\nabla\cdot(\rho\boldsymbol{V})=0 \qquad (2\text{-}3)$$

Where $\alpha=\dfrac{V_v}{V_v+V_l}$ is cavity volume fraction, ρ is the density of mixed fluid and $\rho=\alpha\rho_v+(1-\alpha)\rho_l$, R is the pure phase change rate and $R=R_e-R_c$, and where R_e is evaporation rate and R_c condensation rate of bubble. Then Eq. (2-3) has the following form:

$$\frac{\mathrm{D}\rho}{\mathrm{D}t} = -(\rho_l - \rho_v)\frac{\mathrm{D}\alpha}{\mathrm{D}t} \tag{3-1}$$

where $\alpha = n\frac{4}{3}\pi r_B^3$ and n is the number of bubble in a unit volume, and

$$\frac{\mathrm{D}\rho}{\mathrm{D}t} = -(\rho_l - \rho_v)(n4\pi)^{1/3}(3\alpha)^{2/3}\frac{\mathrm{D}r_B}{\mathrm{D}t} \tag{3-2}$$

By using the Rayleigh-Plesset equation and considering Eq. (3), then the pure phase changing rate can be obtained as:

$$R = (n4\pi)^{1/3}(3\alpha)^{2/3}\frac{\rho_v\rho_l}{\rho}\left[\frac{2}{3}\left(\frac{p_B - p}{\rho_l}\right) - \frac{2}{3}r_B\frac{\mathrm{D}^2 r_B}{\mathrm{D}t^2}\right]^{1/2} \tag{4}$$

Introducing the relation between the cavity mass fraction f and α, $\alpha = f\frac{\rho}{\rho_v}$, and neglecting the second order term, the cavity phase mass transporting equation has the following form:

$$\frac{\partial}{\partial t}(\rho f) + \nabla\cdot(\rho f\boldsymbol{V}) = (n4\pi)^{1/3}(3\alpha)^{2/3}\frac{\rho_v\rho_l}{\rho}\left[\frac{2}{3}\left(\frac{p_B - p}{\rho_l}\right)\right]^{1/2} \tag{5}$$

where the right hand term is vapor production when the vapor wall pressure p_B is higher than local pressure p, that is, $p_B > p$, The cavity condensation is also expressed by using the similar equation, when $p_B < p$. When assuming $p_B = p_v$, Eq. (5) is also called as the cavity dynamic character equation.

6.2.2 PHASE CHANGING RATE

The phase changing rate r_B can be rewritten in the following form to replace *n* in Eq. (5):

$$r_B = \frac{3\alpha}{r_B}\frac{\rho_v\rho_l}{\rho}\left[\frac{2}{3}\frac{p_v - p}{\rho_l}\right]^{1/2} \tag{6-1}$$

Or in the following experience formulae:

$$r_B = \frac{0.061We\sigma}{\rho_l V_{rel}^2} \tag{6-2}$$

where V_{rel} is relative velocity between liquid phase and cavity phase. For cavity flow, V_{rel} is small, considering $r_B \to 0, \alpha \to 0$ and phase changing rate *R* at a unit volume is direct ratio to the volume fraction of the corresponding phase, *We* is Webber number.. The evaporation rate R_e and the condensation rate R_c can be expressed by the mass fraction f:

$$R_e = \mathrm{C_e}\frac{V_{ch}}{\sigma}\rho_l\rho_v\left[\frac{2}{3}\frac{p_v - p}{\rho_l}\right]^{1/2}(1-f) \tag{6-3}$$

$$R_c = \mathrm{C_c}\frac{V_{ch}}{\sigma}\rho_l\rho_l\left[\frac{2}{3}\frac{p - p_v}{\rho_l}\right]^{1/2} f \tag{6-4}$$

where $\mathrm{C_e}$, $\mathrm{C_c}$ are experience factors. V_{ch} is characteristic velocity, which is also the relative velocity between two phase, and only is 1～10% of the liquid velocity and is expressed by $\sqrt{k}$, because it has the same order as the turbulent velocity.

6.2.3 EFFLUENCE OF TURBULENCE

Singhal et al proposed the PDF (probability density function) model [6.3] to consider the influence of turbulence to the cavity flow:

$$p_t' = 0.39\rho k \tag{7-1}$$

And this effect can be simplified as:

$$p_v = p_{sat} + p_t'/2 \tag{7-2}$$

where p_{sat} is saturated vapor pressure.

6.2.4 EFFLUENCE OF UNSOLVABLE GAS

If the non-dissolvable gas is only 1ppm (1e-6) in volume, it also effects to cavitation. Assuming the mass factor of non-dissolvable gas to be f_g, then the mixed flow density is as follows:

$$\frac{1}{\rho} = \frac{f_v}{\rho_v} + \frac{f_g}{\rho_g} + \frac{1 - f_v - f_g}{\rho_l} \tag{8-1}$$

where ρ_g is the density of non-dissolvable gas, so that

$$\rho_g = \frac{Mp}{RT} \tag{8-2}$$

where M is molecular weight of the gas, and general gas constant is $R = 8314\ \mathrm{J/(kg\times mol\times K)}$. And the volumetric fractions of the gas and liquid are as

$$\alpha_g = f_g\frac{\rho}{\rho_g}, \quad \alpha_l = 1 - \alpha_v - \alpha_g \tag{8-3}$$

The evaporation rate and condensation rate are as follows:

$$R_e = \mathrm{C_e}\frac{\sqrt{k}}{\sigma}\rho_l\rho_v\left[\frac{2}{3}\frac{p_v - p}{\rho_l}\right]^{1/2}(1 - f_v - f_g) \tag{9-1}$$

$$R_c = \mathrm{C_c}\frac{\sqrt{k}}{\sigma}\rho_l\rho_l\left[\frac{2}{3}\frac{p - p_v}{\rho_l}\right]^{1/2} f_v \tag{9-2}$$

where the factors $\mathrm{C_e}$ and $\mathrm{C_e}$ are 0.02，0.01.

6.3 GOVERNING EQUATIONS OF CAVITY FLOW

Introducing the foregoing full cavitation model, the governing equations of the cavity flow are as follows.

6.3.1 CONTINITY EQUATIONS

Mixed fluid phase:

$$\frac{\partial}{\partial t}(\rho\ )+\nabla\cdot(\rho\boldsymbol{V})=0 \qquad (10\text{-}1)$$

Vapor cavity phase:

$$\frac{\partial}{\partial t}(\rho f_v)+\nabla\cdot(\rho f_v\boldsymbol{V})=R_e-R_c \qquad (10\text{-}2)$$

6.3.2 MOMENTUM EQUATIONS

Mixed fluid phase:

$$\frac{\partial(\rho\boldsymbol{V})}{\partial t}+\nabla\cdot(\rho\boldsymbol{V}\boldsymbol{V})=-\nabla p+\frac{1}{3}\nabla\left[(\mu+\mu_t)\nabla\cdot\boldsymbol{V}\right]+\nabla\cdot\left[(\mu+\mu_t)\nabla\boldsymbol{V}\right]+\rho\boldsymbol{g} \qquad (10\text{-}3)$$

6.3.3 TURBULENCE MODEL

The RNG (Renormalization Group) $k-\varepsilon$ turbulence model is also used for the mixed fluid phase turbulent simulation.

6.4 PREDICTION OF CAVITY FLOW THROUGH A PROTOTYPE FRANCIS TURBINE

In this section, calculated results of a prototype Francis turbine will be presented by using the cavity flow model in sec. 2.1 and the entire passage simulation of the turbine, from the spiral casing inlet, and then through the whole spiral casing, the stay vanes, guide vanes, the whole runner flow passage and draft tube to the outlet of draft tube.

6.4.1 PARAMETERS AND OPERATIONAL CONDITIONS OF THE FRANCIS TURBINE

Table 1 shows the parameters of Francis turbine in which the cavity flow has been calculated. The calculated domain is the same as shown in Figure 6.1, but it is a prototype Francis turbine with a runner of 9.8 m diameter.

Parameter	Date	Parameter	Date
Rated head	85.6 m	Rated power	767 MW
Flow rate	1000.- m^3/s	Rotating speed	71.4 r/min
Specific speed	239.1 m.kW	Runner Diameter	D_1=9.8 m
Blade number	15	Vane number	23

Table 6.1: parameters of Francis turbine

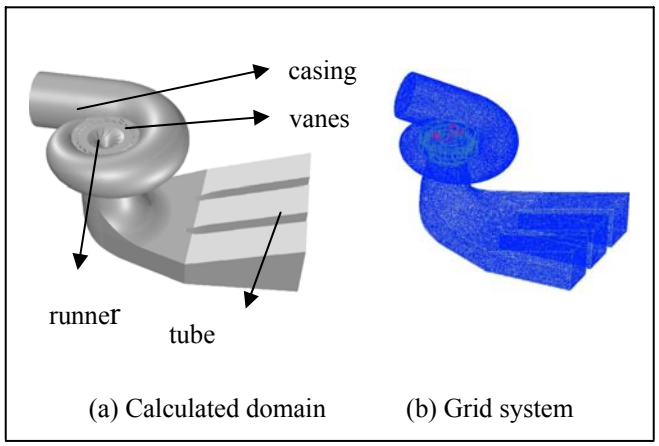

(a) Calculated domain (b) Grid system

Figure 6.1: The model hydraulic turbine

The calculation conditions are at the rated head of 85.6 m and at the guide vane opening $a_0=20^\circ$ $a_0=27^\circ$ and $a_0=30^\circ$ respectively.

Through changing the downstream water level of the turbine, the cavitation number σ of the model turbine in experiment will be modified as:

$$\sigma=\frac{H_a-H_{VA}-H_{SK}-H_v}{H} \qquad (11\text{-}1)$$

where $H_{VA}=p_{VA}/\rho g$ is the vacuum pressure the draft tube for experiment, $H_a=p_a/\rho g$ is the head of atmospheric pressure, H_{SK} is the suction head, H is tested head, $H_v=p_v/\rho g$ is the cavitation pressure head. For the prototype turbine at the site, $H_{VA}=0$, Eq. (11-1) will be as

$$\sigma=\frac{H_a-H_{SK}-H_v}{H} \qquad (11\text{-}2)$$

Four cavitation number can be chosen for the present calculation, they are σ = 0.046, 0.057, 0.069 and 0.081 respectively.

6.4.2 CALCULATED RESULTS OF THE PROTOTYPE TURBINE

According to the foregoing explanation, it is assumed that p_v = 3540Pa, f_g = 15ppm, $\rho_l=1000\text{kg/m}^3$, $\rho_v=0.02558\text{kg/m}^3$ and the water tension $\sigma=0.0717\text{ N/m}$. And the calculation conditions are H =85.6m, $a_0=20^\circ$ and cavitation number σ =0.05. Fig. 2 shows the pressure (p) contour and the cavity fraction (α) contours in Francis turbine runner (a), and on the pressure surface (b) and suction surface (c) of runner blade respectively. From Figure 6.2, it is indicated that near the outlet

of the runner blade, especially, on the suction surface and near the band the cavity fraction is higher, at near the inlet of draft tube it approximates to 1. In the low cavity fraction area, the pressure is low and nearly to 3540Pa, but this is not always true. Because in some area with high cavity fraction, the pressure is higher than 3540Pa.

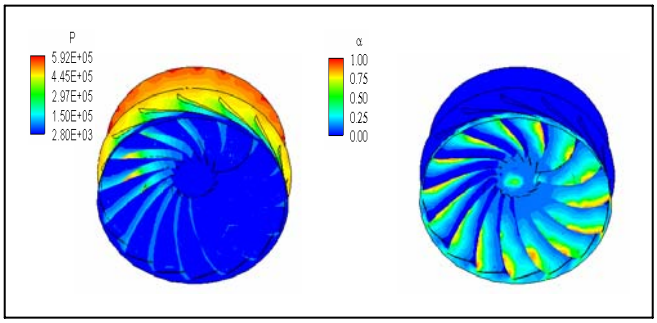

Figure 6.2a: Pressure (p) and cavity fraction (α) contours of runner

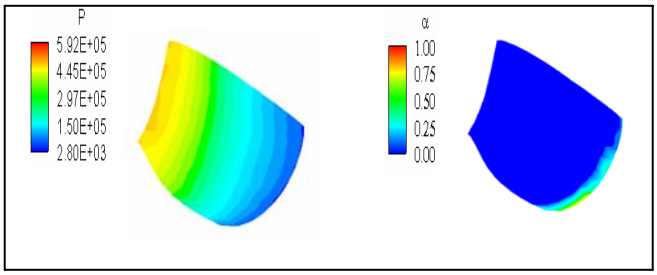

Figure 6.2b: Pressure (p) and cavity fraction (α) contours on pressure side of blade

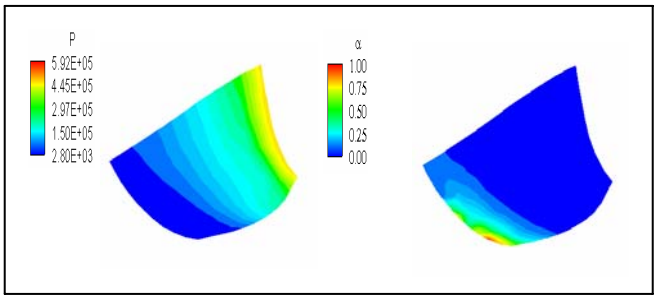

Figure 6.2c: Pressure (p) and cavity fraction (α) contours on suction side of blade

Figure 6.3 shows the pressure (p) contour and cavity fraction (α) contour at inlet and in conical part of draft tube. There is a rotating vortex rope with cavity in draft tube. And at the center of the rope the cavity fraction is nearly 1 and this cavity is extending into the conical part of the tube.

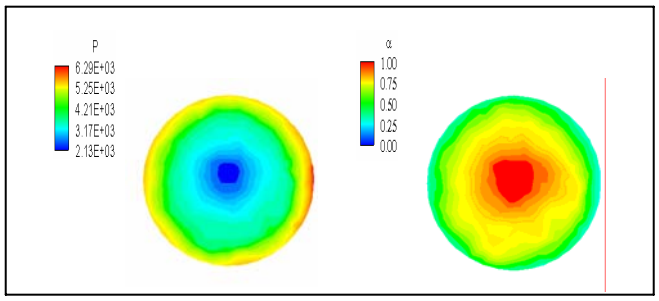

Figure 6.3a: Pressure (P) and cavity fraction (α) contours at inlet of draft tube

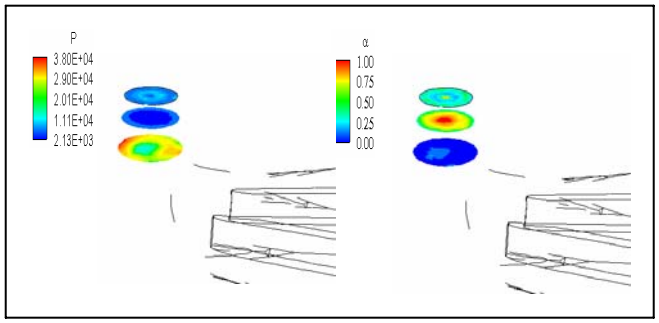

Figure 6.3b: Pressure (p) and cavity fraction (α) contours in conical part of draft tube

Figure 6.4 indicates the comparison of cavity fraction (α = 0.5) contour in runner at different cavitation number (σ) conditions. At the border of cavity in this figures, the cavity fraction α = 0.5. With decrease of cavitation number σ, the cavity area is getting larger and larger. When σ = 0.08, there is not any area of cavity. At the critical cavitation number σ = 0.08, the area of cavity has appeared.

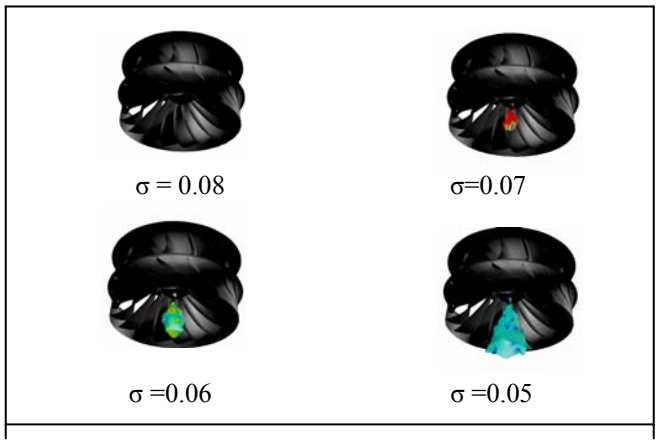

Figure 6.4: Cavity fraction (α = 0.5) contour in runner at different cavitation number (σ)

From calculated results, it is seen that the present model of two-phase cavity flow can be used to simulate the cavitation in hydraulic turbine and to predict the cavitation characters of turbine. Further development of the model and the simulation to unsteady analysis, the unsteady cavity flow model can be used to predict the pressure fluctuation induced by the cavity flow in hydraulic turbine and pump.

6.5 PREDICTION OF CAVITY FLOW THROUGH A MODEL FRANCIS TURBINE

The three dimensional cavitation two-phase turbulent flow through a model Francis turbine was also carried out by using the mixture model of multi-phase flows with the full cavitation model for modeling the bubble phase occurrence, development and collapse process, and as well as with the RNG turbulence model of the mixture.

6.5.1 PARAMETERS AND OPERATIONAL CONDITIONS OF THE FRANCIS TURBINE

The calculated results of cavitation turbulent flow through a model Francis turbine will be presented as same as that in section 4. The computation domain is also the entire flow passage of the model turbine, from the spiral casing inlet to the outlet of draft tube as shown as in Figure 6.5 and the model turbine parameters are listed in Table 6.2.

Parameter	Date
Runner diameter	D_1=0.35m
Blade number of runner	Z_B=13
Covering angle of spiral casing	Φ=345°
Number of guide vanes	Z_0=24
Height of guide vanes	B_0=0.304D_1
Distributing diameter of guide vanes	D_0=1.174D_1
Height of draft tube	H_0=3.01D_1
Height of draft tube	L=4.51D_1
Type of draft tube	Elbow likeness with double frusta

Table 6.2: Parameters of a model Francis turbine

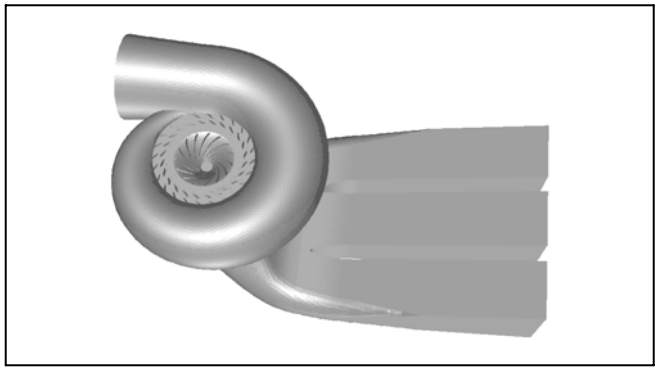

Figure 6.5: Francis turbine model

6.5.2 CALCULATED RESULTS OF THE MODEL FRANCIS TURBINE

According to China standard (GB/T 15613-1995) the testing method for the cavitation number σ in the model hydraulic turbine is as follows: Decreasing the pressure at the outlet of draft tube continuously while keeping the head constant of the turbine, recording variation of turbine efficiency with changing of cavitation number (factor), and the critical cavitation number σ_c can be defined as (1) when the efficiency drops down in 1% , or (2) the cavitation number, which has the value at the intersection point of the tangent of the efficiency curve and the prolongation of straight line part of the efficiency shown in Figure 6.6 and Figure6.7. The second method is adopted in this paper calculation.

The operation condition of the model turbine is at its unit speed n_{11}＝76.06r/min, and its guide vane opening a_0 =21.40 mm in the process of the calculation. As same as the test process, in the calculation, controlling the decrease of outlet pressure of the draft tube gradually, and recording the turbine efficiency (as shown in Table 6.3), then the curve $\sigma-\eta$ of the efficiency variation (at the ordinate in Figure 6.6) with the cavitation number, (at the abscissa in Figure 6.6) can be got as shown in Figure 6.6. In the curve $\sigma-\eta$, the foregoing intersection point can be found, and the critical cavitation number can be determined at this operation condition. Figure 6.7 shows the test results of the cavitation number experiment. Comparison between Fig. 6 calculated data and Figure 6.7 tested result of critical cavitation number

σ_c, the calculated date of σ_c is larger than the test one in 0.5%. But it is shown that the effect of cavitation to the turbine efficiency is same both in the calculation and in the experiment.

Pressure at outlet of draft tube p_{out} (Pa)	Cavitation number σ	Efficiency of turbine η (%)
107378.8	0.50	94.0
68178.8	0.30	94.0
48578.8	0.20	94.0
28978.8	0.10	93.9
25058.8	0.08	93.7
21138.8	0.06	93.0
19178.8	0.05	92.1
17218.8	0.04	91.2

Table 6.3 Relation of cavitation number and efficiency (calculation)

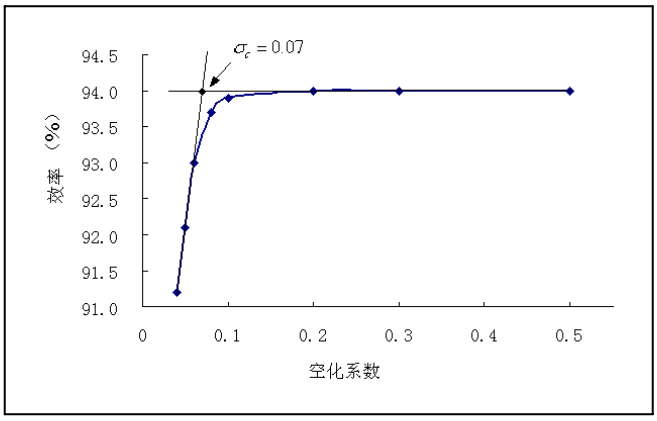

Figure 6.6: Calculated critical cavitation number, σ_c

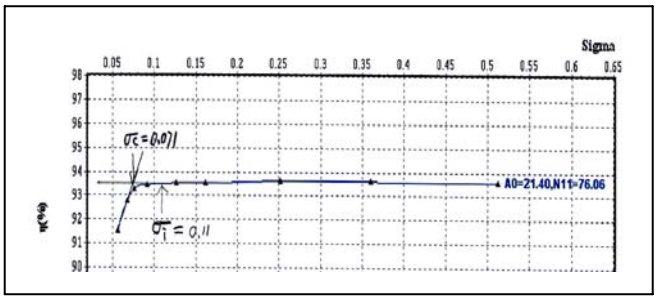

Figure 6.7: Experimental critical cavitation number, σ_c

Figure 6.8 shows cavity fraction distributions of computational results in the model turbine runner at different cavitation number conditions. Among them, Figure 6.8 (a) shows the cavity fraction in the model runner at cavitation number, σ =0.3, condition, and indicates that there is no any distinct bubble in the runner, as well as that the pressure and flow distributions are smooth at the condition, which is no-cavity operation condition. Figure 6.8 (b) shows the cavity fraction distribution in the runner at cavitation number, σ =0.1, condition, which is part-cavity operation condition in the runner, where there are some obvious bubbles on the suction side of blade outlet, but there is not any cavity vortex rope near the runner discharge cone and at the inlet of draft tube. Figure 6.8 (c) indicates the cavity fraction distribution in the runner at cavitation number, σ =0.05, condition, which is severe cavity operation condition in the runner. There are some obvious bubbles in large range on suction sides and outlet of blade. And there is pear-shape cavity vortex rope near the runner discharge cone and at the inlet of draft tube. The existence of vortex rope will cause efficiency decrease of the turbine and instability operation of the turbine unit.

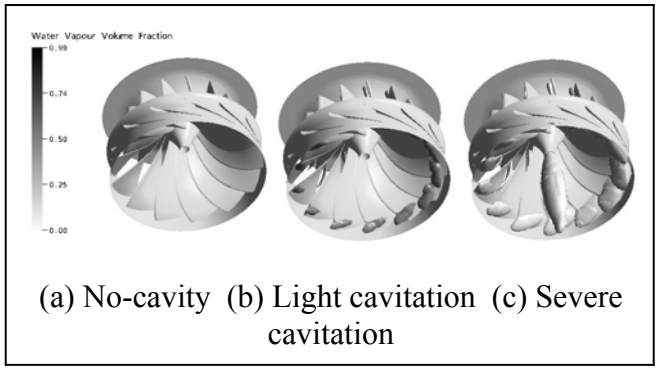

(a) No-cavity (b) Light cavitation (c) Severe cavitation

Figure 6.8: Cavity fraction distribution

When Francis turbines operate at off-design conditions, the flow will attack runner blades at their leading edges, and flow separation will occur on leading parts of blades, and also there will exist circulation flows at the outlet of runner. That will result in the vortex rope in draft tube and will cause the large pressure fluctuation at the inlet area of draft tube. At small load off-design condition, the circulation and the vortex rope at the inlet of draft tube has the same rotation direction as the direction of runner, the vortex rope has the screwy shape swinging in the tube as shown in Figure 6.9. And

larger load off-design condition than the optimum condition, the circulation and the vortex rope has the opposite rotation direction to the direction of runner, the vortex rope has large bubble-shape expanding or contracting in the tube as shown in Figure 6.10. In the present computation, the vortex ropes are simulated at both off-design conditions，as shown in Figure 6.11 and Figure 6.12 and compared well to the test results in Figures 6.9 and 6.10.

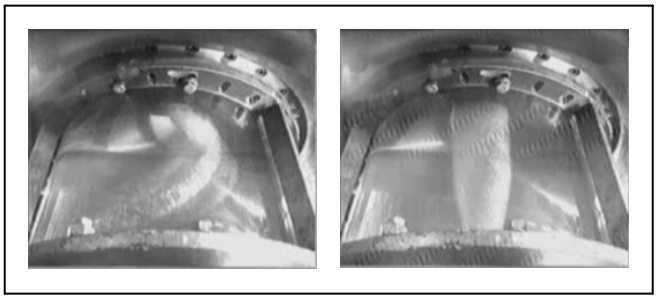

Figure 6.9 Test Vortex rope at small flow rate

Figure 6.10 Test Vortex rope at large flow rate

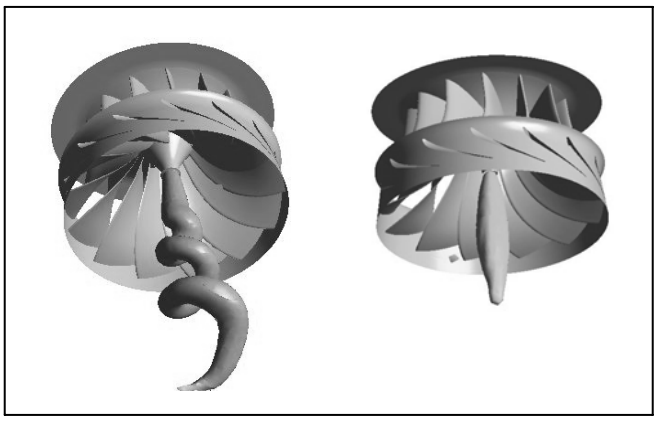

Figure 6.11 Calculated vortex rope at small flow rate

Figure 6.12 Calculated vortex rope at large flow rate

6.6 CONCLUSIONS

The cavitation flow has been simulated based on the mixture model of the cavity two-phase flow and RNG $k-\varepsilon$ turbulence model, as well as with the full cavitation model.

The calculated results of model Francis turbine have been compared with the test results in critical cavitation number, σ_c, and vortex ropes, which are agreed well with each other.

The simulated results of prototype Francis turbine have indicated cavitation bubble distributions in the turbine.

ACKNOWLEDGMENTS

This research work is supported by the Key project of the National Foundation of Natural Sciences in China (Project number: 90410019).

REFERENCES

[6.1] A.K. Singhal, H.Y. Li, M.M. Athavale and Y. Jiang. 2001. Mathematical Basis and Validation of the Full Cavitation Model. ASME FEDSM'01, New Orleans, Louisiana.

[6.2] C.E. Brennen. 1995. Cavitation and Bubble Dynamics. Oxford: Oxford University Press.

[6.3] A.K. Singhal, N. Vaidya and A.D. Leonard. 1997. Multi-Dimensional Simulation of Cavitating Flows Using a PDF Model for Phase Change. ASME FED Meeting, Paper No. FEDSM'97-3272, Vancouver, Canada.

Invited Lecture

7. CAVITATION DETECTION IN HYDRAULIC TURBINES USING ON-BOARD VIBRATION

Professor E. Egusquiza
CDIF Centre for Industrial Diagnostics Technical University of Catalonia, Barcelona
egusquiza@mf.upc.edu

This text of this lecture was not available by the print deadline. For further information please contact Professor Eduard Egusquiza.

WIMRC FORUM 2006

Cavitation in Turbo-machinery & In Medical Applications

International Manufacturing Centre
The University of Warwick
Coventry, CV4 7AL, UK

3rd July 2006

Editor
Professor S.C. Li

Assistant Editor
Miss N.A. Wensley

http://go.warwick.ac.uk/wimrc/

The 1st International Conference on Hydropower Technology & Key Equipment 2006
27-29 Oct 2006 Beijing

CHALLENGE TO MODERN TURBINE TECHNOLOGIES
Analysis of Damage to Guide Vane Surface of Three Gorge Turbines

S.C. Li
Fluid Dynamics Research Centre, Warwick University
Coventry CV4 7AL, UK
S.Li@warwick.ac.uk

ABSTRACT

The Francis turbines (710 MW) of the Three Gorge Project are the world largest and even larger ones (1000MW) are to be developed for schemes on the upstream of the Yangtze River in China. The 14 units installed in the left-powerhouse have been all commissioned successfully during the period from June 2003 to September 2005, functioning as expected. However, all these turbines supplied by world leading manufacturers have developed a pattern of damage mainly on the guide-vanes, which is virtually span-wise dependent stream-wise strips. This type of damage has never been reported before. Is it an isolated issue or a fundamental phenomenon/challenge to huge turbines? Brief description of the damage is presented, together with analysis of possible causes. The preliminary study suggests that this is a phenomenon not fully understood yet, and it is a type of cavitation erosion induced by boundary layer turbulent spots. In other words, the turbulent spots serve as the cavitation inception points causing damage and then the damaged spots subsequently induce further cavitation and damage downstream. Thus a dynamic process forms producing these damage strips. According to the multidisciplinary nature of the phenomenon, the discussion presented in this article is developed from a wide view angle of metallurgical science as well as cavitation inception in boundary layer. It is emphasized that this is a new challenge to huge turbines. Further studies on both the fundamental mechanism of the damage and the novel turbine-design are essential for developing huge turbine.

1. INTRODUCTION

The turbines developed for the Three Gorge Project are the world largest Francis turbines in terms of their power (710 MW) and geometric dimensions (9800 mm of runner diameter). The 14 units installed in the left-powerhouse have been all commissioned successfully during the period from June 2003 to September 2005, generating electricity normally.

The damage was firstly found on the Number 11 turbine ('11F' will be used in the article, following the abbreviation employed at the Three Gorge Power Station) incidentally on 14th October 2005 (operated for 10,245.78 hours) when examining/repairing the damaged guide plate[1]. Later on similar damages were found on 10F on 27th December 2005 (11924.55 hours), on 9F on 11th December 2005 (2328.41 hours) and other units (e.g. 5F and 6F etc). The 14 machines in the left-powerhouse are supplied by two consortiums (Alstom + HEC, GE + Voith Siemens + DFEM) [31].

The significance of the Three Gorge Project itself is obvious in terms of technology development, economic-social-environmental effects. Further 12 similar turbines, in the right-powerhouse are being installed, and 6 additional similar machines in the underground-powerhouse will be purchased soon. Other hydro projects employing similar scale turbines are being developed by the China Yangtze Three Gorge Project Development Cooperation (CTGPC). For example, 18 turbines of 770 MW each for Xiluodu Project and 8 turbines of 750 MW each for Xiangjiaba are to be purchased late this year; 18 turbines of 825 MW each for Baihetan project and 10 units of 700 MW each for Wudongde project are at the feasibility study stage, total about 90 turbines. It is also under consideration to develop 1,000 MW turbine-generator units for hydro schemes. Under such a strategy for hydropower development, these damages, although their impact on the machine operation is

[1] A device employed on turbines for the first time. It will be discussed later.

insignificant[2], does catch the great attention from the top management team of CTGPC, and needs to be thoroughly investigated.

Questions immediately arise: (1) Is this a new phenomenon happened particularly to extremely large turbines? (2) Should new technologies be sought & developed for combating this problem? A special meeting was thus held at the Three Gorge site from 12 to 14 March 2006, attended by research engineers, university academics and manufacturer representatives. A few days later (19th March 2006), the author inspected the damages on 11F unit, in particular the damage on the representative No 4 guide vane. As an initial report of the *in situ* inspection, this article is thus also presented to the 1st International Conference on Hydropower Technology & Key Equipment 2006 for promoting further research in this direction. The outcome would benefit not only the power industry but also the advance of scientific knowledge in general.

2. BASIC INFORMATION

The powerhouse is shown by the model in Figure 1, and the specifications of the 11F turbine are as follows:

- Rated power 710 MW
- Max efficiency guaranteed, 96.26%
- Rated head 80.6 m
- Min head 61.0 m
- Max head 113.0 m
- Rated speed 75 rpm
- Run away speed <150 rpm

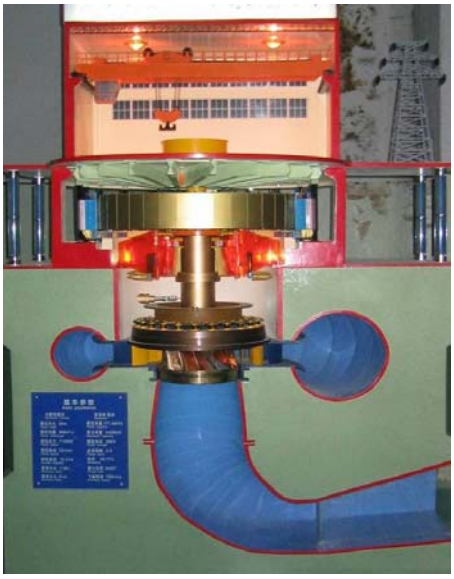

Figure 1 Cross-section of Three Gorge Plant model (Courtesy of Harbin Electric Works)

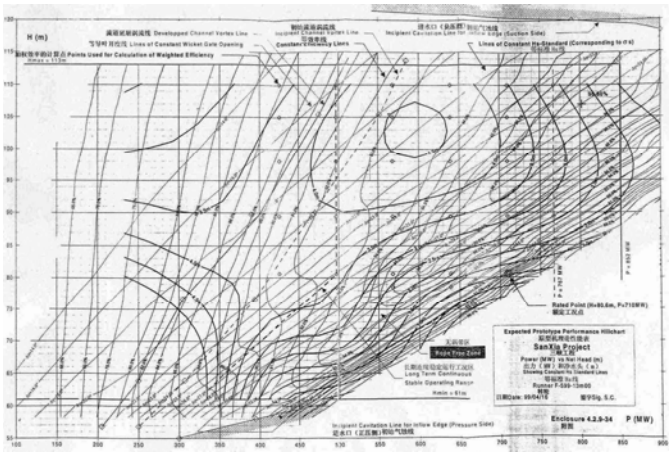

Figure 2 Expected prototype performance hill-chart for 11F by the supplier

The performance curve is shown by Figure 2. For most times, the 11F unit has been operating under low head conditions (around and below 70 m).

3. DAMAGE OBSERVED

3.1 NO4 GUIDE VANE (11F)

The damage observed on the Number 4 guide vane of 11F turbine is representative for this particular pattern of damage. The guide vane is a positively curved hydrofoil as shown in Figure 3. The turbine has total 24 guide vanes and 24 stay vanes, referring to Figure 4.

[2] They do not require an immediate rectification/repairing at this stage because the damage does not affect the safety and effectiveness of operation.

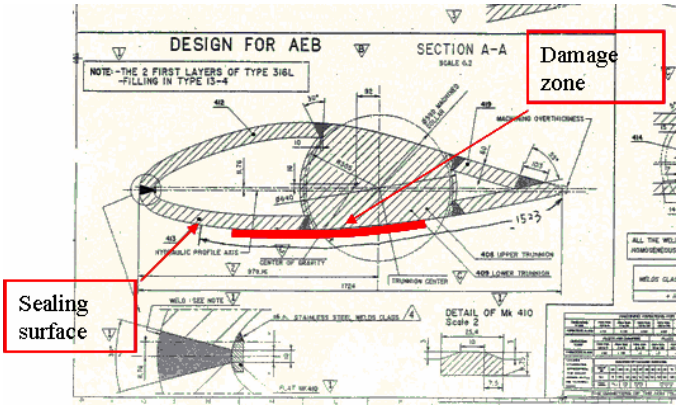

Figure 3 No 4 guide vane

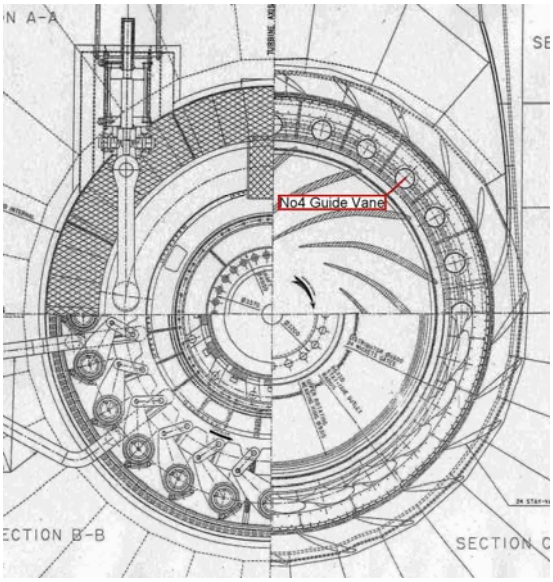

Figure 4 Plan view of 11F turbine

3.2 FEATURES

The damages occur only on the foil's lower surface[3] in the form of horizontal strips, starting from the favorable pressure gradient (FPG) zone extending into adverse pressure gradient (APG) zone as shown by Figure 5. The depth of most damaged area is much less than 1 mm fully covered by corroded rough surface as shown by Figure 8. Heated tail on damaged surface is observed (red-circled in Figure 8), which is another common feature. Figure 9 shows heated area at joints. However, it puzzles that the circled one (in Figure 9) is not similar to others that appear approximately at the main flow direction. This heated feature is also observed on other machines, e.g. photos from 9F are shown by Figure 7 and Figure 9. These damaged strips are approximately in the direction of flow there. Another feature is the wedged head which almost always presents[4]. Typical one is shown in Figure 10.

The damaged strips are distributed in span-wise, showing regularities, referring to Figure 5, with average span-wise spacing, $\lambda_{strip} \approx 0.100$ m .

4 ANALYSIS AND CONSIDERATIONS

Such damages on the guide vane have not been reported before. In order to facilitate a thorough investigation, based on the information gathered through the *in situ* inspection, a preliminary analysis and considerations are presented herewith.

Among all possible factors, cavitation damage needs to be considered firstly although the observed damage appearance does not comply with conventional cavitation damages often observed on Francis turbines. However, following factors based on the considerations of both metallurgical and fluid dynamic sciences strongly suggest the possible cause of cavitation.

4.1 METALLURGICAL CONSIDERATIONS

4.1.1 HEATED TAIL

[3] Here, the lower surface refers to the pressure side of a foil if the angle of attack is positive as conventionally defined in aerofoil aerodynamics.
[4] The heads of No 1 & 18 has been sanded off by the representative of the manufacturer during the *in situ* meeting 12-14 March 2006.

Figure 5 Damages on the lower surface on all guide vanes showing nearly the same pattern

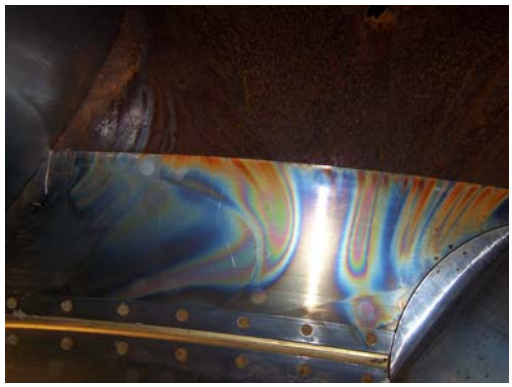

Figure 6 Heated sign on the top surface between guide vanes

Figure 7 Heated tail on the guide vane (9F)

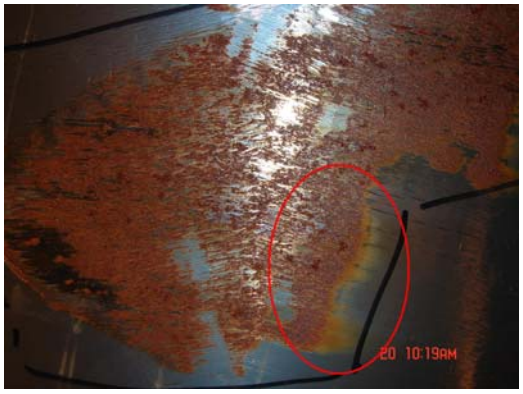

Figure 8 Damaged surface

Figure 9 Heated tails observed on the top ring (9F)

Figure 10 A representative damage-strip showing wedged head

The observed heated (blue and other) colour zone at the tails of the damaged areas suggests that this zone has encountered a temperature of $250^0C - 600^0C$ (termed as 'bluing' in heat-treatment[5]). As far as we know, the only hydrodynamic mechanism involved in Francis turbines that is able to provide/generate temperature at or above this range is cavitation. The experimentally proven temperature that a collapsing single bubble could generate is about $6000^0C - 7000^0C$ [6]. One may argue: 'why the damage compared with those often observed in Francis turbines, in particular those made of low-alloy steels before 1980's, are very different'. The following may provides the answer.

Figure 11 Typical sponge-like erosion pattern caused by a leading-edge cavitation attack (4000 hour operation) [18]

Typical cavitation damage is featured by sponge-like deep erosion, such as shown by Figure 11. Nowadays, materials with better cavitation resistance are used such as the martensitic stainless steel (containing 13% Cr and 4% Ni or 17% Cr and 7% Ni) replacing the low-Mn steel for fabricating machines. The material used for 11F is X3CrNiMo13-4 (EN-1088), which is close or equivalent to *CA6MN* (12.9% Cr, 4% Ni and 0.04% C), a commonly used martensitic stainless for turbine fabrications [20]. Whereas the striking force (i.e. cavitation attack) in this case is relatively weak owing to both the high overall pressure in the guide vane passage and the mechanism of cavitation[7]. The existence of this heated zone itself may also evidence a relative weak cavitation attack on a relatively high cavitation-resistance material. Why? We may put this argument in such a way: heating effect always presents during cavitation attack, but if damage rate is high, the heated portion of material is removed immediately/simultaneously by bubble strikes. Therefore, we can not see the heated zone afterwards. The heated part of material may remain to be seen if the cavitation erosion rate is low. The very low erosion rate (much less than 1 mm over 10,000 hours) of the damage in this case is consistence with the hypothesis proposed here.

4.1.2 CORROSION APPEARANCE

The existence of corrosion on all damaged area combined with the fact of very shallow damage depth (actually touch feeling only) readily tempts one to think that corrosion is the underlying cause responsible for the damage observed as some comments made at the meetings [21]. From the author's opinion, it might be more appropriate to assume the corrosion is a consequence of cavitation damage. The following arguments may provide clues for clearing the cloud over the nature of the corrosion appearance.

The material is a martensitic S S as suggested by its brand which is roughly equivalent[8] to *CA6MN* indicated by '*W*' in the Schaeffler diagram, referring to Figure 12.

It is well-known, for austenite S S, *sensitisation* is a phenomenon of heat effect that causes inter-granular corrosion and is a wide spread problem. The *stainless* character of stainless steels occurs when the concentration of chromium exceeds about 12 wt%. When an austenite S S is exposed to a temperature range between $620^0\ C$ to $676^0\ C$, subject to exposure-time as well as its own composition, the carbon will diffuse towards the

5 A simple heat-treatment method that coats steels with a thin, even film of coloured oxide from bluish-black to purple brown shade, obtained by exposure to an atmosphere of dry steam or air, at certain temperature subject to the material as well as the colour. A typical case of coating sheets with a thin, even film of bluish-black oxide is obtained by exposure to an atmosphere of dry steam or air, at a temperature of about 1000^0F (538^0C) done during box-annealing [29].

6 Comparison with black body's spectra gives the temperature values, subject to bubble size, content and external pressure fields. Collapse of multi-bubble cloud can generate even higher temperature owing to bubble-bubble interaction.

7 The mechanism will be addressed later.

8 Accurate and detail analysis of chemical composition and metallurgical structures needs to be done.

grain boundaries where the high concentration of carbon ties up the chromium by forming chromium carbides $M_{23}C_6$ at grain boundaries, which leaves a zone of chromium depletion (below 12%) in the immediate area around the grain boundary making this area less corrosion resistant than the bulk material and resulting in inter-granular corrosion. Such typical corrosion (on 304) is shown in Figure 13. The mechanism of sensitisation is conceptually shown by Figure 14.

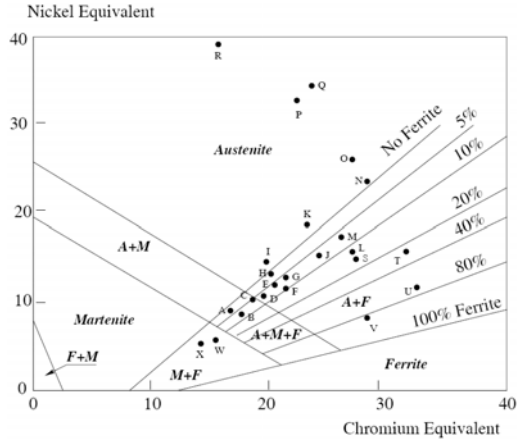

Figure 12 Schaeffler diagram [25]

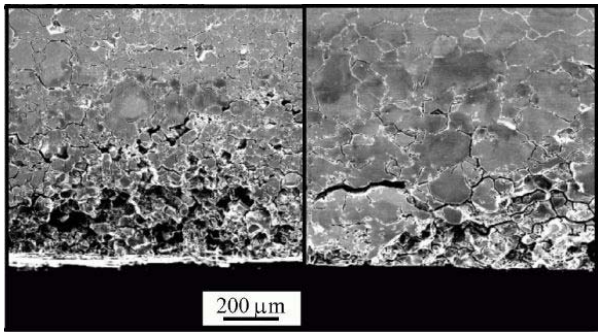

Figure 13 Grain decohesion due to intergranular corrosion [28]

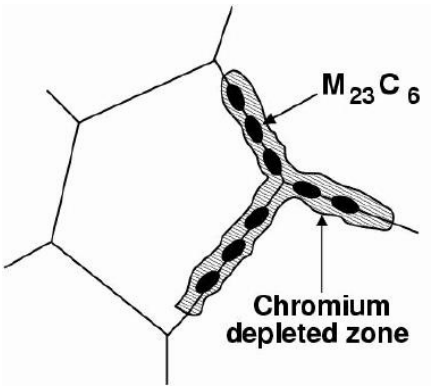

(a)

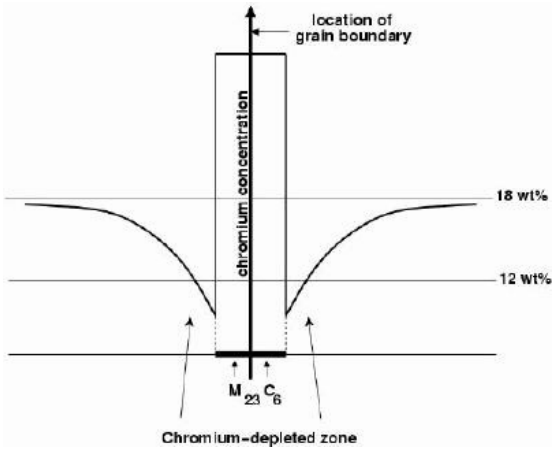

(b)

Figure 14 Conceptual sketch of sensitisation. (a) Chromium depleted zone susceptible to inter-granular corrosion (b) Chromium distribution across grain boundary [30].

Most publications concerning inter-granular corrosion refer to austenitic steels. Study of inter-granular corrosion in martensitic stainless steels is not in current technical literature. Does that mean sensitization is irrelevant or insignificant to martensitic stainless steels? Actually, inter-granular corrosion is also a potential problem to martensitic S S because it is a Fe-Cr-C system and always used in tempered condition[9], in which carbides are precipitated. Recent investigations [e.g. 2], show a trend that the maximum susceptibility to inter-granular corrosion was observed in the condition tempered at 500^0C to 550^0C, and a sensitized structure was detected. For lower tempering temperatures, it was less sensitized, or not at all, and for higher tempering

[9] Martensitic S S is often used for fabrication. Both strength and toughness are requested which is achieved through temper treatment. It is known: (1) at 350°C, higher strength and moderate toughness (2) at 650°C, moderate strength and high toughness (3) avoid 500°C, temper embrittlement (i.e. sensitisation) and minimum toughness.

temperatures, it was also less sensitized. A typical case (UNS S41000) is shown in Figure 15 (550^0C), and the characteristic value variations with temperature (for two hours) is shown in Figure 16. A zone of high sensitization-susceptibility is indicated clearly for temperature ranging from 500^0C to 600^0C.

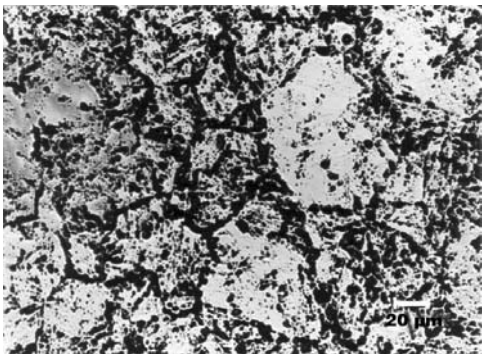

Figure 15 Optical micrographs of UNS S41000 steel specimens after oxalic acid etch test: tempered at 550^0C [2]

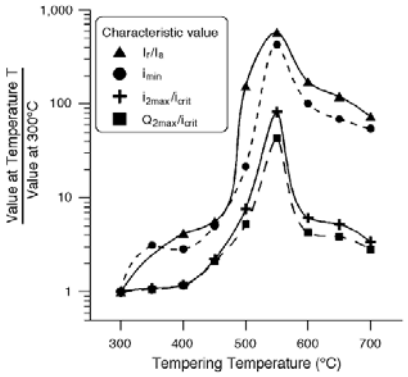

Figure 16 Comparison among electrochemical tests to discriminate degrees of sensitization for different tempering temperatures. Characteristic values are i_r / i_a for the DL-EPR, $i_{\min}$ for the potentiostatic test, and $i_{2\max} / i_{crit}$ and $Q_{2\max} / i_{crit}$ for the potentiokinetic polarization. To make different tests comparable, the ratio was plotted between the characteristic value for the material tempered at different temperatures and the same for the material tempered at 300^0C [2].

Based on the analysis above for the heated sign left on the tail of damaged area, the blue colour (plus other spectra of colors) strongly suggests a similar heat treatment at the temperature range of 500^0C to 600^0C that creates an ideal environment for sensitization, leading to inter-granular corrosion. This explains why corrosion appearance is discovered on the damaged area of this martensitic stainless steel after cavitation attack.

4.2 FLUID DYNAMICS CONSIDERATION

The damage pattern does not suggest a large structure of cavitating flow-structure that directly strikes and causes the damage such as those shown by Figure 11, whereas the wedged head of damage strips gives us a hint: are there any links with the turbulent spots generated during boundary layer transition to turbulence that is also featured by wedge head?

Through the inspection *in situ*, a conjecture has been put forward by the author that this is a non-typical turbine cavitation, its inception and corresponding damages are relating to boundary layer's streaks and most likely induced by turbulent spots during the boundary layer transition process [21 & 22]. In order to understand this, it is essential to see what conditions are required to enable the nuclei in the boundary-layer to cavitate and how the boundary-layer can provide such conditions through its transition process.

4.2.1 CAVITATION INCEPTION

Cavitation inception is closely related with and strongly influenced by boundary layer transition. The main points can be summarized as follows [19].

For cavitation in the boundary shear layer, the statistical properties of bubbles are dominated by the pressure fluctuation field in terms of their intensity and duration. Therefore, the distribution of the turbulence level, which varies across the boundary layer, alters the statistical characteristics of the micro-bubbles' inception performance across the boundary layer. This phenomenon was firstly demonstrated by Daily & Johnson [9]. This relation indicates that the lowest mean pressure across the boundary layer is the location where the turbulence level is highest since (referring to

Figure 17)

$$\overline{p} + \overline{\rho v'^2} = p_1(x) \qquad (1)$$

where $p_1(x)$: pressure in the free flow region beyond the boundary layer where $\overline{v'^2}$ is negligible

$\overline{p}$: mean pressure

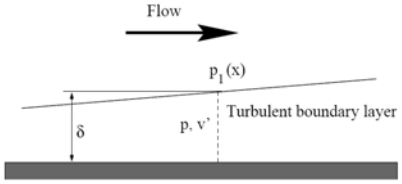

Figure 17 Conceptual sketch of (turbulent) boundary layer

It is obvious that bubbles at this particular location have the highest probability to cavitate owing to the minimum value of mean pressure and the maximum value of instant pressure drop.

The influences of magnitude and time scale of turbulence on cavitation inception were also demonstrated by many other studies on inception scale effect. For example as early as 1981, Arakari & Acosta [4] already emphasize the importance of time scale by postulating that the turbulent fluctuations may actually stall the local flow near the wall, leading to a brief period of separation or a turbulent burst with reverse flow. Then the nuclei within these regions may be exposed to a low pressure longer than would otherwise be the case, thereby promoting the growth of micro-bubbles. This is supported by their experiment that the frequency of the most unstable Tollmien-Schlichting wave in the laminar boundary layer just prior to transition is about 5 kHz equal to a reference time period of 0.2 msec for growth, which is about the same order as the bubble life-time (0.1 msec) observed in their experiments. The early work by Huang [12] also found that the inception is correlated with the spatial amplification ratio A through the mechanism of laminar to turbulent transition or laminar separation. For the tunnel with low level of free-stream turbulence, the inception is well correlated with the computed amplification ratio value of $A = e^{11}$; and, for higher levels of free-stream turbulence, it takes place in a region where the value of A is less than e^{11}, for say e^9 or even e^7.

As early as 1979, attempt by using the Kolmogorov theory for homogeneous and isotropic turbulence to relate the properties of the temporal pressure field to cavitation inception for both free turbulent shear flow and fully developed boundary layer flow has been made. For fully developed boundary layer flow, Arndt & George [5] suggested that if

$$\left(\frac{u_*^2}{\nu}\right) T_B < 1 \quad \text{for smooth wall;}$$
$$\left(\frac{u_*^2}{h}\right) T_B < 1 \quad \text{for rough wall,} \qquad (2)$$

the nuclei in the flow will have enough time to respond to the entire spectrum. Otherwise only a fraction below the frequency of T_B is sensed by the micro-bubbles[10].

Therefore, for the nuclei to cavitate, long enough negative pressure drop generated by flow structures is essential.

4.2.2 FREE STREAM TURBULENCE & B L TRANSITION

Despite of studies over decades, the origins of turbulent flow and transition from laminar to turbulent flow still remains an unsolved challenge for fluid mechanics. Currently, even for flows over a flat plate, no mathematical model can precisely predict the transition Reynolds number because of variety of influences, such as free-stream turbulence, surface roughness, which are still not fully understood yet. Currently, owing to the availability of linear stability methods and the knowledge of breakdown mechanism being initial condition dependent, studies are aiming at understanding the source of initial disturbances rather than the details of the

10 For turbulent boundary layer flow, the highest frequency in the flow is (u_*^2/ν) for smooth wall and (u_*^2/h) for rough wall. Thus if the bubble frequency T_B is higher than the highest frequency, the entire spectrum may contribute to bubble growth.

later stages of transition [27]. Very recently, the discovery of Soliton-like Coherent Structure (SCS) by Lee [15 and 16] gives clearer picture of the low-speed streak formation and its breakdown, which helps to clarify the complex burst phenomena. As pointed out by Lee and Chen [17][11]: there are two different kinds of flow structures which have been referred to as stream-wise vortices by other researchers. One is the real stream-wise vortex. The other is the long streak containing several SCS, often referred as solitary quasi-stream-wise vortex. A long streak containing several SCS appears in the very near-wall region. The middle layer has two real stream-wise vortices which are the relatively long quasi-stream-wise vortices (often counter-rotating pairs). The interaction between the secondary closed vortex and the Λ-vortex produces the chain of ring vortices (i.e. high frequency vortices), leading to breakdown & turbulent spots. Figure 18 shows the evolutions from SCS to a long streak and its breakdown.

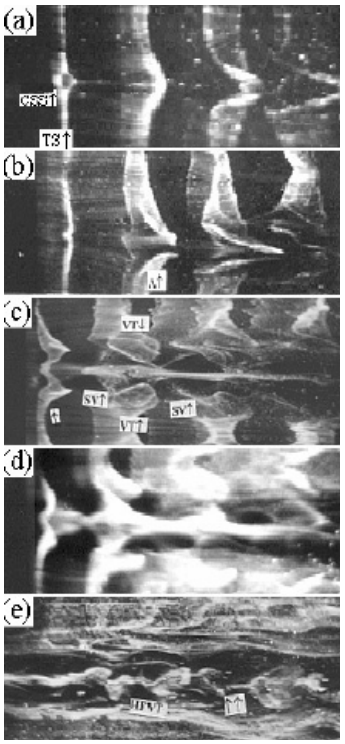

Figure 18 (a) T–S wave and CSS. The hydrogen bubble wire was at x = 250mm and y = 0.75mm; (b) The Λ-vortex structure. The wire was positioned at x = 300mm and y = 0.75mm; (c) Development of the Λ-vortex and the long streak. The wire was at x = 350mm and y = 0.75mm; (d) The long streak is composed of several CS-solitons and the wire was at x = 450mm and y = 0.5mm; (e) Breakdown of a long streak. The wire was at x = 550mm and y = 0.75 mm [17].

However, for turbines, owing to its complexities in geometry and off-design operation, much less is known [26]. For hydro turbines, the interplay of B L transition with cavitation inception is important but little study has been done. Despite of these difficulties, it is still possible to understand the phenomenon based on the knowledge gained from flat plate cases.

For 3D B L flows over (hydro) foil, cross-flow instability may dominate the breakdown while T-S waves act as generators of fundamental low-frequency secondary modes, but are neither important for their growth nor for breakdown [32]. For the problem on our hands, the damage pattern on guide vane gives us a clue that it is virtually a 2D flow. The resulting perturbed flows are span-wise-dependent but essentially unidirectional, i. e. the transverse velocity components are much smaller than the stream-wise component. The instability of such transversely sheared flows appears to be related to various aspects of the transition process, such as secondary instabilities and by-pass transition. Many factors [35] can cause three-dimensional steady/unsteady distortions in the form of stream-wise or longitudinal vortices. These include small steady or unsteady perturbations superimposed on the oncoming flow, imperfections at the leading edge[12], cross-flow instability, and Görtler vortices induced by surface curvature, as well as certain excitation devices[13]. Distortion of this kind also arises due to the nonlinear interaction between pairs of Tollmien-Schlichting waves.

Free-stream turbulence initiates three distinct motions within the boundary layer, as summarised by Saric et al [27]. The first motion is a sustained, streaky ($z \approx 2\delta$), high amplitude ($|u'| \approx 5-10\%U_\infty$) motion, which is probably due to stretching of the ingested free-stream vorticity and the growth of transient modes, i.e. the Klebanoff mode. The second is an outer-layer oscillation at T-S frequencies that grows weakly in the stream direction. The third is the usual T-S mode, which exhibits higher growth rates.

Currently we have very limited understanding about the instability of Klabenoff mode and its role in the transition owing to the random nature of both the free-stream disturbances and the Klebanoff motion. Most studies so far investigate steady distortions, induced in a controlled manner through the receptivity at leading

[11] For more details, please see the forthcoming publication by Lee & Chen [17].
[12] And the sealing surface in our case.
[13] The guide plate may serve well as an excitation device. This will be discussed later.

edge only[14]. The maximum growth of this K-mode distortion is a function of Reynolds number and wave number, e.g. as demonstrated by Anderson et al [3]. In Figure 19(I), $\overline{\beta}$ is span-wise wave number,

$$\overline{\beta} = \beta^* \nu / U_\infty = \beta / \sqrt{\mathrm{Re}} \qquad (3)$$

with β^* is the dimensional span-wise wave number; β is the non-dimensional span-wise wave number valued as $\beta = 0.45$ for maximum transient growth.

The mechanism of the downstream response to upstream disturbance is visualized by Figure 19(II). The calculated initial disturbance at $x_0 = 0$ is outside the boundary layer, while its downstream response is inside the boundary layer. Thus, this numerical simulation demonstrate well the receptivity at the leading edge: *the disturbances at the leading edge that cause the largest growth of stream-wise streaks inside the boundary layer are vortices aligned in the stream-wise direction outside the boundary layer*.

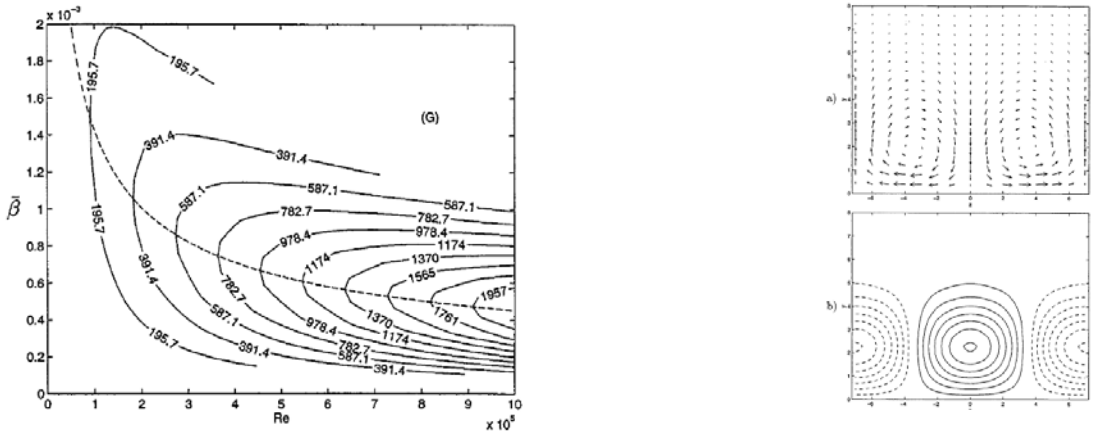

(I) (II)

Figure 19 (I) Contour plot of maximum transient growth vs. $\overline{\beta}$ and Reynolds number. The dashed line describes $\overline{\beta}$ for which the maximum transient growth occurs given a specific Reynolds number. Here $x_0 = 0$ [3]. (II) (a) Velocity vectors in the z – y plane of the optimal disturbance at $x = x_0$. Here $x_0 = 0$ and $\beta = 0.45$. The *u* component is zero. (b) Contours of constant stream-wise velocity representing the downstream response at $x = x_f = 1$ corresponding to the optimal disturbance shown in (I). The *v* and *w* components are zero. Here, the solid lines represent positive values and the dashed lines represent negative values [3].

As early as 1979, Gates & Acosta [11] have already shown that free-stream turbulence is an important factor for inception scaling; and that the mechanism through which this factor influences inception is the structural alteration of the boundary layer in terms of its separation and/or transition[15]. This is crucial for extremely large turbines, the difference of Reynolds number (based on main flow parameter, reflecting the status of free stream) between model and prototype is in the order of 10^2, which represents a significant difference on turbulence level[16], consequently its influence on cavitation inception.

The K-mode involvement (responding to the free-stream turbulence) should be further considered owing to following reasons.

Firstly, the guide plate increased free-stream turbulence is a primary concern in the sense of receptivity and the transient growth of K-mode instability, which may bypass the primary OSE[17] mode and lead to early and random breakdown/turbulent spot although the flow in the first half of guide-vane passage is a highly

14 In reality, there is a continuous receptivity process along the stream-wise extent of the boundary layer, as in flow around the guide-vane.

15 See, e.g. § 2.4 'Cavitation Nucleation and Inception' in *Cavitation of Hydraulic Machinery*, ICP, London.

16 This will be discussed later.

17 Orr-Summerfeld Equation

accelerating flow[18], i.e. with strong favourable pressure gradient, which would have a prolong laminar B L until transition if the level of free-stream turbulence was low.

Secondly, the turbulences in the wake of stay vane is likely to possess span-wise structure (say span-wise distributed stream-wise vortices) comparable with the span-wise variation of observed damage strips, and thus the high receptivity occurs only associated with these structures, causing K-mode transient, bypass transition and breakdown to turbulence in such a pattern of strips.

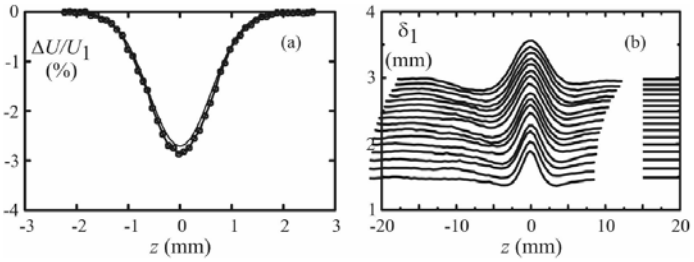

Figure 20 (a) Wake profile 63.5 mm upstream of leading edge. Z-relative to wire centreline. (b) Stream-wise growth of span-wise variation of displacement thickness, δ_1. Z-relative to the peak δ_1 values. Lines in range 15 < z < 20 are Blasius values, i.e. $\delta_1 = 1.7208(\nu x / U_1)^{1/2}$ [33].

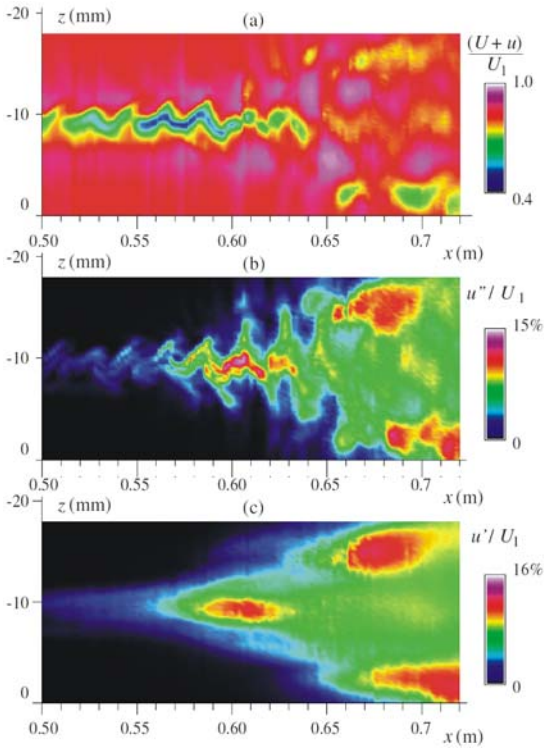

Figure 21 True spatial contours in plane, y=2mm (a) $(\overline{U} + u_\phi)/U_1$. (b) u''_ϕ / U_1. (c) Broadband unsteadiness, $\overline{u'}/U_1$ [33].

	Zero pressure gradient	Mild pressure gradient	Strong pressure gradient
SSLC	10.3^0	9.4^0	7.8^0
TSLC	5.5^0	4.1^0	2.5^0

Table 1 half angles of wedge spreading for zero, mild and strong favourable pressure gradients for SSLC and TSLC [8]

Figure 22 SSLC results for the turbulent wedge under zero, mild and strong (favourite) pressure gradients respectively [8] .

Thirdly, the wedged head of damage strips highly resembles the turbulent spots caused by such a streak (K-mode) transient growth and breakdown in a Blasius B L, which leads to a turbulent wedge. As an example, the work by Watmuff [33] is worth mentioning here, which demonstrates the evolution of a turbulent wedge from stream-wise streak. In his study, a narrow low-speed streak (i.e. region of elevated thickness) is deliberately

[18] Rough estimation shows that the average velocity increases from 12 m/s at the entrance to 25 m/s at the mid-chord, with a acceleration of $\left.\frac{dV}{dS}\right|_{average} \approx 18\ \mathrm{sec}^{-1}$.

introduced into the Blasius boundary layer as a result of the interaction of a laminar wake with the leading edge of the flat plate. The wake is generated by stretching a fine wire across the full extent of the test section and it is aligned perpendicular to the free-stream and to the leading edge. The wire has a diameter of d=50.8 mm, located 184 mm upstream of the leading edge. Stream-wise development of the span-wise variation of displacement thickness resulting from interaction of the wake (referring to Figure 20 (a)) with the leading edge is shown in Figure 20 (b) for 16 stream-wise positions, ranging from x=0.3 to 1.8 m. The results clearly demonstrate the narrow region of elevated thickness, i.e. the low-speed streak. The final stages of growth and the ultimate breakdown of the streak are shown in Figure 21(a-c). The breakdown on the centre-line and the formation of two regions of highly unsteady flow on either side of the streak are most clearly evident in the contours of the broadband unsteadiness shown in Figure 21(c). It is evident that streak is responsible for introducing a new pair of streaks on either side via some instability mechanism, causing span-wise growth of the wedge since a span-wise succession of new streaks is observed in the early stages of its development.

Here, $\overline{U}+u_{\phi}$ is the total phase averaged stream-wise velocity; u' is the background (broad band) unsteadiness; and, u'' is the phase averaged unsteadiness.

The wedge-shaped turbulent spot can also be visualized by using both shear sensitive liquid crystal (SSLC) and temperature sensitive liquid crystals (TSLC). The results [8] show the dependency of wedge spreading angle on the level of flow acceleration, referring to Table 1 and Figure 21.

Lastly, as demonstrated by Matsubara *et al.* (2000) [23] experimentally that the growth of near-wall streaks is a key phenomenon triggering the bypass transition leading to breakdown & turbulent spots. The mechanism of breakdown postulated by Lee [15 & 16] suggests that the generation of the high frequency vortices, i.e. the chain of ring vortices is resulting from the interaction of the secondly closed vortex with the Λ-vortex. For our case, these vortices surely will create an favorite environment for nuclei to grow.

5. DISCUSSION

All these considerations above make us to think: if for this case (particular large turbines) the scale effect makes it happen[19] that the *turbulent spots* just generated at a right area where flow has a highest susceptivity to cavitation inception[20] and thus trigger the *cavitation-inception* there, In other words, both *turbulent spots* and *inception points* concise for prototype.

5.1 MODEL-PROTOTYPE SIMILARITY

5.1.1 FREE STREAM TURBULENCE

The free-stream turbulence level of prototype is much higher than that of model turbine, which makes the prototype, in particular for large turbines, more susceptible to the formation of low-speed streak and the transitional breakdown through the receptivity mechanism. For the Three Gorge turbines, if the similarity of free stream turbulence were required, by assuming a prototype-model scale of 28, the Reynolds number equality would have required

$$\frac{H_m}{H_p} = \left(\frac{D_{1,p}}{D_{1,m}} \right)^2 ,$$

that is,

$$\frac{H_m}{H_p} \approx 784, \text{ i.e. } H_m \approx 47,824 \sim 88,592\ m$$

[19] On model tests, no cavitation observed within the allowable operating zone.

[20] At low head operating condition, the inlet circulation reduces which in turn makes the lower surface of guide vane become more susceptible for cavitation that the upper surface.

In reality, this is impossible, and consequently the constraint of test rig makes us to use much smaller Reynolds number for models. For the Three Gorge turbines, the prototype's Reynolds number is approximately $\mathrm{Re}_{,p} \approx 4.6\times10^{7}$ at $Q_{opt} = 718\ m^3/s$, while for models, it might be $10^2 \sim 10^3$ smaller[21]. This implies that the free-stream turbulence level is much higher for prototype.

For the turbines in the left-plant, the flow in the guide-vane passages indeed is subject to a high level of free-stream turbulence owing to the reason below. For this turbine design, a guide plate is provided in the spiral case prior the entrance of stay-vane passage shown in Figure 23. Obviously, the designer intended to reduce the size of spiral case without sacrifice of cross-section area. However, the premature damage (a piece torn off) of the guide plate and subsequent severe pressure-fluctuation and machine-vibration gave us a clear clue: this device might have caused unusual free-stream disturbances in the oncoming flow (i.e. the wake flow of stay-vane) to the guide vane. Will these disturbances cause particular distortion in the boundary layer of guide vane? Researchers have demonstrated a type of span-wise distortion (modulation) induced by various free-stream disturbances. For example, it has been shown that small low-frequency three-dimensional perturbations in the free stream can produce significant distortion within the boundary layer, leading to alternating span-wise thickening and thinning [10]. Steady disturbances (e.g. artificial roughness, vortices etc) can also cause a similar type of span-wise modulation [e.g. 6]. And these distortions are all in the form of elongated streaks now named as *Klebanoff* mode [13, 34 and 14].

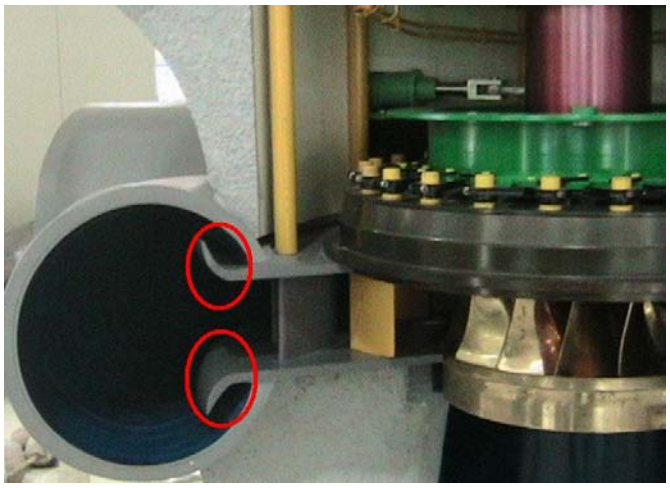

Figure 23 Guide-plate (circled) shown on the model of turbine

5.1.2 BOUNDARY-LAYER SIMILARITY

Boundary-layer similarity not only requires the similar free-stream conditions but also the equality of the boundary-layer based Reynolds number,

$$\mathrm{Re}_l = \frac{L\cdot U_\infty}{\nu}$$

Owing to the equality of Strouhal number (i.e. n_1'), this leads to

$$\frac{(\mathrm{Re}_l)_m}{(\mathrm{Re}_l)_p} = \left(\frac{D_{1,\,m}}{D_{1,\,p}}\right)\left(\frac{H_m}{H_p}\right)^{1/2} = 1$$

That is, for our case (i.e. the prototype-model ratio of 28) the boundary-layer similarity also requires

$$H_m = 784\,H_p$$

In reality, as mentioned before, it is impossible to use such high head for model tests. And this constraint condition makes the ratio of two boundary-layer based Reynolds numbers far away from unity, resulting in the range of

$$\frac{(\mathrm{Re}_l)_m}{(\mathrm{Re}_l)_p} = \frac{1}{28}\left(\frac{H_m}{H_p}\right)^{\frac{1}{2}}$$

Therefore, it is absolutely no boundary-layer similarity for model and prototype in respect of their boundary-layer dynamics, making the prototype much more susceptible to turbulent transition.

[21] The Reynolds number for prototype is obtained from Prof Wu Yu-Lin of Tsinghua University and for models it is estimated based on the current conditions of turbine test rigs around the world.

These two factors above explain well the fact that no cavitation observed during model tests does not guarantee the Three Gorge turbines free from cavitation attack.

5.2 ESTIMATION OF LAMINAR STREAKS AND TURBULENT SPOTS

The span-wise wave-length (spacing) of laminar streaks or Klebanoff wave, λ^*, can be estimated[22] as

$$\lambda^* = 10\,\delta^*$$

Here, δ^* is the displacement thickness,

$$\delta^* = \frac{1.7208\,L}{\sqrt{\mathrm{Re}_{,l}}}$$

From a typical damage strip observed, say $L = 0.550$ m, we have $\mathrm{Re}_{,l} = 5.2\times10^6$ (based on $U_\infty \approx 12.4$ m/s), and $\delta^* = 0.43\times10^{-3}$ m. This gives a span-wise wave length

$$\lambda^* \approx 4.3\times10^{-3}\ \mathrm{m}$$

The transition region is characterised by a random appearance of turbulent spots, referring to Figure 24. Assuming a spot generated from 20-30 such streaks, the turbulent spot spacing λ^*_{spot} will be

$$\lambda^*_{spot} \approx 86\times10^{-3} \sim 129\times10^{-3}\ \mathrm{m}$$

It is approximately equivalent to the observed strip spacing $\lambda^*_{strip}\,(\approx 0.100\ \mathrm{m})$. This again strongly supports the conjecture that the damaged strips are caused by cavitation spots that incepts from turbulent spots.

Surprisingly, the features of turbulent-spot above are all supportive to the hypothesis that the cavitation inception points might coincide with the turbulent spots, or in other words, cavitation incepts from these turbulent points. Thus, a *dynamics process* follows: once the first cavitation damage spot is created at the turbulent spot, it will serves well as a roughness spot create a subsequent damage immediately downstream. This dynamic process progresses stream-wise, resulting in such a horizontal damage strip with a wedged head and heated tail. These span-wise distributed stream-wise damage strips thus become dominant pattern on the guide vane. This may provide a reasonable route for searching more detailed explanation and answer to the problem at hand.

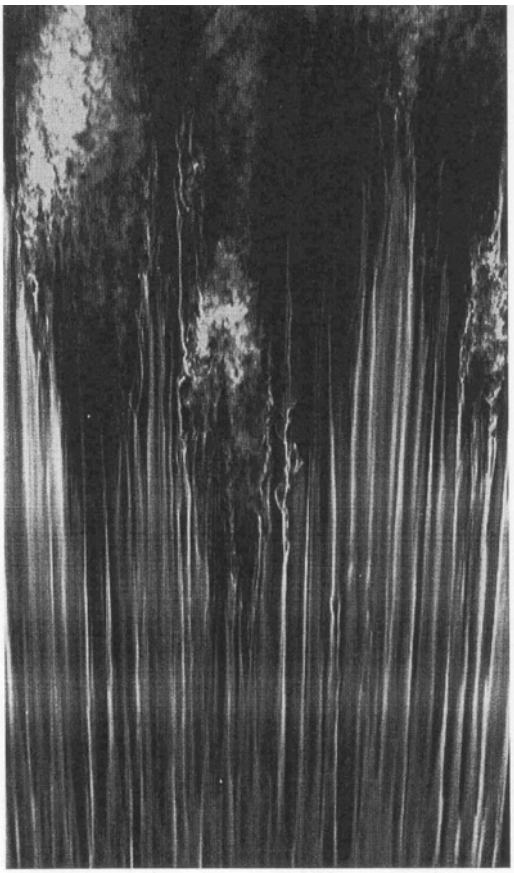

Figure 24 Streak structure observed through smoke visualisation in a laminar boundary layer subject to 2.2 % free-stream turbulence [1]

6. REMARKS

As this problem has just been discovered, apart from *in situ* inspection, no further studies have been conducted yet. Therefore, it is only a very preliminary report servicing as guidelines for further investigation

[22] The results obtained from flat plate case, i.e. for pressure gradient $K = 0$, are used, where K is defined as $K = \frac{\nu}{U_\infty^2}\frac{dU_\infty}{dx}$. For the turbine guide vane, the average value at inlet (FPG) is about $K = 0.148\times10^{-6}$.

and research proposal preparation. However, it does provide strong evidence about the cause of this type of damage that has never reported before.

A detailed research across multi-disciplinary subjects should be carried out. The followings are the main suggestions.

1. Flow analysis of the oncoming flow influenced by the guide plate in terms of flow structure(s) and turbulence level variation is essential. The study should employ the fluid-structure interaction approach. The shape of the guide plate (thin and plateful geometry without stiffener owing to flow requirements) readily induces various vibrating modes including extremely low-frequency ones. These low-frequency modes are particular concern because their influences on the growth of boundary layer streaks as mentioned before. The studies may performed numerically first and then followed by experiment study on prototype and model turbines.
2. The information obtained from above flow analysis should facilitate the boundary layer studies[23]. It will look for possible streak formation, receptivity and transition mechanism (including the interaction with T-S waves). It is particular interesting to see if the stream-wise position and the span-wise variation of the breakdown (in particular, the turbulent spots) under such strong influences of the free-stream (flow-structures and turbulence level) agree with the observed pattern of strips. The study may be carried out firstly on flat-plate with added pressure gradients similar to those on the guide vane either numerically or experimentally[24]. As the most interesting issue we want to know is the spatial growth of streaks, a DNS approach in space domain is strongly suggested for numerical study. With the information obtained from flat-plate, we may able to predict the trends about the streak formation, growth, interaction with T-S waves and breakdown on hydrofoil. And, observation on prototype can be designed and carried more effectively and predictably.
3. The possibility that cavitation inception might occur right at the turbulent spots should be verified through experiments by testing on model foil and monitoring on the guide vane of prototype. Various approaches can be employed. For example, for prototype, SSLC mentioned before combined with high-speed photography through endoscope is a good choice.
4. The material undergoing this type of cavitation attack should be mimicked through laboratory study in order to understand the heating phenomenon/mechanism associated with this type of damage. It may uncover knowledge not known yet to us. Laboratory study using facilities such as cavitation tunnel or rotating device should be supported by metallurgical and chemical analyses.
5. Developments of novel turbine design/manufacture ideas are encouraged in order to respond to the challenges to extremely large turbines. For example, novel spiral case that has smaller size[25] and better flow conditions should be sought to replace the use of guide plate, which obviously disturbances flow significantly, resulting in high turbulence level in free-stream and consequent problems[26].
6. The B L behavior, such as transition length and scaling laws etc, should be investigated thoroughly. This is particularly important for huge turbines. The size of their components[27] and the high free-stream velocity[28] make the critical Reynolds number[29],

---

[23] The sealing surface on the guide vane serves as a profile discontinuity which could be another source from generating boundary layer flow distortion. This needs to be considered in the analysis too. This is particularly true for this case because the sealing surface was machined on a bended stainless steel plate, very likely leaving the edge highly wavy pattern (not as expected straight lined edge).

[24] On scaled down model.

[25] As mentioned before, for high and medium specific speed turbine-generator units, spiral case is often the crucial component that determines the overall size of plant. Therefore, reduction of spiral case has a significant impact to the hydro scheme's economic feasibility. This is why manufacturers often take high risks to reduce the size of spiral case in order to win the bidding. No doubt, the idea of using guide plate, which has already caused a break down event, has to be justified technically and economically. In the March of 2006, the author has made a suggestion to the M & E department of CTGPC about the feasibilities of employing oval cross-section spiral case for the size reduction.

[26] The 3-D damage on the fillet of stay-vane immediately down stream of the guide-plate might be well explained by the disturbances introduced by the guide plate.

[27] Such as the chord lengths of both the stay vane and the guide vane, which are well over one metre.

[28] In the order of 20-30 m/sec.

[29] $3\times10^5 \sim 3\times10^6$ for flat plate at zero angle of attack, subject to free-stream turbulence level.

$$\mathrm{Re}_{crit} = \frac{Ux_{crit}}{\nu},$$

to be reached in the FPG zone instead of APG zone, resulting in more susceptibility to cavitation inception compared with smaller turbines. Therefore, for large turbines, while scaling cavitation data from model to prototype, the scaling effect due to the boundary-layer property difference must be investigated thoroughly and considered properly. Currently our knowledge about the transition length in turbines is fairly poor compared with that of flat plate B L case. For gas turbines, a correlation[30] is found through experiments. That is, the Reynolds number Re_{l_T} calculated with the transition length l_T^* is a linear function of $\mathrm{Re}_{\theta T}^{5/4}$, where $\mathrm{Re}_{\theta T}$ designates the momentum thickness Reynolds number at the end of transition [e.g. 26]. But for hydraulic turbines, little work has been done yet neither theoretically nor experimentally.

7. The damage occurred on the turbines presents no urgent need for remedy action, and turbines can be put back into operation as usual. With the increase of reservoir water-level in the coming autumn, the operating head will gradually move into the optimum head zone and it is anticipated that the damage will also reduce or even disappear[31]. However, a continuous and comprehensive monitoring, recording and accumulating detail data about the machine operation is essential to the understanding of the phenomenon and the control of machine status.
8. The study on these fundamental issues will serve as a sound base for developing next generation of huge turbines (e.g. 1000 MW unit). An effort by multi-disciplinary team at international level is essential.

ACKNOWLEDGMENTS

The author would like to express his sincere thanks to the EPSRC's Warwick-IMRC for their long term financial support (R.ESCM.9001 and R.ESCM9004) on turbine technology and cavitation; and to the CTGPC for their financial & technical support during his visit to the Three Gorge Station from 19th to 20th of March 2006. Thanks also go to Prof Dai Jiang, the Deputy Director of Mech. & Elec. Division of CTGPC and Professor K Sen, the Indian Institute of Technology, New Delhi, for valuable discussions.

REFERENCES

1. Alfredsson P H and Matsubara M, 2000, 'Free-stream Turbulence, Streaky Structures and Transition in Boundary Layer Flows', Fluids 2000 Conference and Exhibit, Denver, CO, USA, 19-22 June 2000.
2. Alonso-Falleiros N, Magri M and Falleiros I G S, 1999, 'Intergranular Corrosion in a Martensitic Stainless Steel Detected by Electrochemical Tests', Corrosion, Vol55, No8.
3. Andersson P, Berggren M and Henningson D, 1999, 'Optimal disturbances and bypass transition in boundary layers', *Physics of Fluids*, 11(1), January 1999
4. Arakeri V H and Acosta A, 1981, 'Viscous Effects in the Inception of Cavitation', ASME J. Fluid Eng. 103, pp280-287.
5. Arndt R E A and George W K, 1979,'Pressure Fields and Cavitation in Turbulent Shear Flows', 12th Symp. Naval Hydrodynamics, Washington D. C., pp327-339.
6. Bradshaw P, 1965, 'The effect of wind-tunnel screens on nominally two-dimensional boundary layers', *J. Fluid Mech*. 22, 679-687.
7. Brandt L, Schlatter P and Henningson D., 2004, 'Transition in boundary layers subject to free-stream turbulence', *J. Fluid Mech.* (2004), vol. 517, pp. 167–198
8. Chong T, Zhong S and Hodson H, 2005, 'Visulization of Turbulent Wedges under Favourable Pressure Gradients using Shear Sensitive and Temperature-sensitive Liquid Crystals'.
9. Daily J W and Johnson V E, 1956, 'Turbulence and Boundary-Layer Effects on Cavitation Inception From Gas Nuclei', Transactions ASME , 78, pp1695-1706.
10. Dryden H L, 1936, 'Air flow in the boundary layer near a plate', *NACA Report* 562.
11. Gates E M and Acosta A, 1979, 'Some Effects of Several Freestream Factors on Cavitation Inception of Axisymmetric Bodies', 12th Symp. Naval Hydrodynamics, Washinfton D. C. pp86-112.
12. Huang T T, 1981, 'Cavitation Inception Observations on Six Axisymmetric Headforms', ASME J. Fluid Eng. 103, pp273-279.
13. Kendall, J. M. 1985 Experimental study of disturbances produced in pre-transitional laminar boundary layer by weak free stream turbulence. AIAA Paper 85-1695.

[30] Precisely the same correlation stems from processing experimental data for both smooth and rough surfaces.

[31] The increase of head will increase the inlet circulation, shifting the angle of attack from negative back to optimum value and increasing the pressure on the lower surface of guide vanes.

14. Klebanoff, P. S. 1971 'Effect of free-stream turbulence on a laminar boundary layer', *Bulletin. Am. Phys. Soc*. 16.
15. Lee C. B., 'New feathers of CS-solitons and the formation of vortices', *Phys. Lett*. A 247 (1998) 397–402.
16 Lee C. B., 'Possible universal transitional scenario in a flat plate boundary layer: measurement and visualization', *Phys. Rev*. E 62 (2000) 3659–3670.
17. Lee C B and Chen S Y, 2006, §2 'Dynamics of Transitional Boundary Layer' in *Transition and Turbulent Control* (Editor Lai Fun), SPI-B320 (in press).
18. Li S C, 2000 §6.2 'Cavitation Damage in Turbines', in *Cavitation of Hydraulic Machinery*, ICP, London
19. Li S C, 2000 §3.7.4 'Bubble-Flow Field Interaction' in *Cavitation of Hydraulic Machinery*, ICP, London.
20. Li S C, 2000 §6.5 'High Resistance Materials' in *Cavitation of Hydraulic Machinery*, ICP, London.
21. Li S C, 2006 'Cavitation Damage: Three Gorge Turbines (Phenomenon, Implication & Unknowns…)', presentations at the Three gorge Power station (19 March 2006), the Beijing University (28 March 2006) and the National Research Institute of Hydro Power (29 March 2006)
22. Li S C, 2006, 'Guide Vane Surface Damage to Three Gorge Turbines', WIMRC FORUM06, 3rd July 2006, Warwick University, Coventry, UK
23. Matsubara *et al*.,2000, in Proc IUTAM Symposium on Laminar-Turbulent Transition (H Fasel & W Saric, eds), Springer.
24. Morkovin MV, Reshotko E, Herbert T, 1994, 'Transition in open flow systems—a reassessment', Bull. Am. Phys. Soc. 39:1882
25. Rao A S and Kung D, 1987, Metallic Overlay Materials for the Optimum Cavitation Performance of Hydraulic Turbines, Report for the Canadian Electric Association, CEA No.135 G273.
26. Ryzhov O S, 2005, 'Transition length in turbine & compressor blade flows', Proc. R. Soc. A, doi: 10.1098 / rspa. 2005. 1651.
27. Saric W S, Reed H L, and Kerschen E J, 2002, 'Boundary-layer Receptivity to Free-stream Disturbances', Annu. Rev. Fluid Mech. 2002. 34:291–319.
28. Shimada M, Kokawa H, Wang Z J, Sato Y S and Karibe I, 2002, 'Optimization of grain boundary character distribution for intergranular corrosion resistant 304 stainless steel by twin-induced grain boundary enngineering', Acta Materialia, 50, pp2331-2341.
29. Simons Roll Forming Co, 2006, 'Glossary of Metal Terms', www.rollformedshapes.com/metalterms.htm.
30. Sourmail T and Bhadeshia H K D H, 'Stainless steel', www.msm.cam.ac.uk/phase-trans/2005/Stainless_steels
31. Three Gorge Power Station, 2006, 'Damage of Guide Vane Surface (Left Powerhouse)', Document for the *in situ* Investigation Meeting, 12-14 March 2006, Yi Chang, China.
32. Wassermann P and Kloker M, 2005, 'Transition mechanisms in a three-dimensional boundary-layer flow with pressure-gradient changeover', J. Fluid Mech. (2005), vol. 530, pp. 265–293.
33. Watmuff J H, 2004, 'Evolution of a Turbulent Wedge from a Streamwise Streak', 15th Australasian Fluid Mechanics Conference, The University of Sydney, Sydney, Australia, 13-17 December 2004.
34. Westin, K. J., Boiko, A.V., Klingmann, B. G. B, Kozlov, V. V. & Alfredsson, P. H. 1994 Experiments in a boundary layer subjected to free stream turbulence. Part I. Boundary layer structure and receptivity. *J. Fluid Mech*. 281, 193-218.
35. Wu X and Luo J, 2001, 'Instability of Blasius boundary layer in the presence of steady streaks', *Annual Research Briefs* 2001, Centre for Turbulence Research.